SANDIA REPORT
SAND2018-10479
Unlimited Release
Printed September 2018

High Fidelity Hybrid Method for In Situ Borehole Stress Determination Final Report

Mathew D. Ingraham, R. Charles Choens, Thomas A. Dewers, Stephen R. Sobolik, Jennifer Wilson, Courtney G. Herrick, Moo Y. Lee

Prepared by
Sandia National Laboratories
Albuquerque, New Mexico 87185 and Livermore, California 94550

Sandia National Laboratories is a multimission laboratory managed and operated by National Technology and Engineering Solutions of Sandia, LLC, a wholly owned subsidiary of Honeywell International, Inc., for the U.S. Department of Energy's National Nuclear Security Administration under contract DE-NA0003525.

Sandia National Laboratories

Issued by Sandia National Laboratories, operated for the United States Department of Energy by National Technology and Engineering Solutions of Sandia, LLC.

Available to DOE and DOE contractors from
U.S. Department of Energy
Office of Scientific and Technical Information
P.O. Box 62
Oak Ridge, TN 37831

Telephone: (865) 576-8401
Facsimile: (865) 576-5728
E-Mail: reports@osti.gov
Online ordering: http://www.osti.gov/scitech

Available to the public from
U.S. Department of Commerce
National Technical Information Service
5301 Shawnee Rd
Alexandria, VA 22312

Telephone: (800) 553-6847
Facsimile: (703) 605-6900
E-Mail: orders@ntis.gov
Online order: https://classic.ntis.gov/help/order-methods/

SAND2018-10479
Printed September 2018
Unlimited Release

High Fidelity Hybrid Method for In Situ Borehole Stress Determination Final Report

Mathew D. Ingraham[1], R. Charles Choens[1], Thomas A. Dewers[2], Stephen R. Sobolik[3], Jennifer Wilson[1], Courtney G. Herrick[1], Bezelel C. Haimson[4], Moo Y. Lee[1]

[1]Geomechanics Department, [2]Nuclear Waste Disposal Research & Analysis, [3]Geotechnology and Engineering
Sandia National Laboratories
P. O. Box 5800
Albuquerque, New Mexico 87185-MS1033

[4]Materials Science and Engineering
University of Wisconsin
1509 University Ave
Madison, WI 53706

Abstract

The state of stress in the earth is complicated and it is difficult to determine all three components and directions of the stress. However, the state of stress affects all activities which take place in the earth, from causing earthquakes on critically stressed faults, to affecting production from hydraulically fractured shale reservoirs, to determining closure rates around a subterranean nuclear waste repository.

Current state of the art methods commonly have errors in magnitude and direction of up to 40%. This is especially true for the intermediate principal stress. This project seeks to better understand the means which are used to determine the state of stress in the earth and improve upon current methods to decrease the uncertainty in the measurement. This is achieved by a multipronged experimental investigation which is closely coupled with advanced constitutive and numeric modeling.

ACKNOWLEDGMENTS

The authors would like to extend their thanks to Michelle Williams, Perry Barrow, Mike Hileman, and Aron Robbins for their assistance in performing the laboratory tests required for this research. Bezalel Haimson and Cecilia Cheung were also fundamental in performing this work through the subcontract placed with the University of Wisconsin, where all of the drilled under stress tests were performed. We would also like to thank Carl Jacques and Enrico Quintana for their assistance in generating high resolution CT scans of samples. We would also like to thank Tracy Woolever for helping to manage the funds for this project and Erik Webb for direction and guidance on the project.

TABLE OF CONTENTS

FIGURES

TABLES

NOMENCLATURE

Abbreviation	Definition
Abbreviation	Definition
CT	X-Ray Computed Tomography
SWG	Sierra White granite
3D	3 Dimensional
UCS	Unconfined Compressive Strength
E	Young's Modulus
ν	Poisson's Ratio
LVDT	Linear Variable Differential Transformer
σ_H	Maximum Horizontal Stress
σ_v	Vertical Stress
σ_h	Minimum Horizontal Stress
σ_1	Maximum Principal Stress
σ_2	Intermediate Principal Stress
σ_3	Minimum Principal Stress
AE	Acoustic Emission
SWESI	Sandia Wellbore Experimental Simulation
UV	Ultraviolet
P_p	Pore Pressure or Borehole Pressure
2D	2 Dimensional
SEM	Scanning Electron Microscope
VTI	Transversely Isotropic
ε	Strain
σ	Stress
γ	Shear Strain
G	Shear Modulus
PERP	Perpendicular to bedding
PARA	Parallel to bedding
45D	45° to bedding
σ_B^{Kir}	Circumferential stress from Kirsch solution
ΔP	Pressure differential
$\sigma^{\Delta T}$	Thermal stress
σ_B^{VTI}	Circumferential stress at failure
P_c	Confining pressure

Abbreviation	Definition
σ_A	Axial stress
I_1	First stress invariant
J_2	Second deviatoric stress invariant
ε_v^P	Plastic compaction volume strain
γ^P_{equiv}	Equivalent plastic shear strain
$\bar{\Theta}$	Lode angle
Ψ	Triaxial extension/compression strength ratio
s	Average pressure

1. PREFACE

This document comprises a multipronged experimental investigation into intermediate principal stress dependence on constitutive response, borehole breakout and determination of in situ stresses from borehole breakout data. Each section of the paper addresses a different area of this investigation, with a short summary and relevant background for each section preceding the methods, results and discussion of said results for each section. This format was chosen to simplify the work for the reader, so that each part of the work was relatively self-contained. Most if not all of these sections will be turned into a peer reviewed journal article, and in many cases the sections were developed from drafts of these articles.

Two different rocks were used in this work: (1) Sierra White granite (SWG) for which most of the characterization was performed as part of this work, accounting for the majority of the testing. This material was selected for two reasons, first it is a nearly isotropic and ideal rock, thus the analysis of the response with respect to intermediate principal stress and borehole breakout should be straightforward. The second reason it was selected was because at the time of the project inception, Deep Borehole nuclear waste disposal was of great interest and this rock would be a surrogate for the type of rock that would be ideal for siting a deep borehole waste repository.

(2) The second rock selected was Mancos Shale. The baseline data for this was developed as part of another project at Sandia, and it was selected because of the existing experience with the rock and the relevance of the rock to the petroleum industry, who should be interested in the results of this work.

It should be noted that all of the work presented in this document assumes a sign convention where compressive stresses and strains are positive, unless otherwise noted. This is counter to the typical engineering convention, but it is the standard for geomechanics. Also note that in most circumstances (unless otherwise noted) assumes a strike slip faulting regime where the stresses are oriented such that $\sigma_H \geq \sigma_v \geq \sigma_h = \sigma_1 \geq \sigma_2 \geq \sigma_3$. This means that it is assumed that $\sigma_H = \sigma_1$, $\sigma_v = \sigma_2$, $\sigma_h = \sigma_3$.

2. TRUE-TRIAXIAL DEFORMATION OF GRANITE: EXPERIMENTS AND MODELING OF POST-YIELD AND FAILURE BEHAVIORS

2.1. Section Summary

Stress states in the subsurface can be characterized in terms of three principal stresses, yet the abundance of mechanical testing on subsurface geomaterials is conducted under triaxial states of stress with two principal stresses equal. We conduct true triaxial tests using Sierra White Granite to measure the influence of the intermediate principal stress on post-yield and failure constitutive behavior. Loading of right cylindrical (for axisymmetric compression tests with Lode angle equal to 30°) and parallelepiped specimens (for Lode angles > 0° and < 30°) were performed at constant Lode angle until failure manifesting as through-going shear bands. The occurrence of yielding was determined by either the onset of dilatancy, measured differences between loading modulus and elastic modulus determined from unload-reload cycles conducted throughout the testing, or both. Failure from tests at constant Lode angle exhibit linearity when plotted in cylindrical Lode coordinate space, and a number of failure criteria including Mohr-Coulomb, William-Warnke, and Matsuoka-Nakai-Lade-Duncan functions are compared with similar goodness-of-fit. A generalized isotropic elasto-plastic constitutive model combining non-associative plasticity, nonlinear elasticity, and phenomenological yield criteria (representing microcracking and pore collapse, e.g.) is applied to the experimental data set. For Sierra White Granite, we find that a degree of non-associativity and kinematic hardening is necessary to describe the observed behavior, including the post-yield "turnaround" accompanying dilatancy. The extent of non-associativity is shown to depend on intermediate stress. The observed constitutive behavior is discussed considering renewed interest in borehole breakouts and estimations of in situ states of stress for subsurface engineering endeavors.

2.2. Introduction

The state of in situ stress influences all subsurface engineering activity, from mining and petroleum resource extraction to deep borehole and reservoir waste storage. The recent JASON report (2014) points to the need for better defining of realistic subsurface states of stress and associated influence on rock deformation. More particularly, renewed interest in disposal of nuclear waste in deep boreholes (Brady et al. 2009), and geothermal recovery of energy from granitic batholiths (INL 2006), point to the need to engineer and control near-borehole environments in granitic rocks. Previous experience with the KTB borehole in crystalline rock (Emmermann and Lauterjung, 1997, Borm et al. 1997, Brudy et al. 1997) shows that drilling at great depth can be problematic from borehole breakouts, which are influenced by magnitude and direction of intermediate stress (Chang and Haimson, 2000). Additionally, difficulty in drilling deep boreholes in granitic terrains is exacerbated if a significant offset in the principal lateral stresses (intermediate principal stress vs minimum principal stress) occurs (Brudy and Zoback, 1999). Therefore, there is increasing interest in better understanding the role of intermediate principal stresses in deformation of low porosity igneous rock.

We investigate the mechanical response of "Sierra White Granite", a Cretaceous granodiorite from the Sierra Nevada of western California, USA (Bateman and Sawka, 1981), to conditions relevant to deep boreholes including the influence of intermediate principal stress. Samples of granite are subject to loading at constant Lode angle, a function of the second and third deviatoric stress invariants, through yielding and ultimately to failure. The loci of peak stresses are compared to

failure criteria that include intermediate principal stress. We examine post-yield constitutive behavior by means of the Kayenta generalized plasticity model (Brannon et al. 2009), employed via a single element finite element driver for comparison to experimental results up to and including failure. We find that a constitutive model combining a "mixed" isotropic and kinematic hardening and non-associative three invariant-dependent yield and plastic potential functions describes the observed deformation to a satisfactory degree. While an intermediate stress-dependent Mohr-Coulomb criterion describes much of the failure response, we present modeling results in terms of the Willam-Warnke criterion (Brannon et al, 2009, William and Warnke, 1975)) which avoids vertices occurring in the Mohr-Coulomb model at axisymmetric compression conditions. The true-triaxial behavior of Sierra White granite is discussed in the context of borehole breakouts in deep boreholes and interpretations of borehole stresses.

2.3. Background

2.3.1. Borehole Breakouts and Stress States in the Earth's Subsurface

Although a variety of methods exist for directly or indirectly "measuring" in situ stress, by far the dominant means are borehole methods wherein hydraulic fractures or breakouts are induced across a wellbore interval (Heidbach et al., 2016, Heidback et al., 2010). Errors in magnitude and orientation from these methods can be as high as 30 to 40% (JASON, 2014)) and result from rock heterogeneity, anisotropy, and uncertainty in the physics of rock failure. Much understanding in subsurface stress derives from breakout observations and measurements with relatively simplistic views on rock strength and heterogeneity (i.e. isotropic properties, Mohr-Coulomb behavior, and that stress can be averaged over spatial volumes (Zoback et al., 1985)), that are more-or-less borne out in laboratory studies or studies of stress in boreholes (Haimson and Herrick, 1985,1986, Lee and Haimson, 1993, Hickman et al., 1985). More recent examination of borehole breakouts utilizes numerical simulation to surmount issues with heterogeneity, spatial variability, and coupled thermo-mechanical and thermo-poro-elastic processes (Shen, 2008, Gomar et al., 2014, Dewers et al., 2018). These models show the importance on constitutive models that are dependent on the intermediate principal stress to adequately characterize and simulate in situ stress and borehole failure.

2.3.2. Experimental Testing Under True-Triaxial Conditions

Seminal experiments were performed under true triaxial states of stress by Mogi (1971a, 1971b) on westerly granite and other rocks. They revealed that the intermediate principal stress has a substantial effect on failure. Since then, true triaxial testing was performed on a variety of sedimentary and metamorphic rock types (ex. Hunsche and Albrecht, 1990, Michelis, 1987, Mogi, 1972, Mogi, 1981). Other work under true triaxial stress was conducted on surrogate materials and on jointed rock (ex. Reik and Zacas, 1978). In the 1990's and early in the 2000's, there was renewed interest in testing low porosity igneous rocks (ex. Chang and Haimson, 2000, Haimson and Chang, 2000). Other experiments were performed under constant lateral strain (in the intermediate principal direction), which resulted in a true triaxial state of stress. However, the intermediate principal stress was determined indirectly, and was not directly controlled (Holcomb and Rudnicki, 2001, Labuz and Papamichos, 1996).

Kwasniewski (2013) compiled a list of true triaxial tests in rock that were reported in the literature. The list includes the type of loading apparatus used, the principal stresses applied, as well as the

maximum ratio of intermediate to minimum principal stresses. These results were compared to a number of failure criteria. It appears that most of the data can be fit relatively well with both the power law criterion proposed by Mogi (1972, 1981), and a 3D version of the Hoek & Brown criterion proposed by Zhang and Zhu (2007). However, the criterion presented by Rudnicki (2008) was not included in their comparison, likely because it would require that experiments be performed at constant Lode angle (under pure shear conditions). To date, the only constant Lode angle tests (under non-axisymmetric conditions) have only been conducted by Ma et al. (Ma and Haimson, 2016, Ma et al., 2017a, 2017b), and Ingraham et al. (2013).

2.4. Materials and Methods

2.4.1. Sierra White Granite

A single block of Sierra White granite was used for preparation of all the specimens used in the present study. This parent block was purchased from Coldspring Inc. and was quarried in Raymond, CA. Per the supplier, uniaxial compressive strength of this rock is 164.6 MPa, and its density is 2.64 g/cc. The rock is an unweathered, nearly homogenous granodiorite, comprised of (from most to least abundant): oligoclase, quartz, orthoclase, biotite, muscovite and a few other trace minerals. The grain size ranges from ~1 to ~3 mm. Preliminary testing performed on the samples yielded an unconfined compressive strength (UCS) of 176.2 MPa, Young's modulus (E) of 48.5 GPa and a Poisson's Ratio (υ) of 0.22.

2.4.2. True Triaxial Testing

Tests reported in this paper were performed in the Sandia National Laboratories Geomechanics Laboratory, utilizing a true triaxial testing system developed by Wawersik et al. (1997) (Figure 2.1A). Standard UCS tests (of right circular cylindrical specimens 50.80 mm long and 25.40 mm in diameter) were performed in a 100 kN uniaxial loading frame. Specimens were jacketed in fully annealed copper foil 0.127 mm in thickness, in the same manner as described by Ingraham et al. (2013a). The true triaxial testing specimens had the following dimensions: 25.40 x 57.15 x 57.15 mm with a tolerance of +/-0.127 mm, and opposite sides are ground to be parallel within 0.0127 mm per mm of length. An image of a jacketed specimen is provided in Figure 2.1B. Specimens were instrumented as in Ingraham et al. (2013a). A strain gage (6.35 mm gage length) was used to capture the strain response in the σ_2 direction (Figure 2.1B, while LVDT pairs were used in both the σ_1 and σ_3 directions (Figure 2.1B). Figure 2.1B also shows the piston jacks which apply σ_2. These utilize pressure in excess of confining pressure (σ_3) to apply stress to one pair of lateral faces of the specimen.

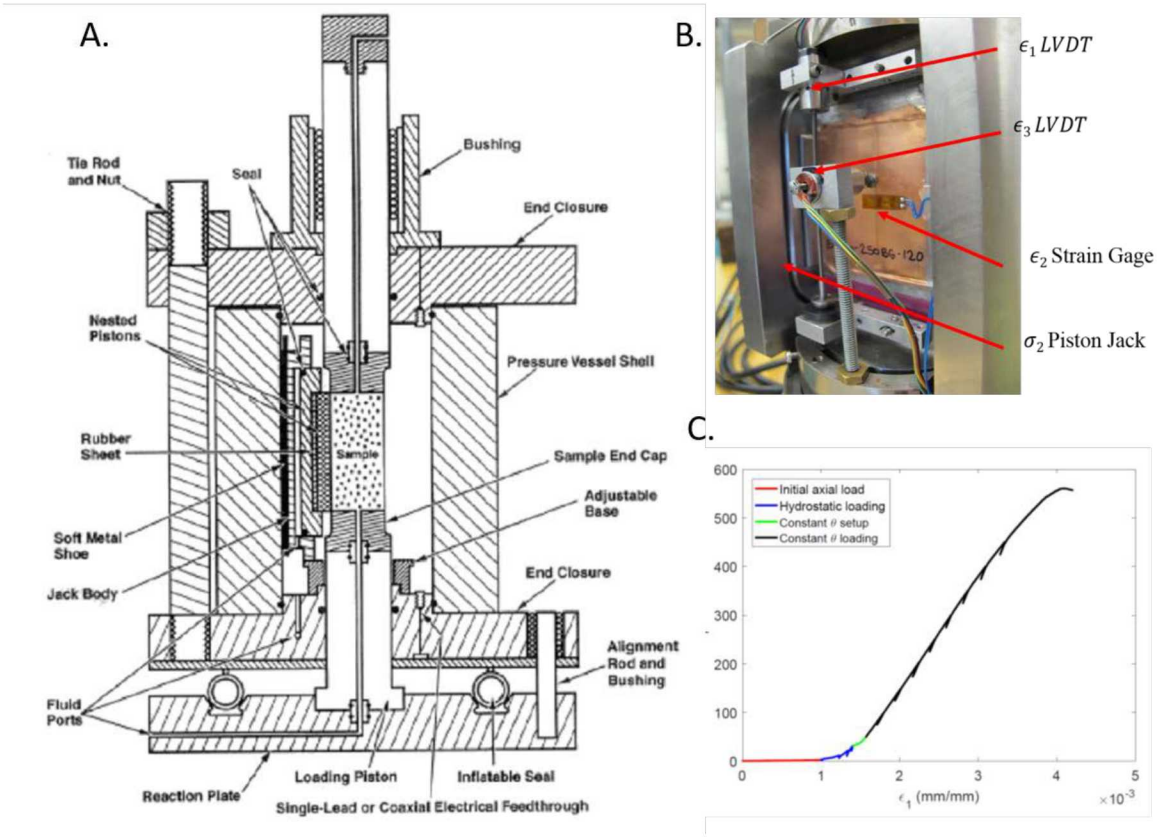

Figure 2.1. A. True-triaxial apparatus. B. Location of sensors on copper-jacketed sample. C. Loading sequence for true triaxial testing plotted as axial stress versus axial strain, involving: an initial axial load (red); a near-hydrostatic loading to close to minimum principal stress values (dark blue); a small adjustment to bring stress state to desired Lode angle (green); followed by Loading at constant Lode angle.

Tests were run under constant Lode angle conditions, but not constant mean stress conditions, as that would have severely limited the stress range that could be accessed, or would have required application of tensile stress in the σ_3 direction. The loading path applied to the specimens in this study is similar to the "novel" loading path described by Ma and Haimson (2016) and Ma et al. (2017a, 2017b). The only difference between the two is the initial loading of the specimens. Our study utilized a pressure difference between confining pressure and the pressure in the jacks, requiring a small non-constant Lode angle section at the end of the hydrostat, whereas Ma et al. were able to test at a constant Lode angle directly from the hydrostat. A loading curve for this work is shown in Figure 2.1C where the different stages of the test are illustrated on the axial stress – strain curve for sample 1T8 in the form of different colors. The red portion of the curve shows the initial axial (σ_1) load applied to the specimen to ensure that the sample is seated inside the pressure vessel. This is followed by a hydrostatic loading portion (blue) where the confining pressure is increased to the desired level for the minimum principal stress (σ_3). During the hydrostatic loading, the axial load is maintained just above the hydrostat to ensure that the specimen remains in contact

with the loading column. Once the desired minimum principal stress was reached, there was a transition in which the constant Lode angle portion of the test was set up (green portion of the curve in Figure 2.1C). This involved increasing the axial load by a set increment depending on the desired Lode angle (increments shown in Table 2.1). The jacks were then applied to the desired intermediate principal stress (σ_2, see Table 2.1 for these values). The specimen was then at the desired Lode angle, and this condition was maintained until failure. The maximum principal stress was increased under displacement control at a rate of 5.72E-4 mm/sec, resulting in a strain rate of 1E-5 mm/mm/sec, shown in black in Figure 2.1C. The intermediate stress was commanded to maintain the Lode angle constant, this means that for each increment of stress in σ_1, σ_2 would increase by some fraction of that stress increase; the specific numbers for each Lode angle for all tests are provided in Table 2.1.

Table 2.1 Loading parameter information for each Lode angle. Stresses were increased hydrostatically to the desired σ_3 then the starting increments were applied, and the specimens were loaded at the stated stress ratio to keep the Lode angle constant during deviatoric testing.

		Starting Increment	
Lode angle	Stress Ratio (σ_1:σ_2)	σ_1 (MPa)	σ_2 (MPa)
0	2:1	5	2.5
16.1	4:1	10	2.5
23.4	8:1	20	2.5

2.4.3. Constitutive Modeling

2.4.3.1. Notation and Lode Coordinates

In this paper, the combination of geomechanics experimentation and continuum mechanics modeling in sections to follow necessitates using different sign conventions. Following uses in the literature (Brannon et al. 2009, Brannon and Leelavanichkul, 2010), we will use an overbar over a quantity to denote the negative of that quantity. For modeling purposes, we will follow the convention that stresses are positive in tension, and refer to principal stresses and strains as $(\sigma_1, \sigma_2, \sigma_3)$ and $(\varepsilon_1, \varepsilon_2, \varepsilon_3)$ respectively, with $(\bar{\sigma}_1, \bar{\sigma}_2, \bar{\sigma}_3)$ and $(\bar{\varepsilon}_1, \bar{\varepsilon}_2, \bar{\varepsilon}_3)$ being the positive counterparts in experimental results. In general, we will refer to $(\sigma_1, \sigma_2, \sigma_3)$ as ordered eigenvalues of the Cauchy stress tensor $\boldsymbol{\sigma}$, i.e. $\sigma_1 \leq \sigma_2 \leq \sigma_3$ so that, in reference to experiments, $\bar{\sigma}_1 > \bar{\sigma}_2 > \bar{\sigma}_3$. Accordingly, we denote $\mathbf{s}$ as the deviator of $\boldsymbol{\sigma}$, with eigenvalues of s_1, s_2, and s_3. We will make use of three independent invariants

$$\begin{aligned} I_1 &= tr\boldsymbol{\sigma} = \sigma_1 + \sigma_2 + \sigma_3 \\ J_2 &= \frac{1}{2}\, tr\boldsymbol{s}^2 = \frac{1}{2}(s_1^2 + s_2^2 + s_3^2) \\ J_3 &= \frac{1}{3}\, tr\boldsymbol{s}^3 = \frac{1}{3}(s_1^3 + s_2^3 + s_3^3) \end{aligned} \qquad (1)$$

To facilitate application of three-invariant plasticity models to the failure and yielding of Sierra White Granite testing results, we will make use of coordinate transformations to Lode coordinate space (Figure 2.2A). Lode coordinates are geometrically accurate or isomorphic with respect to stress invariants (Brannon and Leelavanichkul, 2010), do not distort yield and failure surfaces, and

thus are best for fitting the test data for modeling purposes. The three principal stress eigenvalues (σ_1, σ_2, σ_3) (and the over-barred counterparts, with some modification) can be expressed in terms of invariants (I_1, J_2, J_3) or Lode cylindrical coordinates (r, θ, z) as (Brannon and Leelavanichkul, 2010)

$$\begin{aligned}\sigma_1 &= \frac{z}{\sqrt{3}} + \frac{r}{\sqrt{2}}\left[\cos\theta + \frac{\sin\theta}{\sqrt{3}}\right] \\ &= \frac{I_1}{3} + \sqrt{J_2}\left[\cos\theta + \frac{\sin\theta}{\sqrt{3}}\right] \\ \sigma_2 &= \frac{z}{\sqrt{3}} - \sqrt{\frac{2}{3}} r \sin\theta \\ &= \frac{I_1}{3} - \frac{2}{\sqrt{3}}\sqrt{J_2}\,\sin\theta \\ \sigma_3 &= \frac{z}{\sqrt{3}} - \frac{r}{\sqrt{2}}\left[\cos\theta - \frac{\sin\theta}{\sqrt{3}}\right] \\ &= \frac{I_1}{3} - \sqrt{J_2}\left[\cos\theta - \frac{\sin\theta}{\sqrt{3}}\right]\end{aligned} \qquad (2)$$

with Lode coordinates defined as

$$r = \sqrt{2J_2}, \quad \sin 3\theta = \frac{J_3}{2}\left(\frac{3}{J_2}\right)^{3/2}, \quad z = \frac{I_1}{\sqrt{3}} \qquad (3)$$

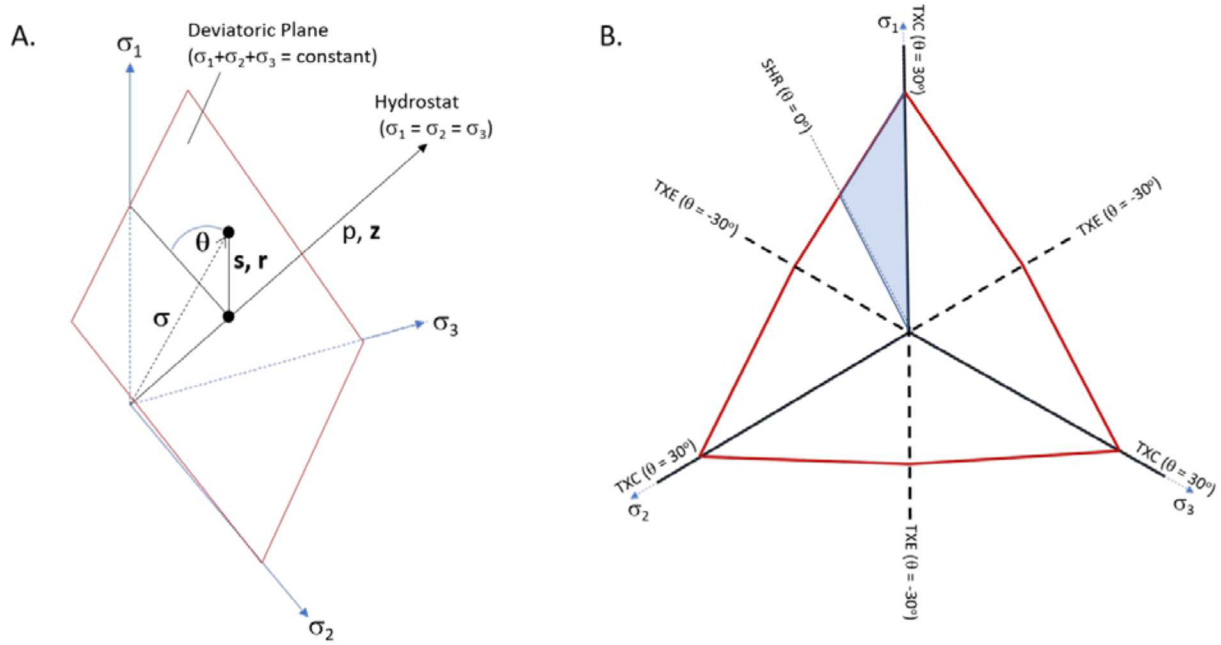

Figure 2.2. A. Stress space and coordinate transformation to cylindrical Lode coordinates. B. Octahedral profile in stress space (looking down the hydrostat) and rotational symmetry of Mohr-Coulomb failure surface of isotropic geomaterials.

Here θ is referred to as the Lode angle, and the definition in (3) is selected for convenience with working with the constant-Lode angle experiments. As discussed in the experimental section

above, our tests are conducted at constant Lode angle, and the *r-z* plane at a given constant θ is referred to as the meridional profile. Figure 2.2A shows the relationship between the (σ_1, σ_2, σ_3) and cylindrical (r, θ, z) coordinates where the z and hydrostat (i.e. pressure axis) coincide, r is in the deviatoric plane, and q is the angle revolved around the z axis.

Isotropic materials such as many granites possess symmetry properties such that yield and failure surfaces are reflected around the hydrostat or z-axis in stress space. The r-θ plane at constant z is referred to as the Π-plane, and the profile of yield or failure surfaces at a given z value is called because of the reflection symmetry, the octahedral profile (Figure 2.2B). An example octahedral profile that will be useful later in this paper is shown by the red lines in Figure 2.2B, an example of Mohr-Coulomb failure. As rocks are generally stronger in triaxial compression (TXC) than in triaxial tension (TXE), the distance from the z-axis to the failure profile is longer for TXC ($\theta = 30^o$) axes than for TXE ($\theta = -30^o$) axes, which gives this particular octahedral profile its distinctive triangular appearance. The SHR line corresponds to so-called pressure-shear loading, (simple shear with superimposed hydrostatic loading), which is relevant to subsurface stress states and deformation. For our purposes, with constraints given by the experimental apparatus, we will be concerned with stress states resolved onto the shaded region in Figure 2.2B, corresponding to stress states between TXC and SHR, or correspondingly, θ values between $+30^o$ and 0^o.

2.4.3.2. The Kayenta Model

Kayenta (Brannon et al., 2009) is a generalized elasto-plastic constitutive model that describes non-linear elasticity, yielding, and failure of a large class of rock-like materials. Yielding of geomaterials can take the form of a variety of inelastic responses including microcrack growth and pore collapse, and these are handled phenomenologically with *Kayenta* by a single yield surface. Although is meant to handle isotropic materials, it includes anisotropy associated with joint sets and kinematic hardening, the latter which will be shown to be important to describe volume strain behavior following the onset of dilatancy leading to failure. *Kayenta* contains many features relevant to deformation of porous geomaterials (Brannon et al., 2009, Regueiro et al., 2004, Foster et al., 2005) (i.e. pore collapse and 'cap'-plasticity (Sandler, 2005), elastic-plastic coupling and damage effects (Dewers et al., 2014), softening, rate-dependency, Weibull effects, etc.), and although some of these are certainly relevant to granite deformation, we will concern our description to aspects of *Kayenta* relevant to aspects important to experimental behavior in this paper.

To describe yielding, *Kayenta* employs a yield function $f(\boldsymbol{\sigma}, \boldsymbol{\alpha}, \kappa)$ such that elastic conditions satisfy $f < 0$, yielding occurs at $f = 0$, and translation of f in stress space from initial yielding to failure is controlled by the state variable κ (relating to extent of isotropic hardening) and the backstress tensor $\boldsymbol{\alpha}$, which controls the extent of kinematic hardening. The yield criterion used by *Kayenta* contains a "shear-limiter" or meridional failure function F_f, a so-called "cap" function F_c, and a Lode-angle function $\Gamma(\theta)$ (Brannon et al., 2009), which, in Lode coordinates, combines as

$$r = \sqrt{2}\left[\left(F_f\left(\sqrt{3}\,z\right) - N\right)\sqrt{F_c\left(\sqrt{3}\,z, \kappa\right)}\right]/\Gamma(\theta) \qquad (4)$$

Here N is a parameter equal to the initial offset of the yield surface from the limit or failure surface, and so controls the extent of upward translation of the yield surface in the meridional plane during kinematic hardening. The backstress tensor $\boldsymbol{\alpha}$ is a deviatoric tensor quantifying the degree that the

stress tensor on the yield surface is shifted associated with non-isotropic kinematic hardening. Originally used in plasticity to describe the Bauschinger effect in metals, in geomaterials it has been used to quantify the extent of dilatancy in rocks (Dienes, 1975) and unloading effects in sands (Lade and Inel, 1997). Initially zero, upon yielding it evolves proportionally with the plastic strain rate as described in reference (Brannon et al., 2009).

The so-called limit or failure surface as employed in *Kayenta* takes the form

$$r = \sqrt{2}F_f \,/\Gamma(\theta) \qquad (5)$$

where F_f has exponential and linear terms in $\bar{I}_1$ to describe a variety of material responses (i.e. linear being Mohr-Coulomb materials and exponential representing the approach to pressure-insensitivity of Von Mises materials):

$$F_f(I_1) = a_1 - a_3\, e^{-a_2\bar{I}_1} + a_4\bar{I}_1 \qquad (6)$$

To model Lode angle effects in Γ, Kayenta makes uses of the ratio of material strength in compression versus that in extension, termed ψ. Of the options for Γ, two are relevant to what we explore in this paper; these are:

Mohr-Coulomb: $\Gamma(\theta) = \frac{2\sqrt{3}}{3-\sin\varphi}\left(\cos\bar{\theta} - \frac{\sin\varphi\sin\bar{\theta}}{\sqrt{3}}\right)$ (7)

and

William-Warnke: $\Gamma(\theta) = \frac{4\left(1-\Psi^2\right)cos^2\alpha^* + (2\Psi-1)^2}{2\left(1-\Psi^2\right)cos^2\alpha^* + (2\Psi-1)\sqrt{4\left(1-\Psi^2\right)cos^2\alpha^* + 5\Psi^2 - 4\Psi}}$ (8)

In (7), ϕ is the angle of internal friction (in a typical Mohr diagram, $tan\phi = \mu$, the friction coefficient) and is related to Ψvia $\sin\emptyset = 3\frac{(1-\Psi)}{(1+\Psi)}$. In (8), the angle α^*equals $\frac{\pi}{6} + \bar{\theta}$. To maintain the necessary convexity in the octahedral profile, $\frac{1}{2} \leq \Psi \leq 2$.

The a_i parameters in (6) can be chosen to map onto classic models for rock failure. For example, for Mohr-Coulomb behavior (Brannon et al., 2009):

$$a_1 = \left(\frac{2\sqrt{3}}{3-\sin\emptyset}\right)S_0\cos\emptyset\,, a_2 = 0, a_3 = 0, a_4 = \left(\frac{2\sqrt{3}}{3-\sin\emptyset}\right)\frac{sin\emptyset}{3} \qquad (9)$$

where S_0 is the cohesion in the well-known Mohr-Coulomb failure criterion.

Finally, to model observed yield data discussed below, we will use the cap-surface function for Fc in (4) to capture the decreasing pressure dependence of the yield surface relative to the failure surface (this is shown below). Our data are inconclusive as to the existence of a cap surface for Sierra White Granite, which may well exist despite the low porosity of about .01 or less, but we use this functionality to obtain a better 'fit" to yield data. In *Kayenta*, F_c depends on the state variable $\bar{\kappa} = -\kappa$ and the value of $\bar{I}_1$ where inelastic pore collapse initiates (termed $\bar{X}$) and follows the Pelessone function (1989)

$$F_c(\bar{I}_1, \bar{\kappa}) = 1 - \frac{(\bar{I}_1 - \bar{\kappa})(|\bar{I}_1 - \bar{\kappa}| + (\bar{I}_1 - \bar{\kappa}))}{2(\bar{X} - \bar{\kappa})^2} \qquad (10)$$

This function is such that F_c = 1 if $\bar{I}_1 < \bar{\kappa}$ and is a decreasing elliptical function between 1 and 0 otherwise.

In addition to the post-yield relevant functions, *Kayenta* employs a number of functions to describe nonlinear elasticity and elastic moduli degradation and we discuss this below.

2.5. Results and Discussion

2.5.1. Elastic Behavior and Yield Determination

Stress-strain data for all tests are given in the appendix. All specimens demonstrate a nearly linear elastic response to the application of stresses up to approximately 90% of the peak stress applied. An example is shown in Figure 2.3, for an unconfined compression test with Lode angle = 30°. Following an initial nonlinear portion, the axial stress-strain curve appears nearly linear. Recognizing yield in such a case can be equivocal; plastic yield associated with the various inelastic microstructural processes can be inferred from the onset of acoustic emissions (AE), degradation of elastic moduli, differences between loading and unload-reload loops, onset of dilatancy, and a change in convexity of certain stress-strain relationships (Ingraham et al., 2013b, Dewers et al., 2017). Obtaining AE data was beyond the scope of this study, so to determine yield we used the behavior of unload-reload loops and measured dilatancy as measures to determine yield. Even then, some of our yield estimates come with uncertainty, as strain sensors may not respond equally to changes in loading direction. Beyond the elastic region, sample response to

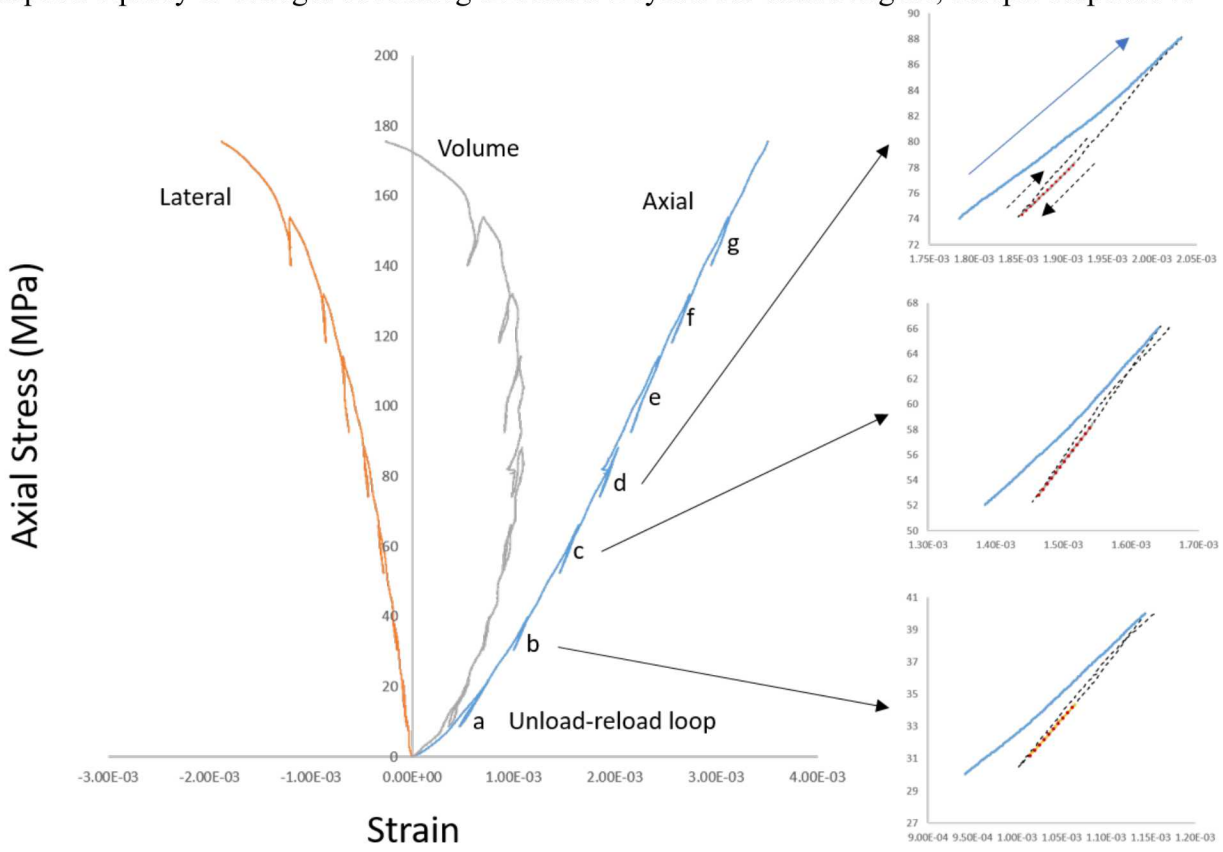

Figure 2.3. Example of unconfined uniaxial compression testing results plotted as axial stress versus lateral, volume, and axial strains. Inset shows view of unloading-reloading loops used to determine elastic modulus pre- and post-yielding, near the "turn-around" in volume strain marking the onset of dilatation.

Table 2.2 Details of failure and the failure features for each test compared with the failure feature angle as predicted by theory, specimens 1A and 3A were cylindrical specimens tested uniaxially. Note: band angles are measured between σ_1 and the band normal.

	Failure			Initial Yield			
Test	I_1	(J2)^.5	θ	I1	(J2)^.5	θ (degrees)	Measured Band Angle (degrees)
1T9	447.2	143.7	0.0	177.6	54.0	0.0	60.0
1T6	449.4	144.7	0.0	210.4	64.9	0.0	71.0
1T11	471.7	140.3	0.0	269.2	72.7	0.0	
1T10	668.8	205.8	0.0	296.1	81.7	0.0	
1T3	425.0	170.7	0.3	167.7	63.6	16.1	70.0
1T7	623.2	238.4	0.3	255.6	85.3	0.3	68.0
1T2	780.6	287.4	0.3	331.2	100.4	0.3	69.0
1T4	360.1	167.0	0.4	150.9	65.7	0.4	68.0
1T5	526.1	230.0	0.4	236.5	89.7	0.4	73.0
1T8	687.4	289.1	0.4	307.0	105.2	0.4	72.0
1A	175.6	101.4	0.5	74.5	43.0	0.5	Axial
3A	167.4	96.6	0.5	109.8	63.4	0.5	Axial
MD10	289.4	149.8	0.5	172.4	82.2	0.5	
MD30	476.7	223.2	0.5	290.4	115.6	0.5	

load switches from compactant to dilatant, likely due to formation and propagation of microcracks within the sample. These microcracks continued to propagate, and eventually coalesced into a through-going localized macroscopic shear feature, causing the specimen to fail. This was not confirmed microstructurally in this study; however, this is consistent with well-documented failure modes in high strength, low porosity rocks like granite (e.g. Tapponnier and Brace 1976, Zoback and Byerlee, 1975). The angle of the shear features formed in each specimen are presented in Table 2.2.

In Figure 2.3, dilatancy can be recognized by the "turn-around" in volume strain, which occurs around 80 MPa axial stress, and accompanies a subtle change in convexity of the axial stress-axial strain curve. The unload-reload loops are labelled as a-g, and are defined as small decreases in stress followed by a return. These loops are useful in measuring changes in elastic properties post yielding, as, according to plasticity theory, once yielding occurs, stress remains on the yield surface with hardening as load increases, and decreases in stress unload into the elastic regime. Yielding commences once stress conditions reload to the yield surface. Hysteresis in unload-reload loops associated with piston and o-ring friction can give rise to a "loop"-like configuration (Dewers et al., 2017) particularly near the initial portions of unloading and re-loading, and this can be seen in the enlarged images of the three unload-reload cycles in Figure 2.3. The slope of the linear portion demarked with red corresponds to the Young's Modulus, E, which changes from: 35.4 GPa for a; 63.1 GPa for b; 69.9 GPa for c; 66.7 GPa for d; 66.8 GPa for e; 66.1 GPa for f; and 67.2 GPa for g. The increase in E from a to c is associated with nonlinear elasticity. Following unload-reload loop c, there is a slight decrease in E at loop d, and this corresponds to the onset of dilatancy in the

volume strain curve. This (albeit) slight drop in modulus is very likely associated with onset of yielding and commensurate increase in plastic strain. The degradation in moduli associated with plastic straining is termed elastic-plastic coupling (Brannon et al., 2009, Dewers et al., 2018, Dewers et al., 2014) and can be tricky to discern from nonlinear elasticity – increases in moduli with increase in stress can be offset by drops in moduli due to plastic straining. Here, such effects appear to be minor and we will ignore elastic-plastic coupling (such effects are important in more porous geomaterials such as sandstone (Dewers et al., 2014).

The onset of dilatancy here coincides with the small drop in Young's Modulus, so the two methods for recognizing yield agree. This is the case for low confining pressure tests, but as mean stress $\overline{\sigma}$ increases, dilatancy becomes more difficult to determine as the volume strain turn around becomes less evident. We will use small drops in moduli, dilatancy, and changes in convexity to together to derive best estimates of yielding for all tests and these are given in Table 2.2.

2.5.2. Failure and Yield Criteria

In order to determine if failure of Sierra White granite is affected by the intermediate principal stress, we examine peak stress data in both the maximum-intermediate principal stress ($\overline{\sigma_1} - \overline{\sigma_2}$) plane (Figure 2.4A) and in $\bar{r}, \bar{z}$ meridional (i.e. constant $\bar{\theta}$) space (Figure 2.4B). It is evident in Figure 2.4A in the data sets of $\sigma_3 = 5$ and 17 MPa that as the intermediate stress increases, the shear stress at failure first increase to a maximum, then decrease as the intermediate stress continue to increase. This behavior is commonly reported for rocks subjected to true triaxial states of stress (e.g. Lee and Haimson, 1993, Mogi, 1971a,b, Zhang and Zhu, 2007, Ma and Haimson, 2016, Ma et al., 2017a,b, Mogi, 1967). Looking at failure in the $\bar{r}, \bar{z}$ plane (Figure 2.4B), as the Lode angle decreases, the shear stress at failure decreases (assuming the same mean stress).

This work compares favorably with the work of Mogi (1967) on Westerly granite, where the effect of intermediate principal stress on the failure of granite was first reported. While the work of Mogi only examines the extremes of the Lode angle (axisymmetric compression, $\sigma_2=\sigma_3$, and axisymmetric extension, $\sigma_2=\sigma_1$), the same trend is seen as in the current work; as the Lode angle decreases (moves towards extension), the Mises stress required to fail the specimen decreases. This effect magnifies as the mean stress increases.

From (6), best-fit lines shown in Figure 2.4B for failure surfaces are linear, with
$\{a_1, a_2, a_3, a_4, \Psi\}$ = {21 MPa, 0, 0, 0.449 MPa^{-1}, 0.599} for the Mohr-Coulomb (7) model and
$\{a_1, a_2, a_3, a_4, \Psi\}$ = {27 MPa, 0, 0, 0.422 MPa^{-1}, 0.598} for the Willam-Warnke (8) model. The fitting procedure was performed in $\bar{r}, \bar{\theta}, \bar{z}$ space and returns R^2 greater than 0.99; the Willam-Warnke model is shown plotted in this space in Figure 2.5A.

To find the corresponding yield surface for each failure model, we applied (4) to the yield estimates in Table 2.2. Using values for a_i and Ψ given above, we find:
$\{\bar{X}, \bar{\kappa}, \bar{N}\}$ = {625 MPa, 1.0 MPa, and 13.0 MPa} for the Mohr-Coulomb (7) model and
$\{\bar{X}, \bar{\kappa}, \bar{N}\}$ = {625 MPa, 1.0 MPa, and 18.5 MPa} for the Willam-Warnke (8) model. This fitting procedure is relatively insensitive to the values of $\bar{X}$, $\bar{\kappa}$ chosen, and this is because the cap model used is more sensitive to the choice of these parameters at stress values closer to the hydrostat. As with the failure surface fits, this was done in in $\bar{r}, \bar{\theta}, \bar{z}$ space and returns R^2 greater than 0.99. The Willam-Warnke fit is displayed in this space in Figure 2.5B.

Both yield and failure surfaces for both models are shown in stress space in Figure 2.5C (for Willam-Warnke) and 5D (for Mohr-Coulomb) along with the relevant data used for fitting. The octahedral profiles have a similar triangular shape (the octahedral profile for the Mohr-Coulomb model is shown looking "down" the hydrostat in Figure 2.2B. The Willam-Warnke model was

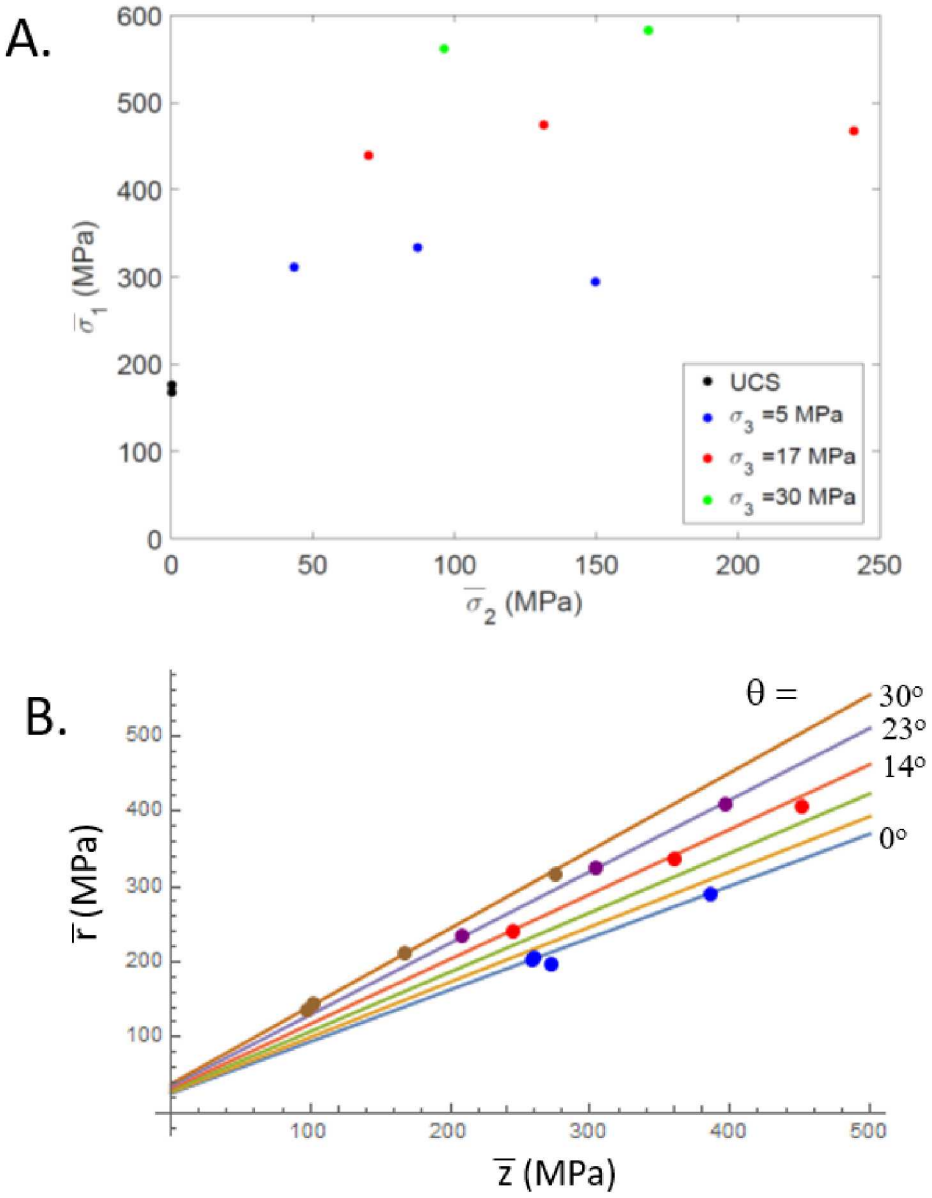

Figure 2.4. Peak stresses from testing of Sierra White Granite. A. Plot of peak stresses in the space of maximum and intermediate principal stresses. C. Failure data plotted in $\bar{r} - \bar{z}$ space, contoured for Lode angle. Lines are best-fit linear regressions to data.

originally developed for concrete (William and Warnke, 1975) but is found to be computationally useful for finite element simulations and an improvement over the Mohr-Coulomb model due to the absence of vertices at ASC conditions ($\theta = 30^o$) which can be numerically costly. The fitting to both failure and yield data are essentially identical, and we will use the Willam-Warnke approach in our Kayenta modeling to follow in a later section.

Recent models for yielding and failure use a Ψ function that varies with pressure, such that the meridional profile can vary from more triangular in shape at low mean stresses to more circular in shape at high mean stresses, as is observed for porous geomaterials such as sandstone (Ingraham et al., 2013a). An example is the modified Matsuoka-Nakai-Lade-Duncan (MNLD) criterion proposed by Rudnicki (2008, 2017) and applied to sandstones by Ma et al. (2017a). The MNLD criterion requires constant Lode angle tests, which are rarely performed. The MNLD failure criterion maps onto

$$\sqrt{\frac{4}{27}}A(\bar{\sigma})\sin(3\,\bar{\theta})\left(\frac{\bar{\tau}}{\tau_0(\bar{\sigma})}\right)^3+\left(\frac{\bar{\tau}}{\tau_0(\bar{\sigma})}\right)^2-1=0 \qquad (11)$$

where $\bar{\tau}\,equals\,\sqrt{\bar{J}_2}$ and $\bar{\sigma}$ is mean stress. $A(\bar{\theta})$ and $\tau(\bar{\theta})$ are calibration functions such that for $-1 \le A(\bar{\theta}) \le 1$, (11) has real roots with the root closest to unity being relevant for solution. For SHR ($(\bar{\theta}=0)$ loading, (11) yields $\bar{\tau}=\tau_0$ such that this function can be determined from SHR loading. From the data in Table 2.2, we find

$$\tau_0(\bar{\sigma}) = 0.890\,\bar{\sigma} + 11.604 \qquad (12)$$

and together with (11) results in

$$A(\bar{\sigma}) = 5.0e^{-6}\bar{\sigma}^2 - 0.0008\bar{\sigma} - 0.95 \qquad (13)$$

which is shown in Figure 2.6A. The quadratic function is problematic (this should not be extrapolated beyond the range of stresses used in the fitting) but provides a reasonable approximation for our purposes. Table 2.3 details the results of fitting the data with the MNLD criterion.

Table 2.3 Fitting parameters for parameterizing the failure criterion defined by Rudnicki (2008). Note that tests run in pure shear are not included in this table as these tests are used to parameterize the function, therefore the fit is perfect. Units for all values of *τ* in this table are MPa.

	Calculated *A*	Fit *A*	τ_0	Calculated τ	Actaual τ	τ Difference
1A	-0.989	-0.984	63.76	100.2	101.8	1.6
3A	-0.989	-0.983	61.13	95.9	96.6	0.7
1T2	-0.844	-0.824	242.65	285.7	287.5	1.8
1T3	-0.987	-0.967	137.40	169.5	170.8	1.3
1T4	-0.975	-0.978	118.20	167.6	167.0	-0.6
1T5	-0.945	-0.941	167.32	229.0	230.0	1.0
1T7	-0.925	-0.905	196.07	236.8	238.4	1.6
1T8	-0.918	-0.875	215.07	281.0	289.2	8.2

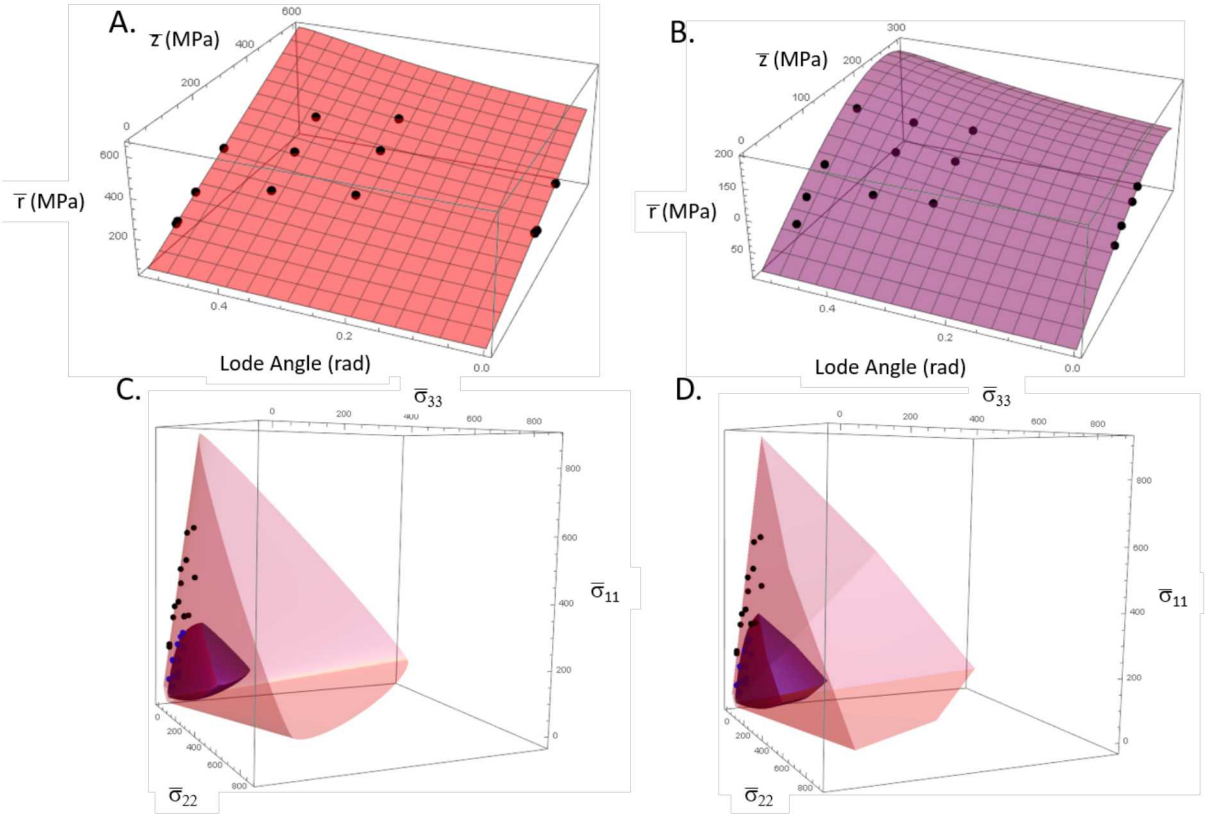

Figure 2.5. A. Fit of William-Warnke failure envelope to peak stress data in Lode coordinate space. B. Fit of yield surface to estimations of yield stresses plotted in Lode coordinate space. C. William-Warnke failure (red) and yield (purple) surfaces plotted in stress space. D. Mohr-Coulomb failure (red) and yield (purple) surfaces plotted in stress space.

A plot of the MNLD failure surface in stress space is given in Figure 2.6B, along with similar views for the Mohr-Coulomb model in 6C and the Willam-Warnke model in 6D at the same octahedral profile. Note that the goodness of fit for all models is similar, and they all possess a similar triangular octahedral profile. We conclude that, while it is likely that Sierra White Granite failure at higher mean stresses would probably require a mean stress-dependent Ψ-like function as provided by the MNLD formulation, our data set is well-described by failure surfaces with constant Ψ.

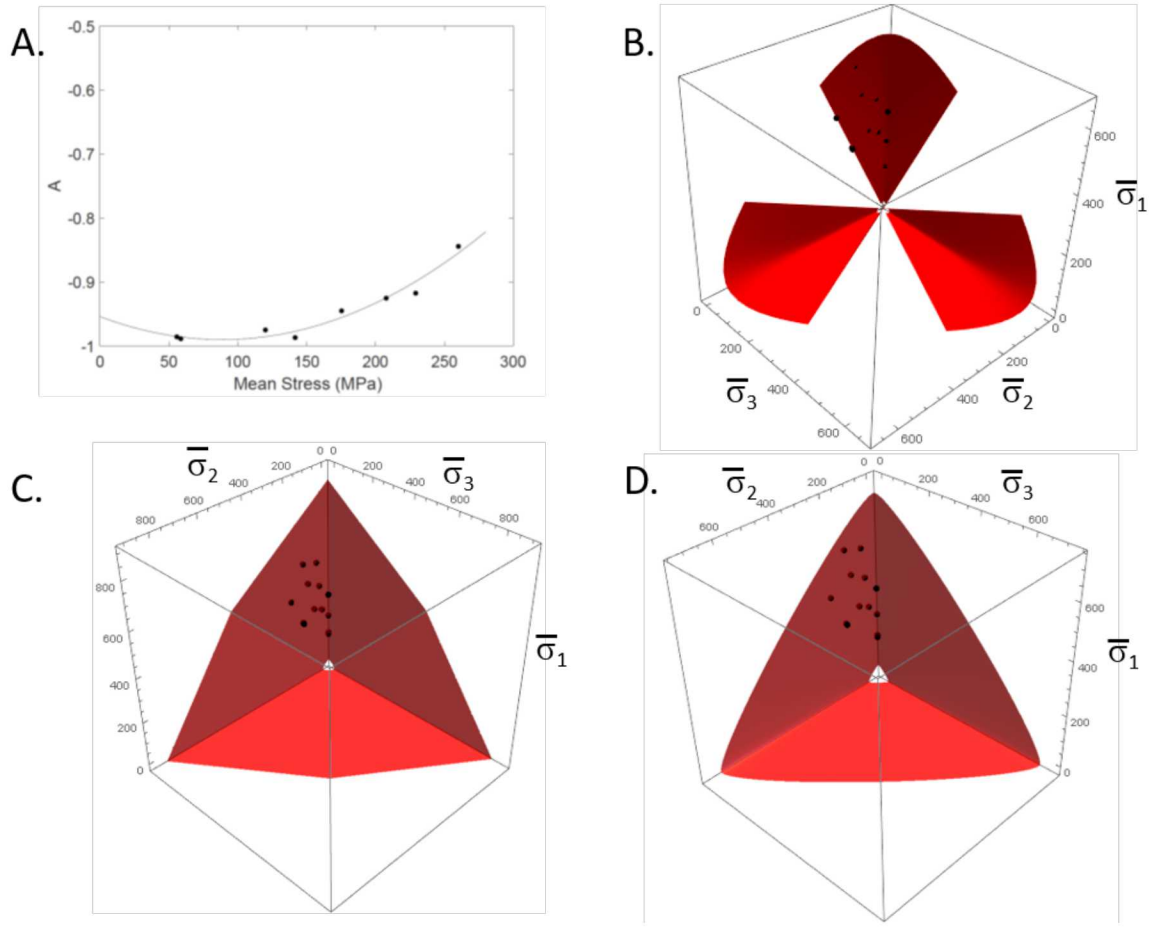

Figure 2.6. A. Fit of data to *A* term in the MNLD failure envelope. B. Plot of MNLD failure envelope in stress space with superimposed peak stress values. C. Mohr-Coulomb failure envelope in stress space. D. Willam-Warnke failure envelope, looking down hydrostat for comparison.

2.5.3. A check for non-associativity

One controversial aspect of elasto-plasticity constitutive modeling in geomaterials is the existence on non-normality, or non-associativity, during plastic yield. Central postulates in most plasticity theories is that an increment of plastic strain can be partitioned into elastic and plastic parts (the 't' superscript refers to total, the 'e' to elastic, and the 'p' to plastic)

$$d\varepsilon_{ij}^{t} = d\varepsilon_{ij}^{e} + d\varepsilon_{ij}^{p} \qquad (14)$$

and (Drucker's postulate) that the direction of plastic flow is normal to the yield surface such that

$$d\varepsilon_{ij}^{p} = d\lambda\, \partial f / \partial \sigma_{ij} \qquad (15)$$

where the multiplier λ is called the consistency parameter, derived from the condition that stress must remain in the yield surface during plastic flow. For geomaterials, it is often observed that the assumption of associativity or normality often overpredicts the extent of plastic volume strain (Dienes, 1975, Dewers et al., 2017, Sandler and Pucik, 1994, Brannon, 2007). This had led to the incorporation of a plastic potential function Φ such that

$$d\varepsilon_{ij}^{p} = d\lambda\, \partial \Phi / \partial \sigma_{ij} \qquad (16)$$

as this provides better predictions of the distribution between plastic shear and plastic volume strain, with plastic strain paths dictated from the normal of the plastic potential function. This can be problematic as under special conditions, as this non-association between plastic strain and yield surface can sustain unstable results where plastic waves travel faster than elastic waves, yielding negative work (Sandler and Pucik, 1994). There are a number of mechanisms that lead to 'phantom' non-associativity that cast doubt on the concept, or at the very least over-predict its occurrence (Brannon 2007), including erroneous partitioning of total strain. For example, for the porous sandstone deformation discussed by (Dewers et al., 2017), it was shown that total strain should be partitioned into at least four components relating to elastic strain, plastic strain, nonlinear elasticity, and elastic plastic coupling, and that by including the elastic-plastic coupling into the plastic strain overestimated the extent of non-associativity. Applying the normality condition to non-isomorphic yield surfaces (i.e. yield surfaces portrayed in non $\{r, z, \theta\}$ invariant spaces) and non-coaxiality of stress and plastic strain tensors due to anisotropy can be others, discussed in (Brannon 2007).

The present data set on true-triaxial deformation of Sierra White granite provides a unique opportunity to test the applicability of non-associativity, at least upon initial yielding. Up to yield, stress and strain tensors are coaxial (assuming proper alignment of the deformation apparatus allowing no rotation) which allows us to explore upon initial yielding the possibility of non-associative plastic flow. Once yielding has commenced, plastic-strain induced anisotropy associated with any kinematic hardening would negate the assumption of coaxiality, and showing the extent of non-associativity from the data set becomes more complex. From (14), we can determine the increment of plastic strain (and its invariants) just subsequent to initial yield, assuming we can determine yield accurately. If the increment of elastic strain is the same pre- and post-yielding (i.e. there is no elastic-plastic coupling or non-linear elasticity), then we can determine the increment of elastic strain post-initial yield by subtracting the pre-yield elastic strain increment from the total strain increment post yielding:

$$d\bar{\varepsilon}_{ij}^{p}\ (post\ yield)\ = d\bar{\varepsilon}_{ij}^{t}\ (post\ yield)\ -\ d\bar{\varepsilon}_{ij}^{e}\ (post\ yield) \qquad (17)$$

Given the parameterized yield surface in Figure 2.5B, the unit normal tensor to the yield surface $\boldsymbol{N}$ for each state of initial yield for each experiment are calculated from each experiment via

$$\boldsymbol{N} = \frac{\frac{\partial f}{\partial \sigma}}{\left\| \frac{\partial f}{\partial \sigma} \right\|} \qquad (18)$$

where the denominator is the norm of the numerator. Given from (16) that $d\varepsilon_{ij}^{p} = \lambda \boldsymbol{M}$ where $\boldsymbol{M}$ is a tensor in the direction of plastic flow, we can check for non-associativity by superimposing $\boldsymbol{M}$ onto points of yield for each test and compare to N (Figure 2.7A). To calculate **M**, we determine total strain before and after yielding and calculate components of the plastic strain tensor using (17), dividing by the norm to obtain the unit vector, and superposing this from each yield point.

In Figure 2.7B, we show the parameterized *Kayenta* yield criterion (4), plotted in Figure 2.5B, in $\bar{r}, \bar{z}$ space contoured for $\bar{\theta}$ in Figure 2.7B. The **N** vectors (normal to the yield surface and resolved onto the $\bar{r}, \bar{z}$ plane) are shown in blue, and the **M** vectors are shown in black for all tests at $\theta = 30^{o}$, and for selected ones at other values. It is apparent from the non-coincidence that the strain paths are non-associated with the yield surface, and that the plastic potential Φ has a lesser slope in $\bar{r}, \bar{z}$ space than the yield surface.

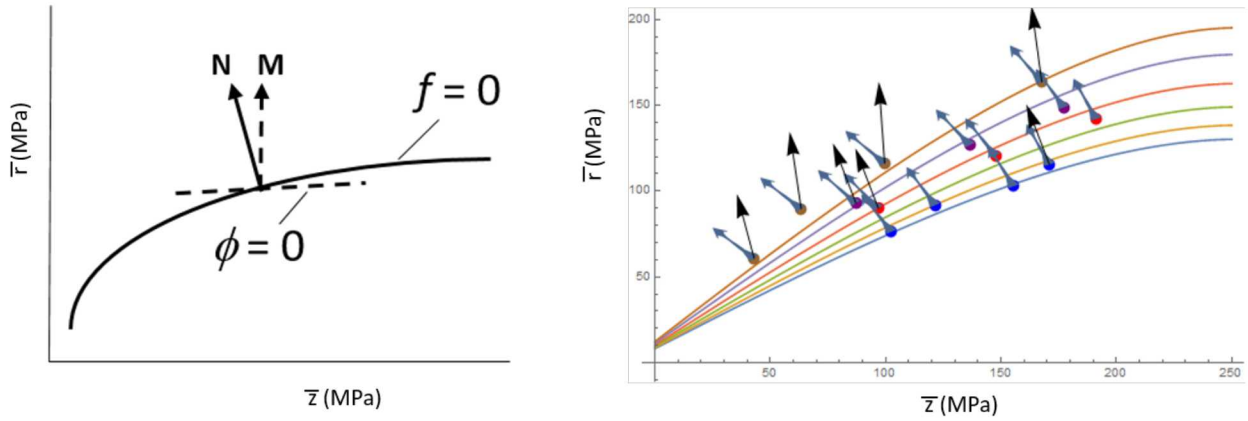

Figure 2.7. Checking for applicability of non-associativity. A. Schematic of strain vector components (M) normal to plastic potential surface and and unit normal (N) to yield surface, which coincide if the plastic potential coincides with the yield surface. B. Unit normal to yield surface compared to strain vectors for selected data, showing degree of nonassociativity may vary with Lode angle.

In the next section, we show via fitting a plastic potential surface to the strain data with *Kayenta*, that these conclusions about non-associativity appear to hold at initial yield as well as at larger plastic strains. We show in the next section that a reasonable plastic potential surface is found by applying *Kayenta*'s equation for Φ, and, as suggested by the unit normals plotted in Figure 2.7B, this takes the form of the same equation for the yield surface (4), parameterized as discussed above for the Willam-Warnke model, but using a different a_4 parameter (termed a_4^{pf} in *Kayenta*) lesser in magnitude. A surface Φ determined by the M normal vectors would appear much flatter, as depicted in Figure 2.7A. In a Mohr-Coulomb approach, this would be equivalent to selecting an angle of dilation smaller than the angle of internal friction, although we do not explore this further here.

2.5.4. Kayenta Modeling

To examine model behavior, we employ a single finite element driver to solve *Kayenta* model equations, using the Willam-Wanrke versions of yield and failure surfaces. To complete the set of parameters needed to run *Kayenta*, we need determine the isotropic bulk and shear moduli from unloading data. *Kayenta* provides options for fitting elastic data. We use a version for the bulk modulus, *K*, which carries an I_1 dependence, discussed in (Brannon et al., 2009):

$$K(\bar{I}_1) = B_o + B_1 e^{-B_2/\bar{I}_1} \qquad (19)$$

This form basically switches from a low mean stress modulus, reflecting the presence of open microcracks, to a high mean stress modulus, when cracks have closed under pressure. Kayenta offers a shear modulus functional, dependent on $\sqrt{J_2}$, but we have found that model approximations to data can be determined with a constant shear modulus, *G*. This has the effect that the Poisson's ratio and Young's Modulus increase with mean stress. We increase the shear modulus slightly for tests at higher confining pressure, which is equivalent to a mean stress dependent shear modulus, a reasonable finding. A complete version of Kayenta parameters is

given in Table 2.4, although we increase the shear modulus slightly for different model runs to account for a mean-stress dependent *G*.

Table 2.4. Summary of parameters used for Kayenta constitutive modeling.

B_o (Pa)	15.0e9
B_1 (Pa)	79.9e9
B_2 (Pa)	6.6e7
G_0 (Pa)	17.0e9
a_1 (Pa)	27.1e6
a_4 (dim)	0.42
P_0 (Pa) (intersection of hydrostat)	-6.25e8
P_1 (Pa) (arbitrary, used to invoke sloping yield surface)	1.22e10
P_2 (Pa^-2) (arbitrary)	1.28e-18
P_3 (initial porosity)	1.0e-2
CR (dim) (parameter related to κ and P0)	1.0
Ψ	0.585
J3TYPE (chooses Willam-Warnke failure model)	2
a_4^{pf} (dim) slope of plastic potential surface in invariant space	0.38

An experiment run under hydrostatic conditions is shown in Figure 2.8A, which involves hydrostatic loading to 100 MPa with unload-reload cycles at 50, 75, and 90 MPa. One can notice some erratic measurements from strain gauges at the higher mean stresses. The unload-reload cycles are only slightly distinguishable from the loading curve. This is followed by an unloading to zero. We have calculated tangent bulk moduli from this data set by measuring tangents to the unloading data at 10 MPa intervals, and fitting (19) to this data set. This gives a parameter set $\{B_o, B_1, B_2\}$ = {15.0 GPa, 79.9 GPa, 57.7 MPa}, an excellent approximation (shown in red) to the final unloading curve (underlying the red curve in green) in Figure 2.8A.

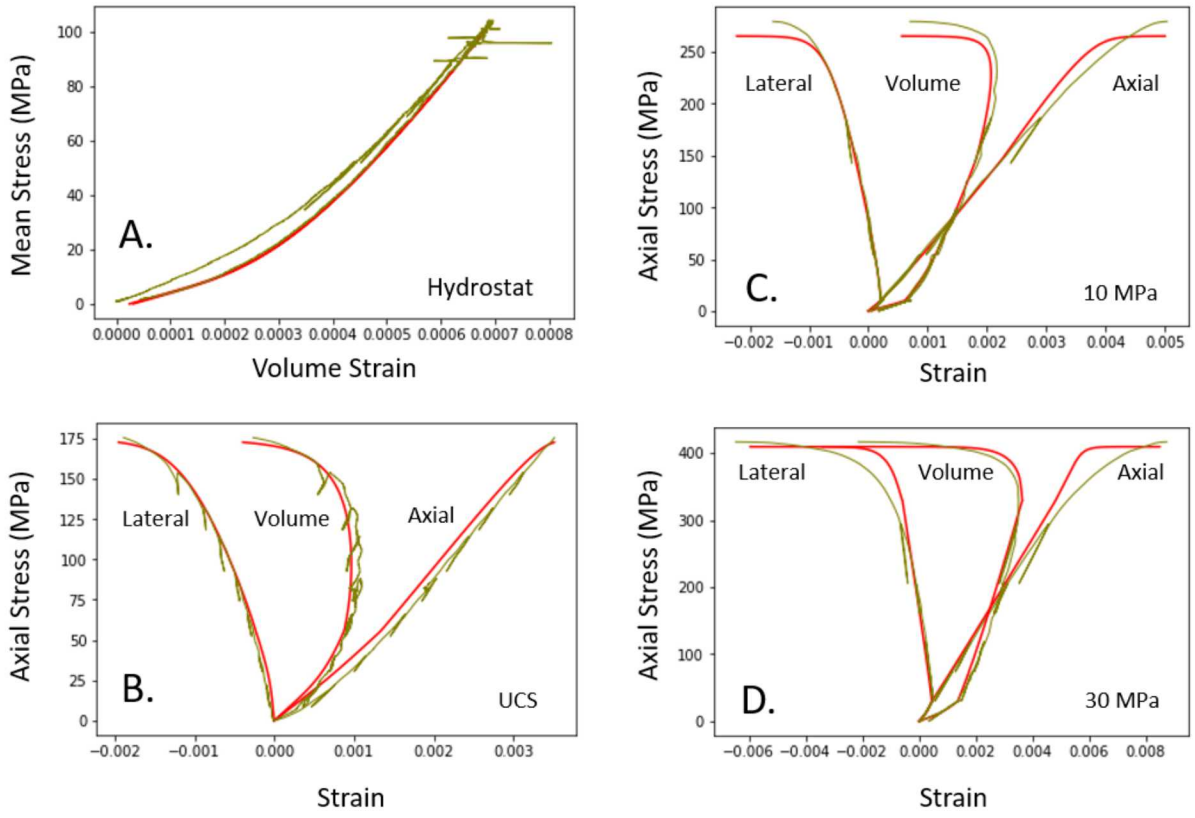

Figure 2.8. Results of Kayenta constitutive modeling for axisymmetric compression tests of Sierra White Granite. Experimental data plotted as tan curves and Kayenta output plotted as red curves. A. Fit to hydrostat. B. Behavior of UCS test. C. Behavior of triaxial test at 10 MPa confining pressure. D. Behavior of triaxial test at 30 MPa.

Results of the unconfined compression test 1A are shown in green in Figure 2.8B. Here we find a shear modulus of 17.7 GPa and an a_4^{pf} parameter equal to 0.38 MPa^{-1} yields an excellent fit to the data. In particular, the approximation to the volume strain turn-around between the onset of dilatancy and ultimate failure is modeled adequately. Assuming associative flow in this simulation would overestimate the lateral total strain by ~ 10%, and consequently the volume strain by ~20%. Ignoring the yield surface N offset produces very little dilatancy post yield until very near ultimate failure. These show the importance of considering kinematic hardening as well as non-associative flow in modeling the elasto-plastic constitutive behavior of Sierra White Granite.

Using this parameter set, we show results of *Kayenta* models for the 10 MPa and 30 MPa confining pressure axisymmetric compression tests in Figures 2.8C and 2.8D. We vary the shear modulus slightly from the UCS test of Figure 2.8B, using a value of 27.6 GPa for both triaxial tests. The results show a reasonable approximation of the test data, with a slight underestimation of ultimate failure in 8C and D.

All of the results in Figure 2.8 are for a Lode angle of 30°. Results of Kayenta modeling for true triaxial tests with Lode angles of 23° (test 1TR4), 16° (test 1TR3), and 0° (test 1TR10) are shown in Figure 2.9, using the parameter set from the 30° Lode angle tests. In general, Kayenta does a reasonable job matching the loading portions of the test data but underestimates the extent of dilatancy in all tests. This suggests that using constitutive parameters derived from axisymmetric tests may not be appropriate to extend to stress conditions where the intermediate principal stress is substantially different from the least principal stress. *Kayenta* offers additional means to parameterize the plastic potential, including a Ψ^{pf} and κ^{pf} (used in place of their yield surface counterparts Ψ and κ) that could be used to modify the shape of the plastic potential function further, but this is beyond the scope of the present study.

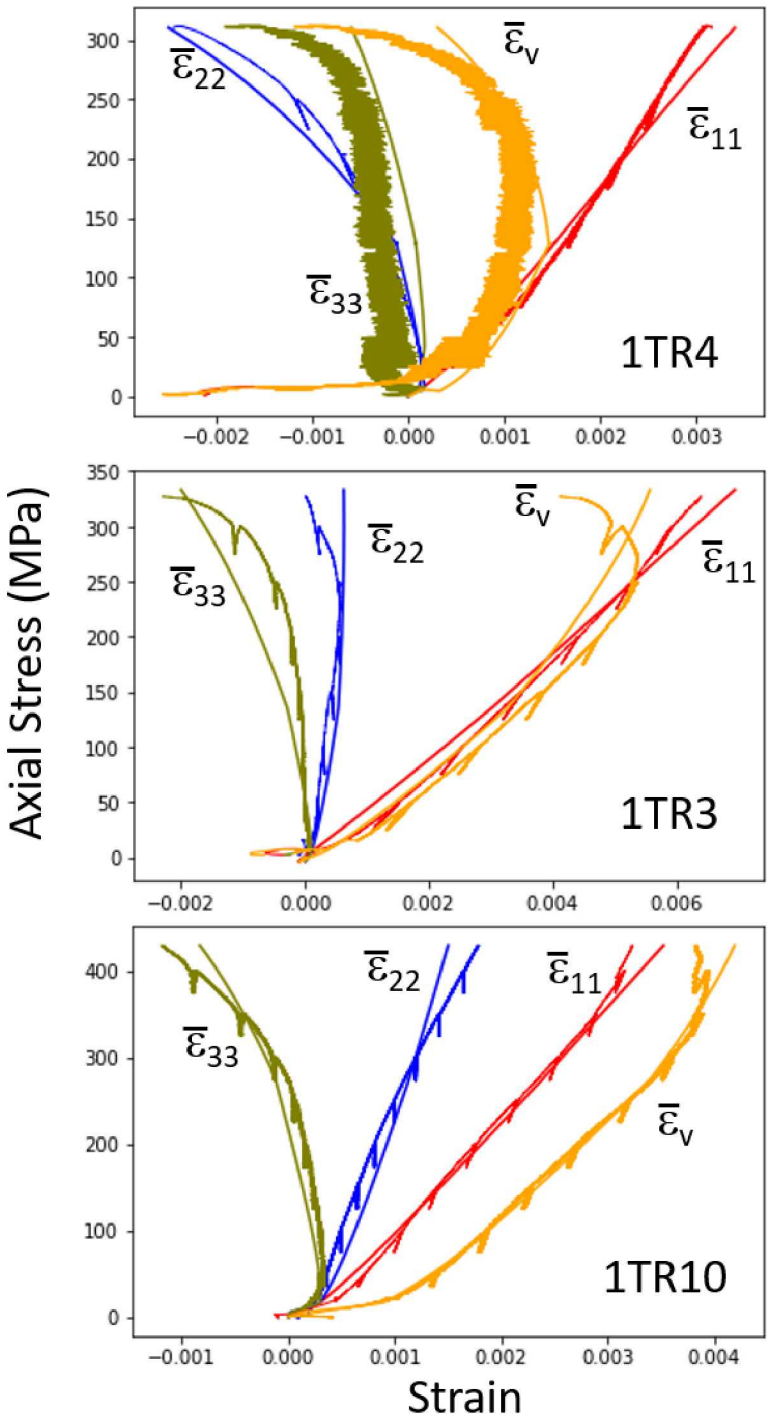

Figure 2.9. Behavior of true triaxial tests and Kayenta modeling. 1TR4: Lode Angle = 23 degrees. 1TR3: Lode angle equals 16 degrees. 1TR10: Lode angle equals 0 degrees. In general the constitutive model parameterized from ACS tests slightly underestimate the degree of dilatancy prior to failure.

2.6. Conclusions

This research presents a series of 15 tests performed on Sierra White granite with 10 tests under true triaxial conditions and four under axisymmetric (ASC) loading, to investigate the effect of the intermediate principal stress on failure of the rock. Two ASC tests were performed under uniaxial conditions to determine typical rock properties such as unconfined compressive strength, Young's modulus and Poisson's ratio. An initial test was conducted under hydrostatic loading to determine the bulk modulus. The true triaxial tests were performed under constant Lode angle conditions. All of the specimens tested failed in a brittle manner and demonstrated dilatancy prior to failure, occurring via a through-going shear fracture.

The maximum principal stress at failure was observed to rise with increasing intermediate principal stress up to a point after which it began to decrease. This point lies between the Lode angles of 16.1° and 0°. Further testing is required to determine more accurately where that point lies. It was also found that the Mises equivalent shear stress required to fail the granite decreases with decreasing Lode angle, i.e. with increasing the intermediate principal stress.

Experimental results on peak stresses at failure were used to fit several model functions, including Mohr-Coulomb, Willam-Warnke, and Matsuoka-Nakai-Lade-Duncan functions. Each provided an excellent goodness-of-fit, all with octahedral profiles more triangular than circular in shape. In particular the Mohr-Coulomb and Willam-Warnke models could be fit with the same TXE/TXC strength ratio of ~0.59, which is the ratio of rock strength under tension to that in compression.

Other important aspects of post-yield behavior of the Sierra White granite are determined by applying a generalized plasticity model Kayenta to the observed experimental behavior. We find that constitutive response of the material post-yield includes nonlinear elasticity, non-associativity, Lode-angle dependent yielding, and isotropic and kinematic hardening. These were demonstrated via a single finite element driver solution of the elasto-plastic constitutive equations. Parameterizing the observed dilatancy in particular with the 30^{o} Lode angle data underestimated the degree of dilatancy observed at lower Lode angle values, such that further work need be committed to understanding the Lode angle dependence of post-yield behavior for this material.

With respect to the impetus for this work, the results show that to properly characterize the stability of boreholes at great depth with a high degree of certainty, a model that takes into account the effect of intermediate principal stress is necessary for better predictive capacity.

3. EXPERIMENTAL STUDY OF BOREHOLE BREAKOUT IN SIERRA WHITE GRANITE

3.1. Section Summary

Understanding the state of stress in the earth is most commonly achieved by measuring the size and orientation of borehole breakouts in conjunction with hydraulic fracturing the rock mass. To better understand this phenomenon at a fundamental level a series of tests were performed on specimens cut from a nearly isotropic block of Sierra White granite (SWG). These samples were testing in a novel testing configuration designed to allow for testing of borehole breakout in a standard triaxial cell. Specimens were deformed in the presence of different borehole chemistry, as well as with different loading paths to failure. It was observed that the specimens failed in a very consistent manner showing nearly identical borehole breakouts regardless of test conditions or borehole chemisty.

3.2. Background

A novel experimental geometry is combined with acoustic emission monitoring capability to measure crack growth and damage accumulation during laboratory simulations of borehole breakout. Three different experiments are conducted in this study using Sierra White Granite. In the first experiment, the sample is deformed at a constant 17.2 MPa confining pressure without pore fluids; in the second experiment, the sample is held at a constant effective pressure of 17.2 MPa with a constant pore pressure; and in the third experiment, pore pressure is modified to induce failure at otherwise constant stress. The results demonstrate that effective pressure and stress path have controlling influence on breakout initiation and damage accumulation in laboratory simulations of wellbore behavior. Excellent agreement between the dry test and constant pore pressure test verify the application of the effective pressure law to borehole deformation. Located AE events coincide with post-test observations of damage and fracture locations. Comparison of AE behavior between the experiments with pore pressure show that breakouts develop prior to peak stress, and continued loading drives damage further into the formation and generates shear fractures.

3.3. Materials and Methods

3.3.1. Sierra White Granite

A single block of Sierra White granite was used for preparation of all the specimens used in the present study. This parent block was purchased from Coldspring Inc. and was quarried in Raymond, CA. Per the supplier, uniaxial compressive strength of this rock is 164.6 MPa, and its density is 2.64 g/cc. The rock is an unweathered, nearly homogenous granodiorite, comprised of (from most to least abundant): oligoclase, quartz, orthoclase, biotite, muscovite and a few other trace minerals. The grain size ranges from 0.04 to 0.12 inches. Preliminary testing performed on the samples yielded an unconfined compressive strength (UCS) of 176.2 MPa, Young's modulus (E) of 48.5 GPa and a Poisson's Ratio (υ) of 0.22.

3.3.2. Methods

The samples used in this test series were deformed using the novel Sandia Wellbore Experimental Simulation, or SWESI, geometry. This involves coring a sample from the parent block that is 50 mm in diameter and 75 mm in length. A hole is then drilled through the center of the sample normal to the coring direction. In bedded materials the orientation of this hole with respect to bedding is critically important (see section 4), however in the SWG which is nearly isotropic, the hole orientation was not chosen to coincide with any directional artifact. The hole shown in Figure 3.1 is 11.3 mm in diameter. During testing to prevent the infiltration of confining fluid a machined steel cover which is curved to match the surface of the specimen is fitted over the hole. This cover is also equipped with high pressure fluid ports and a 1.6 mm silicon rubber gasket to ensure a good seal between the cover and the rock surface. An example of the assembled specimen with covers is shown in Figure 3.2. The specimen is coated with a UV cure polyurethane to seal the specimen to the end caps, isolate the specimen from confining fluid and affix the borehole covers to the specimen.

The specimen is placed into a conventional triaxial cell with the pore pressure port plumbed to the borehole covers, so that fluids at different pressures can be introduced into the borehole during testing. In this test series five different borehole chemistries were selected. These were acetic and citric acid, deionized water, potassium chloride brine, sodium/calcium bicarbonate and mineral oil. These were used as the borehole fluid because they are commonly found in drilling muds. The fluid was introduced after the specimen had been loaded hydrostatically.

Acoustic emissions (AE) were recorded from an array of 8 sensors placed around the sample with four surrounding each end of the borehole in a square pattern. This allowed for location of the acoustic events which were generated during testing. The events were located using a primary threshold crossing algorithm, requiring 4 hits to define an event. The system used for AE detection and location is a Mistras Micro-II Express system with an Express 8 AE board and associated software. AE was recorded during testing to monitor the damage evolution within the sample, and visualize the progression of damage. The transducers were piezoelectric pins, manufactured by Dynasen and were mounted on the sample by potting the pins into a brass fixture with Wood's metal and then mounting the brass fixture to the sample with epoxy. The AE signals were preamplified with 40dB gain, and bandpass filtered for 150-450 kHz.

Three different loading paths were implemented for this test series to investigate the effect of the pore pressure on failure. First samples were loaded to failure in displacement control with an axial strain rate of 3.3×10^{-6} sec^{-1} while being held at 17.2 MPa confining pressure with the borehole dry. Second, samples were loaded to failure at the same axial displacement rate, however the confining pressure was 20.6 MPa with a pore pressure within the borehole set to 3.2 MPa, resulting in an effective stress of 17.2 MPa. Finally, the sample was loaded to 170 MPa axial load (load level determined from failure of previous tests) while holding the confining pressure at 20.6 MPa and the pore pressure at 13.8 MPa, resulting in a 6.8 MPa effective pressure. The axial load and confining pressure were held constant while the pore pressure was decreased to 3.4 MPa, resulting in the effective pressure increasing and creating failure. The specimens were allowed to creep for 2700 seconds while under this condition before being unloaded.

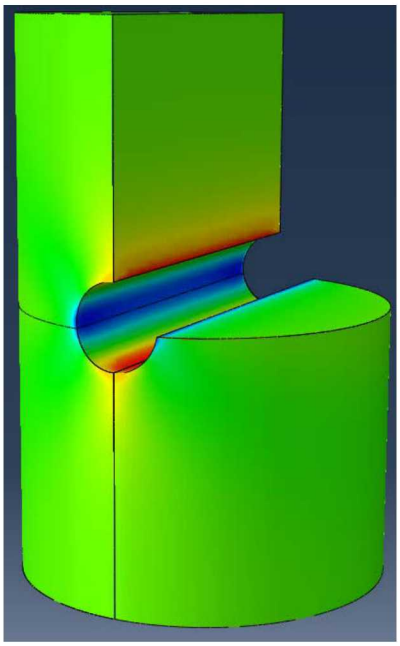

Figure 3.1: Abaqus model showing the stress concentration around the borehole when the specimen is loaded (red indicates tension and blue compression).

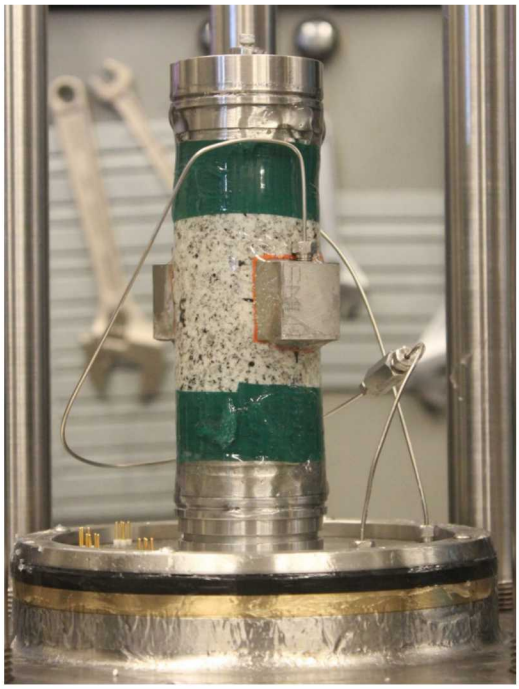

Figure 3.2: Image of granite sample with connections made for flooding the borehole space with a chemical solution. The simulated borehole is behind the metal cover with the pressure port.

3.4. Results

Stress vs strain results for the three different loading methods are shown in Figure 3.3. There is no difference in the failure strength between the dry and constant pore pressure tests, this indicates that for these conditions the effective pressure law holds for SWG. There was little to no influence of borehole chemistry on failure and response. It is also apparent from the plot of cumulative AE events (total count) shown in Figure 3.4 that there is significant yielding and

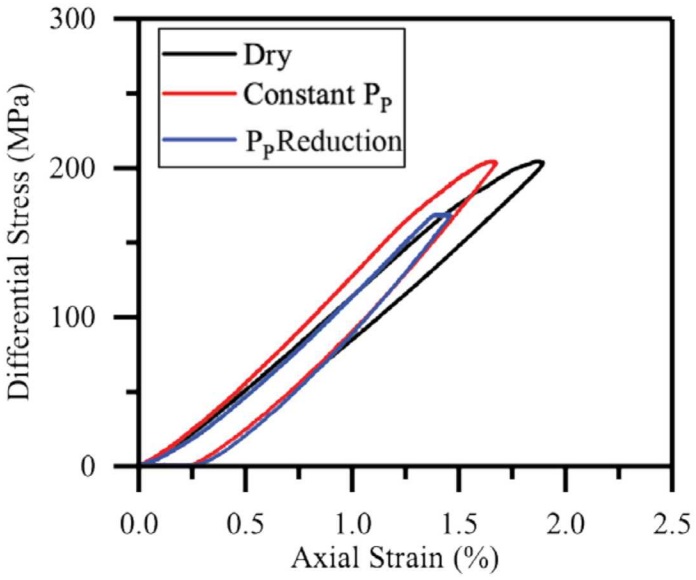

Figure 3.3: Differential stress vs axial strain for 3 representative samples deformed in 3 different ways. Note the lower peak stress in the sample where failure was induced by decreasing pore pressure.

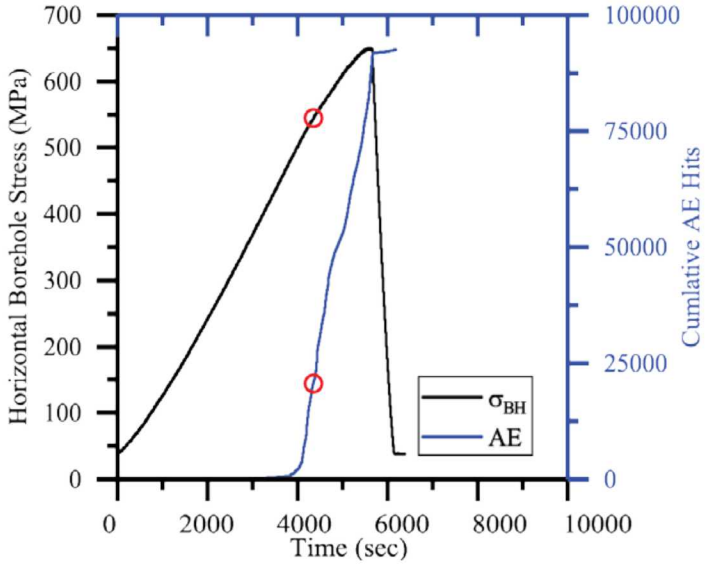

Figure 3.4: Borehole stress and cumulative AE vs Time. Note the increase in AE well before peak stress indicating yielding and damage accumulation prior to peak stress.

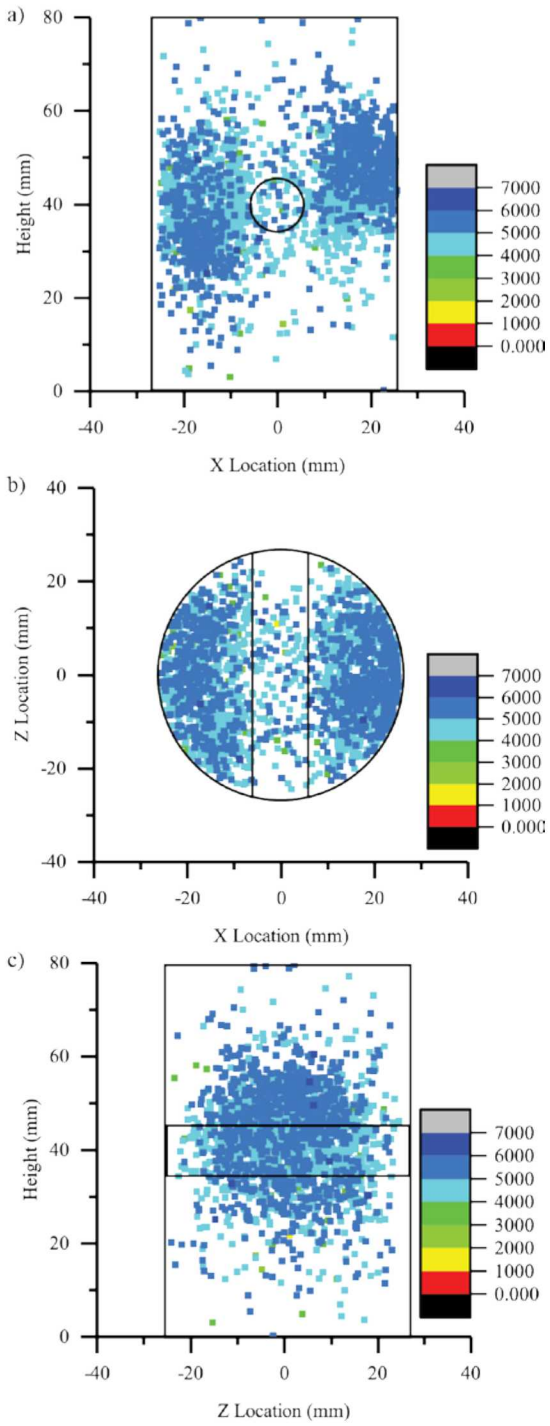

Figure 3.5: Plot of AE events located within the sample. The color indicates when the event occurred in time in terms of total events.

damage accumulation occurring prior to the peak of the stress strain curve. This is notably different from the test where the borehole pressure was decreased while under constant stress conditions. In that test there was little strain accumulated during the change in the borehole pressure, and there

was less total AE activity as compared with the other two test methods. A spike in the AE was also noticed in the decreasing borehole pressure test.

In general the AE events recorded during hydrostatic and early deviatoric loading were sporadic and randomly distributed throughout the specimen. As the test progressed the AE tended to cluster around the midpoint of the wellbore and spread towards the axial stress, i.e. towards the end of the sample as the test continued to progress (Figure 3.5), the AE events are evenly distributed along the length of the wellbore. From this information, both the AE rate and the AE location data it can be concluded that breakouts begin to form prior to peak stress. An image of a breakout is shown in Figure 3.6.

X-ray computed tomography scans were also performed on the samples. This allowed for an investigation of the fractured region around the borehole without having to destroy the sample making thin sections. Images of samples from each of the testing methods (dry, constant pore pressure, lowering pore pressure) are shown in Figure 3.7, CT scans of these specimens are shown in Figure 3.8. It is clear from observation of the CT scans that the mean and mechanism of failure is consistent across the three samples. However, the sample where the pore pressure was reduced in order to induce failure shows significantly less microfracturing away from the breakout region, which is highly evident in the other specimens. This is most easily seen on the unroll image below the specimen image. Shown here is the surface of the borehole unwrapped and viewed as a 2D planar image as one would see from a televiewer log of a borehole in the earth.

Figure 3.6: Closeup of borehole breakout in SWG generated with the SWESI geometry

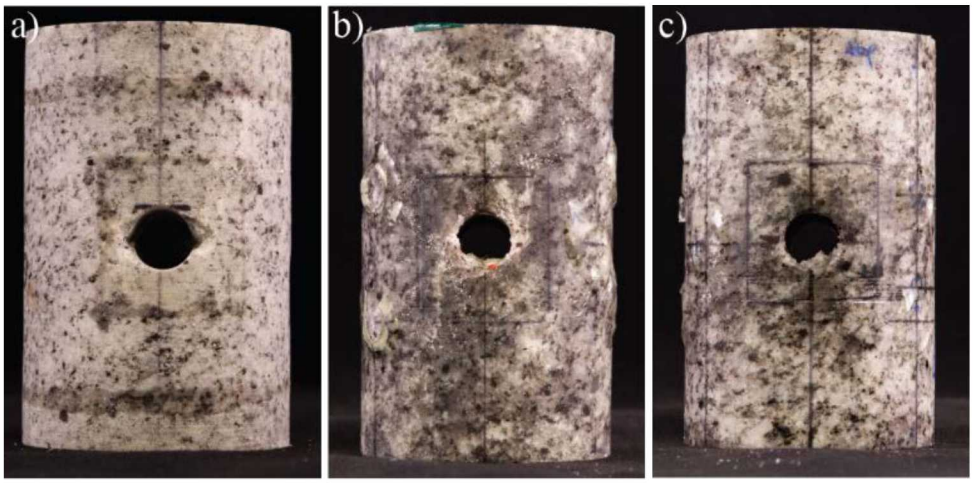

Figure 3.7: Three examples of borehole breakouts in SWG. a) Specimen tested dry, b) Specimen tested with constant pore pressure, c) specimen failed by decreasing pore pressure.

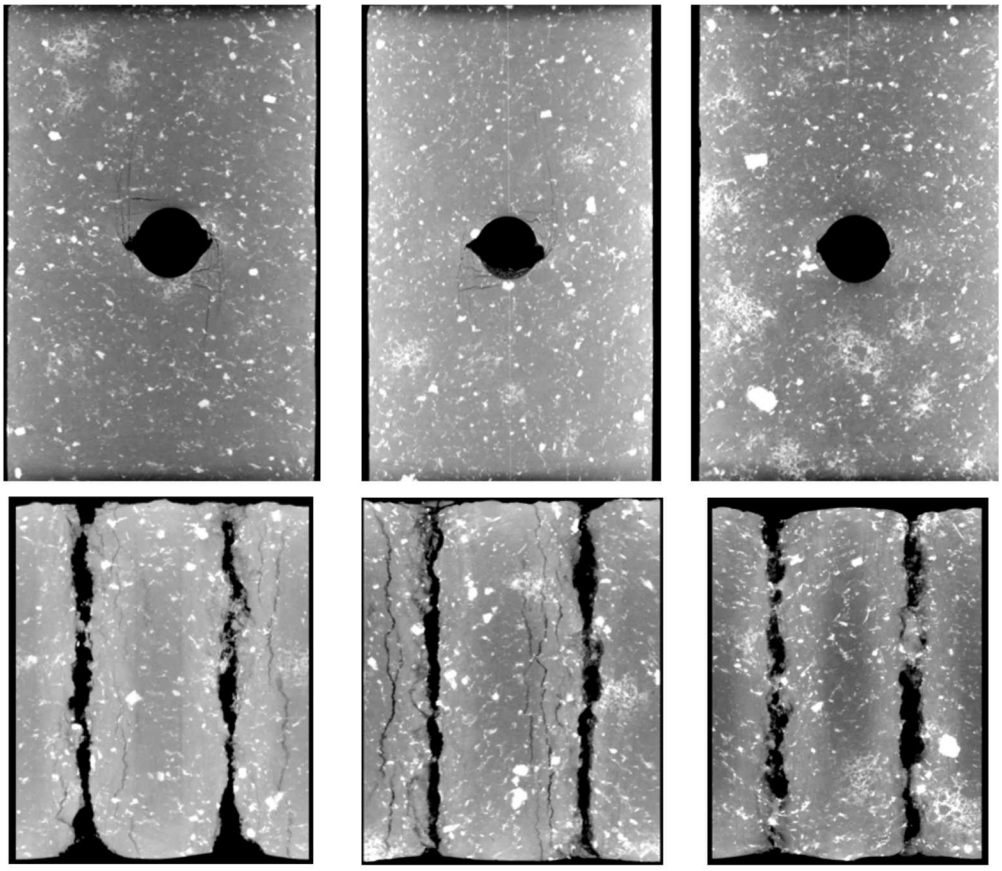

Figure 3.8: CT scan results from the specimens shown in Figure 3.7. The lower image is an unroll of the borehole surface which allows one to look at breakouts as they would appear in a televiewer log. Note breakout width is approximately the same for all of the specimens, and fractures are less developed in the sample where the pore pressure was dropped.

3.5. Conclusions

Results of this testing have shown that the SWESI geometry is effective at simulating borehole deformation phenomena using a standard triaxial cell and that borehole chemistries can be successfully introduced to the specimen. The test geometry results in borehole breakouts that are oriented to the stress state for a nearly isotropic rock, as was predicted when the test geometry was developed. Previous testing showed that there was little effect of chemistry on the response of SWG to loading conditions, this test confirmed that even in extremely high stress regions such as around the borehole the introduced chemistry had little effect. This would certainly not be true on other rock types such as shales, limestones, and some sandstones.

Fracture distribution throughout the sample is similar for both the dry and constant borehole pressure tests. The failure features and peak strength observed in both samples suggests that for this material the effective stress law is valid. However, in the specimen where the borehole pressure was decreased less fracturing was observed, and failure occurred at a lower peak stress. In all of the tests it was noticed that yield and breakout formation occur prior to peak stress, this was determined by monitoring and locating acoustic emissions within the samples.

The AE events formed in clouds which were aligned with the borehole breakout and formed along the entire length of the borehole. There was good agreement between the AE hits and locations between the constant borehole pressure test and the decreasing borehole pressure test at 85% of load (the constant stress condition applied to the decreasing borehole pressure test.

4. EXPERIMENTAL STUDIES OF ANISOTROPY ON BOREHOLE BREAKOUTS IN MANCOS SHALE

4.1. Section Summary

Measuring the size and orientation of borehole breakouts is one of the primary methods for determining the orientation and magnitudes of the in situ stresses in the subsurface. To better understand the effects of anisotropy on borehole breakouts, experiments were conducted on Mancos Shale, a finely laminated mudrock. A novel testing configuration was developed to conduct borehole breakouts experiments in a standard triaxial vessel and load frame. Samples were prepared at three different orientations and deformed under 6.9 to 20.7 MPa confining pressure. The results show a variation of peak strength and breakout geometry depending on the lamination orientation. Samples deformed parallel to laminations failed at a higher maximum compressive stress than samples deformed perpendicular to laminations, which were stronger than inclined samples. These relationships are quantified by a cosine-based failure envelope. Observed breakout shapes in perpendicular samples are V-shaped and symmetric around the borehole which advance as a series of fractures of increasing size into the side walls. In inclined samples, fractures form along weaker laminations planes and grow in an en echelon pattern towards the axial stress direction. In parallel samples, long fractures grow from the wellbore towards the axial stress direction. The observed geometries highlight sources of error in calculating in situ stresses from borehole breakouts.

4.2. Introduction

A correct understanding of state of in situ stresses in the subsurface is key for proper design of subsurface engineering projects such as oil and gas wellbores (Bradley, 1979; Gazaniol et al., 1995; Roegiers, 2002; Wilson et al., 2007; Zhang et al., 2006), tunnels (Lisjak et al., 2014; Hoek et al., 2000), mines (Arjang and Herget, 1997; Durrheim et al., 1988), geologic nuclear waste repositories (Bauer et al., 1985; Lee and Haimson, 1999; Martin and Lanyon, 2003; Warpinski and Teufel, 1991), and geologic carbon sequestration projects (Newell et al., 2017; Rutqvist et al., 2007; Streit and Hillis, 2004). In situ stress are also critical for hydraulic stimulation designs in unconventional reservoirs and predictions of potential reactivation of natural faults due to anthropogenic pore pressure variations (Ellsworth, 2013; Healy et al., 1968; Keranen et al., 2014; Marschall et al., 2006; Shamir and Zoback, 1992; Zoback, 2010). Removal of materials in constructing subsurface openings perturbs in situ stress states and creates localized stress concentrations that can result in fractures, deformation, and possible failure if not properly accounted for or mitigated (Cheatham, 1993; Haimson and Herrick, 1986; Marschall et al., 2006; Zoback et al., 1985). First observed in oil wells due to advances in dipmeter tools, borehole breakouts are compressive fractures commonly observed along the length of a wellbores created by the induced stress concentrations that can be used to determine the orientation of the in situ stresses (Bell and Gough, 1979; Gough and Bell, 1981, 1982). The size of breakouts can be used to calculate stress magnitudes if the failure progression is understood (Vernik and Zoback, 1992; Zoback et al., 1985). We present a novel experimental technique to measure effects of anisotropy on wellbore deformation and failure on a finely laminated, transversely anisotropic Mancos Shale.

Stresses in the subsurface vary spatially with depth, from region to region, field to field, even layer to layer in adjacent stratigraphic units. Vertical stress in the subsurface represents the weight of the overburden, increasing with depth (Zoback et al., 1985). Horizontal stresses at depth arise as the plane strain response to vertical loading, and are further modified by tectonic loading, topographic loading, erosional unloading, thermal loading, mechanical heterogeneity, and the constitutive behavior of rock (JASON, 2014). Because of these modifications, it is impractical to calculate in situ horizontal stresses, and therefore minimum and maximum horizontal stresses must be measured at different depths at interested locations.

Vertical stress, σ_v, can be easily calculated in wellbores by integrating density logs to calculate the weight of the overburden. Horizontal stresses at depth are usually measured by a combination of hydraulic fracturing complemented by borehole breakouts (Haimson, 1989; Zoback, 2010; Zoback and Haimson, 1983). The minimum horizontal stress, σ_h, can be reliably measured from the results of a leak off or hydraulic fracturing ("mini frac") test, where a section of a wellbore is isolated and fluid pressure is increased to induce vertical hydraulic fractures aligned with the maximum horizontal stress, σ_H. Repeated pressure cycles in hydraulic fracturing tests are also able to estimate σ_H, but complications in deep wellbores can lead to high uncertainties (Zoback, 2010). For deep wellbores used in the petroleum and geothermal industries, drilling induced fractures along the length of the wellbore can be used to constrain σ_H with increased certainty (Zoback, 2010). The widths of borehole breakouts are measured using imaging tools, and this is combined with assumptions about rock properties and failure behavior to calculate the stress necessary to create the observed width (Barton et al., 1999; Zoback, 2010). This calculation is based on predicting rock failure using Mohr-Coulomb or other failure criteria, typically ignoring thermal, chemical, rate, intermediate principal stress, and anisotropy effects. Advanced analysis can incorporate anisotropy and 3D stress effects, but calculating σ_H can still be difficult (Ewy, 2002; Moos et al., 1998; Vernik & Zoback, 1990). Simplified assumptions about rock failure do not reflect complicated geologic environments where the errors in stress orientation and magnitude estimates can be as high as 30-40% (JASON, 2014).

To investigate borehole breakouts experimentally, previous studies have utilized two approaches: true triaxial ("polyaxial") experiments or conventional triaxial axisymmetric hollow cylinders. True triaxial deformation apparatuses are capable of subjecting parallelepipeds of rocks to three independent principal stresses, recreating the stress state around a borehole and the subsequent types of borehole failure seen in the field (Haimson, 2007; Haimson and Herrick, 1986; Labuz and Biolzi, 2007; Lee and Haimson, 1993). While well suited for this type of study, true triaxial apparatuses are uncommon and tests can be costly and labor intensive. Other options for studying borehole behavior have utilized hollow cylinders of rock in conventional triaxial cells (Cuss et al., 2003; Dresen et al., 2010; Meier et al., 2015; Salisbury et al., 1991). Due to the axisymmetric geometry of the equipment and hollow cylinders, no study has been able to apply a differential stress across the borehole to recreate breakout geometry seen in the field and true triaxial experiments. In this study, a novel geometry, the Sandia Wellbore Experimental Simulation geometry, was pioneered that is capable of creating the realistic deformation seen in true triaxial experiments in a standard axisymmetric geomechanics load frame. Following the classic example of Kirsch's hole in a plate solution, a hole was drilled into the side of cylinder and covered to isolate its interior from confining pressure. When deformed in a conventional triaxial apparatus, the axial load creates a differential stress around borehole to recreate the type of breakout behavior

observed in the field. This study utilizes this novel geometry to investigate the effect of anisotropy on borehole breakouts. Experiments are conducted on three different lamination orientations of Mancos shale for a range of confining pressures in order to investigate the effect of anisotropy on induced borehole breakouts. The geometries of the resulting breakouts are characterized using thin sections, SEM micrographs, and CT scans. The results show that anisotropy has a strong effect on the compressive strength of boreholes, geometries of induced breakouts, and extent of microcracking in the sidewalls.

4.3. Methods

4.3.1.1. Source and Characterization of Mancos Shale Samples

Experiments were conducted on Mancos Shale, a Late Cretaceous mudrock deposited in the Western Interior Seaway of the USA. Samples were taken from larger blocks quarried outcrops in Utah and maintained at 0-40% humidity and temperatures between 18° and 22° C. Mancos shale consists of fine laminations alternating between silt rich and clay rich layers. Scanning electron microscope images highlight the compositional and textural difference between the light and dark laminations (Figure 4.1). Energy dispersive X-ray spectroscopy mapping demonstrated that the bulk mineralogy is similar, as the framework grains in both instances are quartz, calcite, dolomite, and minor amounts of authigenic pyrite (Figure 4.1a, b). In dark laminations, there is an abundance of illite-smectite mixed layer clays (Figure 4.1c). In light laminations, there are small amounts of plagioclase feldspar, and ankerite rims on dolomite grains (Figure 4.1f). Texturally, light laminations are composed of a tight packing of framework grains tens of microns in size. Many grains show patchy alteration textures (Figure 4.1e). In dark laminations, framework grains are embedded in a fine clay matrix (Figure 4.1b). Porosity ranges from 3.7% to 7.9% (Kocurek, 2013).

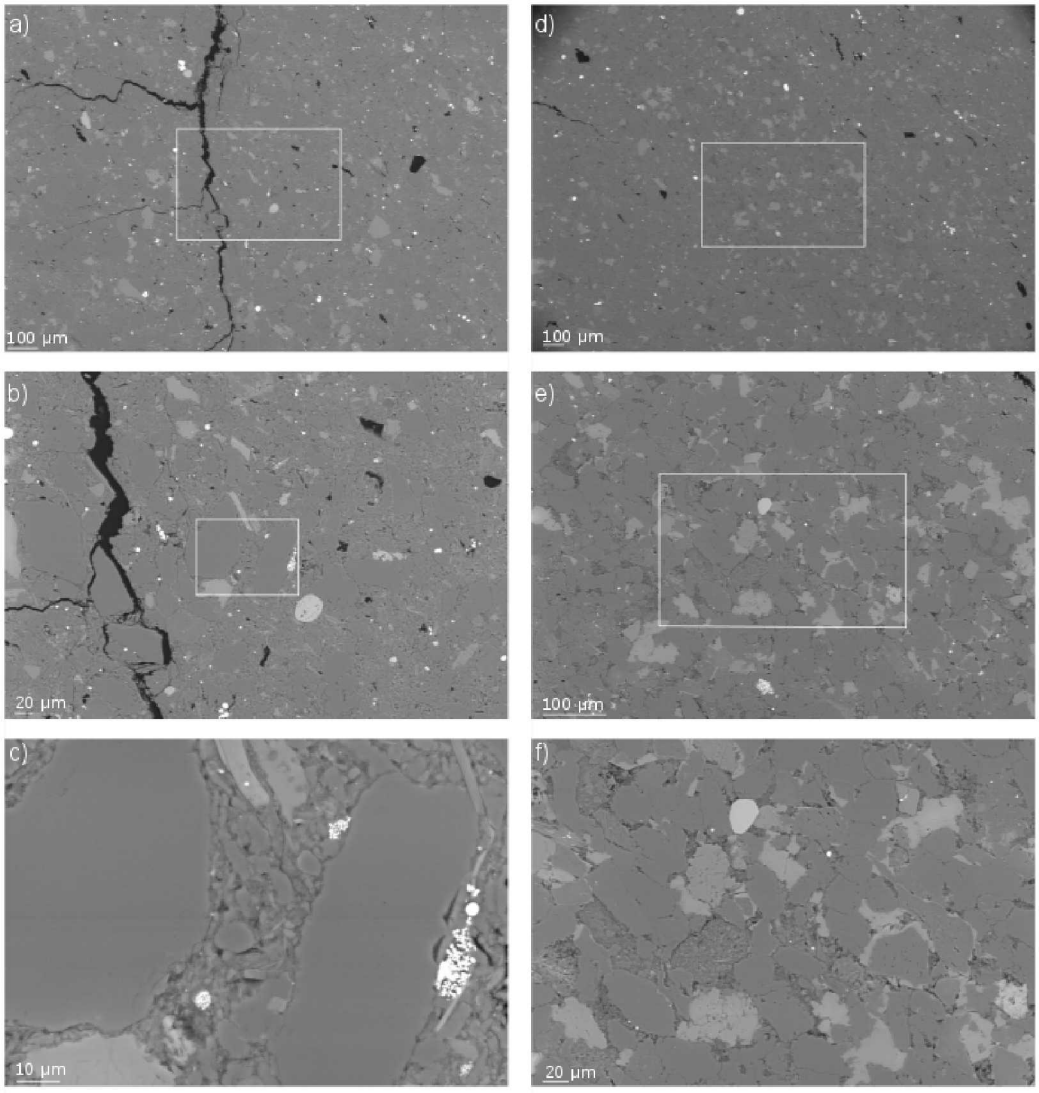

Figure 4.1. SEM images of Mancos Shale from sample 45D 1.2 with increasing magnification for (a-c) dark laminations and (d-f) light laminations. Differences are largely due to quartz and clay content.

4.3.1.2. Mechanical Anisotropy

The arrangement of laminations and compositional differences between light and dark laminations suggest that the strength of the material should depend on their orientation relative to applied stresses. Shales are commonly treated as transversely isotropic media (VTI) due to macroscopic laminations, clay platelet alignment, and microfracture orientation, where material properties like elastic moduli and failure strength differ parallel and perpendicular to the laminations (Dewhurst & Siggins, 2006; Melendez-Martinez & Schmitt, 2016; Ong et al., 2016). To verify this approach for Mancos Shale, compressional velocities were measured on samples cored parallel and perpendicular to laminations. Velocities were measured in 15° increments across the sample diameter using 1 MHz ultrasonic transducers. For the sample cored parallel to the laminations,

compressional velocities are highly dependent on lamination orientation (Figure 4.2a). Velocities are highest propagating along lamination planes and lowest when propagating perpendicular to laminations, resulting in a 18.6% reduction, similar to observations in Callovo-Oxfordian shale (Sarout & Guegen, 2008). For the perpendicular sample, velocities vary slightly (<5%) and there is no relationship to orientation (Figure 4.2b).

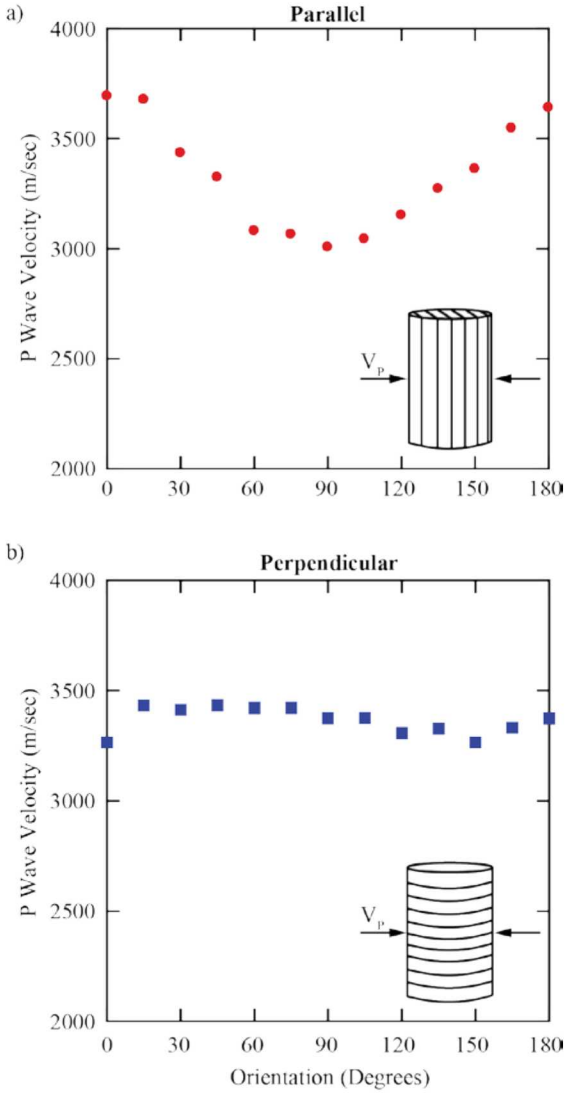

Figure 4.2: P wave velocities measured diametrically in cylindrical cores of Mancos shale. Velocities were measured in 15° increments around the circumference. a) Velocities measured for core prepared parallel to laminations. 0° is along lamination directions. b) Velocities measured for core prepared perpendicular to laminations.

Measured velocities demonstrate that the mechanical response of Mancos Shale differs across laminations but not within the plane of laminations, findings consistent with VTI behavior. The mechanical response of VTI material can be described by Hooke's law using the compliance matrix in terms of engineering moduli:

$$\begin{Bmatrix} \varepsilon_{xx} \\ \varepsilon_{yy} \\ \varepsilon_{zz} \\ \gamma_{xy} \\ \gamma_{xz} \\ \gamma_{yz} \end{Bmatrix} = \begin{bmatrix} 1/E_x & -\nu_{yx}/E_x & -\nu_{zx}/E_z & 0 & 0 & 0 \\ -\nu_{xy}/E_x & 1/E_x & -\nu_{zx}/E_z & 0 & 0 & 0 \\ -\nu_{xz}/E_x & -\nu_{xz}/E_x & 1/E_z & 0 & 0 & 0 \\ 0 & 0 & 0 & 1/G_{zx} & 0 & 0 \\ 0 & 0 & 0 & 0 & 1/G_{xz} & 0 \\ 0 & 0 & 0 & 0 & 0 & 1/G_{xy} \end{bmatrix} \begin{Bmatrix} \sigma_{xx} \\ \sigma_{yy} \\ \sigma_{zz} \\ \sigma_{xy} \\ \sigma_{xz} \\ \sigma_{yz} \end{Bmatrix}, \quad (1)$$

where ε is strain, σ is stress, γ is shear strain, ν is Poisson's ration, E is Young's modulus, and G is shear modulus (Jaeger et al., 2007; Sayers, 2013; Voight, 1928). The *ij* subscripts are annotated on the sample geometry in Figure 4.3a. For a VTI material, symmetry demands that $\nu_{yx} = \nu_{xy}$, $\nu_{xz}/\nu_{zx} = E_x/E_z$, and $G_{xz} = G_{zx}$. Elastic moduli used in this study are from an experimental study on Mancos Shale by Yoon et al., (In Prep), which showed similar compositions and compressional velocities to the Mancos Shale used in this study. The authors found that elastic moduli, acoustic velocities, and failure strength were higher in cores taken parallel to laminations when compared to cores taken perpendicular to laminations. The material properties for Mancos Shale are $E_x = E_y = 25$ GPa, $E_z = 22$ GPa, $G_{xy} = 12$ GPa, $G_{xz} = G_{yz} = 8$ GPa $\nu_{xy} = 0.2$, and $\nu_{xz} = 0.28$ (Yoon et al., In Review).

4.3.2. Experimental Geometry

50mm diameter cores, 75mm in length were prepared in three different orientations with respect to the laminations: cored parallel to the laminations (PARA samples), cored perpendicular to the laminations (PERP samples), and cored at a 45° angle to the laminations (45D samples). The cylindrical axis of the samples coincided with the applied axial stress, so PARA samples were deformed parallel to laminations, PERP samples were deformed perpendicular to laminations, and 45D samples were deformed inclined to laminations. A novel geometry, the Sandia Wellbore Experimental Simulation geometry, SWESI, was pioneered to simulate borehole behavior in the cores. A 11.3 mm diameter hole was drilled in the side of the core, centered along the length and perpendicular to the core axis (Figure 4.3a). For PARA and 45D samples, the hole was drilled parallel to the strike of the laminations. Based on Saint-Venant's principle, the hole is sized to be less than one third of the diameter of the core, minimizing stress effects from the boundary of the core. The alignment of the hole with regards to the laminations for PERP and PARA samples represents horizontal wellbores drilled into shallowly dipping shale formations under normal and reverse faulting regimes. The 45D geometry would not be commonly encountered during drilling, but would be applicable to tunneling projects (Thury & Bossart, 1999). By aligning the hole parallel to the strike of the laminations, resulting breakout microstructures will also be aligned to the strike of the laminations. The geometry gives a clear demonstration of the effect of lamination orientation and strength anisotropy on microstructural development and macroscopic strength.

According to Kirsch's elastic solution, loading a circular hole in a semi-infinite plate creates a stress concentration in the circumferential stress, σ_Θ, equal to three times the loading stress at the boundary of the hole in the plane perpendicular to the loading direction. An opposing circumferential stress equal to the magnitude of the loading stress at the boundary of the hole in

the plane parallel to the applied stress direction. For boreholes in the field, the circumferential stress from Kirsch's elastic solution, σ_B^{Kir}, at breakout locations is:

$$\sigma_B^{Kir} = \sigma_\theta = 3 * \sigma_H - \sigma_h - 2 * P_0 - \Delta P - \sigma^{\Delta T}, \quad (2)$$

where P_0 is the formation pore pressure, ΔP is the difference between formation pressure and mud weight, and $\sigma^{\Delta T}$ are thermal stresses. In our experimental geometry, σ_H corresponds to the axial stress, σ_h corresponds to the applied confining pressure, and other terms can be ignored. For boreholes in isotropic rocks at depth this solution is appropriate, but the finite size of this sample geometry and observed material anisotropy in Mancos Shale precludes this approach. To calculate the stresses at the borehole walls in our experiments, the state of stress at peak load for each experiment was modeled using Abaqus CAE with orthotropic elastic models. The model geometry was based on the sample geometry and published elastic moduli from Yoon et al., (In Prep). The model's mesh was composed of tetrahedral elements with an approximate global size of 0.0015 m, creating a total of ~200000 elements (Figure 4.3b). The orthotropic material orientation was rotated to represent the different lamination orientations. σ_{xx}, σ_{zz}, and σ_{xz} was measured at the borehole wall and converted to polar stresses following to calculate the circumferential stress at failure, σ_B^{VTI} (Timoshenko and Goodier, 1970):

$$\sigma_B^{VTI} = \sigma_\theta = \sigma_{xx} \sin^2\theta + \sigma_{zz} \cos^2\theta + 2\sigma_{xz} \sin\theta \cos\theta. \quad (3)$$

The σ_{xx}, σ_{zz}, and σ_{xz} stresses follow the global coordinate system in Abaqus and do not rotate with the different material orientations used in the PARA and 45D models. Any rotations observed in the stress state resulted from anisotropy. An additional model used isotropic material properties to investigate the effects of geometry on stress concentration, where E = 25 GPa and v = 0.28.

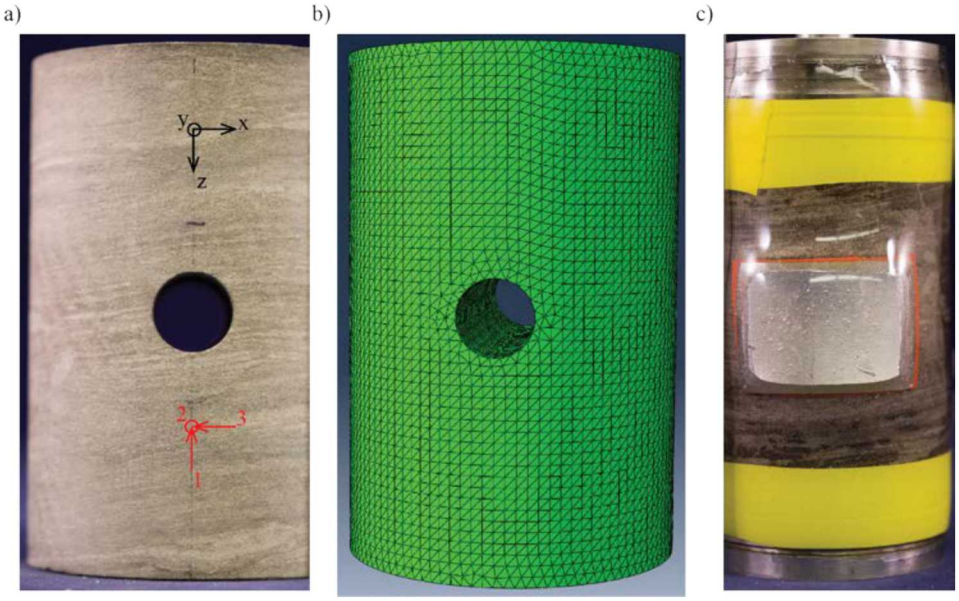

Figure 4.3: SWESI Sample Geometry. a) Mancos Shale sample with 11.3mm hole. Black axis shows σ_{ij} orientations used for modelling. Red axis shows direction of applied principal stresses. b) Abaqus finite element model of sample geometry consisting of ~200000 tetrahedral elements. c) A Mancos shale specimen with a horizontal borehole sealed by an aluminum cover and jacketed by UV cure urethane.

In order to isolate the simulated borehole from applied confining pressure, the hole was covered with a 3 mm thick by 25 mm wide by 50 mm long aluminum bar curved to fit the diameter of the core. A 1.5 mm thick silicon rubber sheet was used between aluminum cover and core to help distribute stresses and seat the cover to the core. The bar and rubber were affixed to the sample using UV cure urethane. Solid covers were used in this study, and the simulated boreholes were deformed without fluid. Covers can be machined to allow fluid access into the borehole (Choens et al., 2017). Friction between steel endcaps and the sample was minimized by using a stearic acid - petroleum jelly mixture and a 0.1mm thick copper shim (Labuz and Bridell, 1993). Samples were affixed to the endcaps using vinyl tape, and the assembly was jacketed with a layer of UV cure urethane (Figure 4.3c). Samples were deformed in a MTS® servo hydraulic load frame in the Geomechanics Laboratory at Sandia National Laboratories. Samples were loaded hydrostatically to the desired confining pressure, $P_C=\sigma_2=\sigma_3$, and then axial stress, $\sigma_A=\sigma_1$, was increased. Sample PERP 1.3 was deformed at an axial strain rate of 1.4×10^{-4} sec^{-1}; all other samples were deformed at a strain rate of 1.6×10^{-5} sec^{-1}, which allowed for controlled growth of the borehole failure. Experiments were conducted at 6.9, 13.8, and 20.7 MPa σ_3 for each lamination orientation. Samples were loaded until the axial stress plateaued, then unloaded before a stress drop could occur. This loading procedure ensured the development of fractures around the borehole, but prevented a larger through-going shear fracture. Additional experiments were conducted at 6.9 MPa σ_3 for each lamination orientation where the samples were loaded to failure to investigate the interaction between borehole breakouts and larger, through-going shear fracture. Failure strength is defined as the peak differential stress achieved during loading.

4.3.3. Imaging and Analysis of Deformed samples

After testing, specimens were photographed to document the shape and extent of borehole breakouts. Specimens deformed at 6.9 MPa σ_3 were selected for further microstructural investigation as these samples had the most intact breakouts after testing. Samples were coated with a rhodamine dyed epoxy to maintain structural integrity during processing. Whole cores were imaged using a North Star Imaging CT scanner with using a 220kV source with a voxel size of 47.8 µm. After scanning, the 6.9 MPa σ_3 samples were vacuum impregnated with rhodamine dyed epoxy and processed into thin sections. The samples were made into two different sized thin sections: samples with large shear fractures were mounted onto large thin sections (50mm x 75mm), and samples with only borehole breakouts were mounted onto standard thin sections (24mm x 46mm). For perpendicular samples, the core with a through going shear fracture was deformed at a faster strain rate, so a breakout only sample was used to make the large thin section. Thin sections were scanned on a flat-bed slide scanner at a resolution of 4800 dpi. An individual borehole breakout from each orientation was imaged in high resolution using a variable pressure environmental SEM to create a montage image. The parallel and 45 degree sample micrographs consist of 190 images stitched together, where each individual image is 250 µm by 457 µm. The PERP micrograph is 240 images.

Fracture lengths and orientations from thin sections were measured using Image J image analysis software (Schindelin et al., 2012a; Schneider et al., 2012b). Fractures were divided into three different categories based on mean gray value along the length: light, dark, and mixed. For each thin section, mean gray values were calculated for the light and dark laminations, and these were

used to assign fractures to the different laminations. Mixed fractures represent an intermediate value, indicating a fracture that cuts across alternating laminations. Fracture lengths are reported in pixels, so results are consistent between different categories for a given thin section, but not between different thin sections. Similar sized thin sections should have roughly equivalent pixel lengths. The orientations from the three different fracture categories were plotted in StereoWin9 (Cardozo and Allmendinger, 2013). All results were plotted as rose diagrams on polar grid stereonets, where the data was binned in 5º increments. The top of the stereonet is 0º, and values increase in a clockwise direction. The loading axis corresponds to the 0° axis of the stereonet. The radial length of the measurements, representing the number of measurements per bin, was normalized by the longest bin length of the lamination angle measurements, so that the diameter of the rose diagram is 1.

4.4. Results

Deformed samples failed by the development of fractures in the vicinity of the simulated wellbore, resulting in geometries matching observations of borehole breakouts (Figure 4.4) (Lee and Haimson, 1993; Marschall et al., 2006; Peška and Zoback, 1998; Shamir and Zoback, 1992; Zoback, 2010; Zoback et al., 1985). All orientations formed diametrically opposed breakouts perpendicular to the axial loading directions, but not at all σ_3 values tested. Inspection of the boreholes post-test show no confining fluid leaked into the borehole and the edges of the borehole maintained integrity, indicating that the borehole cover successfully isolated the borehole from the confining pressure. Fractures are evenly distributed along the length of the wellbore (Figure 4.5).

4.4.1.1. Mechanical Results

Clear variations in peak stress can be seen for the three different lamination orientations (Table 4.1). For all confining pressures tested, PARA samples are stronger than PERP samples, which are stronger than 45D samples, as evidenced by peak differential stress (Figure 4.6,7, Table 4.1). This peak stress represents the maximum sustained load of the structure, not stress concentration at breakout locations. At each σ_3 value, samples were loaded to yielding and unloaded, resulting in damage localized around the borehole (Figure 4.4). In an additional series of tests at 6.9 MPa σ_3, samples were loaded past yielding to develop a through-going shear fracture. The additional loading occurred at approximately the same stress as yield, so the development of a larger shear fracture does not affect the observed peak stress of the borehole structure (Figure 4.6a, b, Table 4.1).

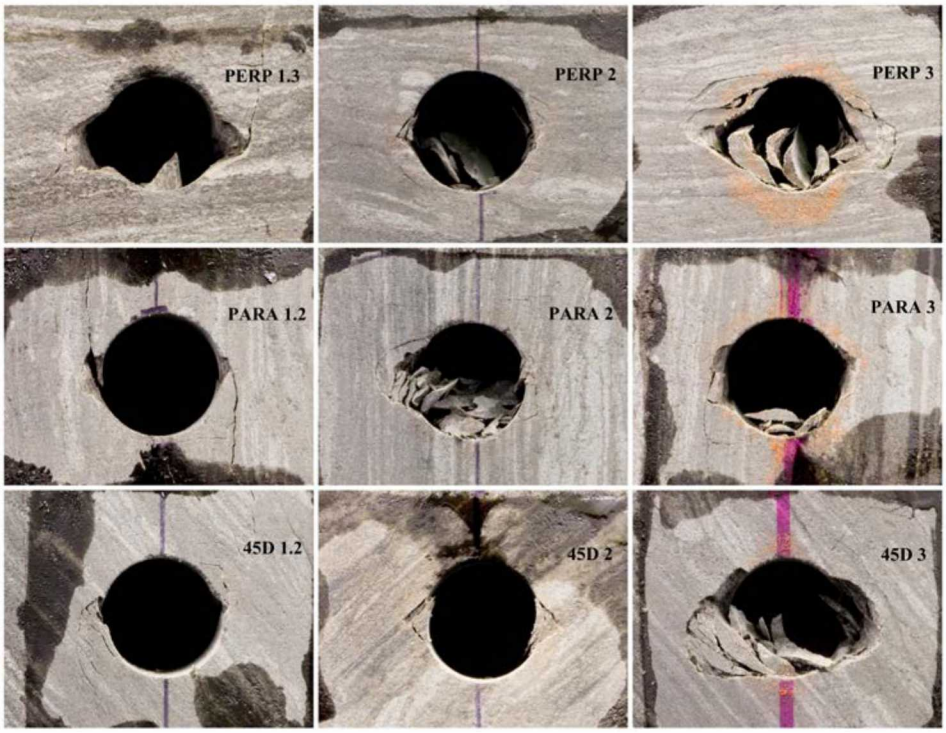

Figure 4.4 Photographs of Mancos shale showing borehole breakouts under the maximum principal stress, σ_1, applied perpendicular (PERP); parallel (PARA); and 45 degrees (45 D) to the lamination planes, respectively. The diameter of the undeformed borehole is 11.3 mm. Sample deformed at 6.9 MPa σ_3 are the left column, samples deformed at 13.8 MPa σ_3 are the middle column, and samples deformed at 20.7 MPa σ_3 are the right column.

Figure 4.5 Sample PERP 1.2 after deformation. View shows fracture distribution along wellbore. The diameter of the undeformed borehole is 11.3 mm.

All the orientations tested have a linear relationship between peak stress and mean stress (Figure 4.7a). The slope of the failure envelope for PARA samples is greater than PERP samples, which is greater than for 45D samples.

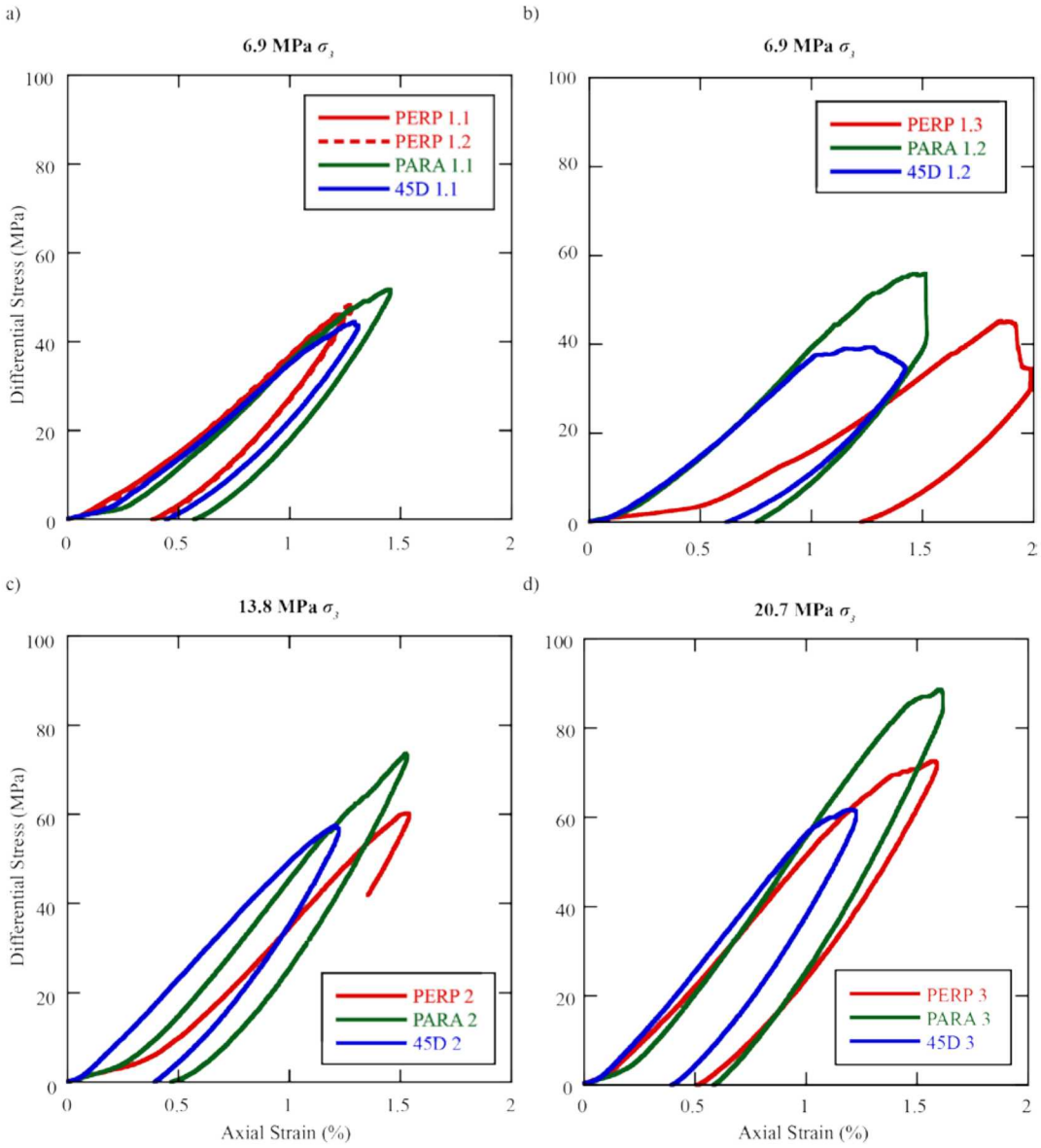

Figure 4.6: Differential stress versus axial strain for experiments conducted at a) 6.9 MPa σ_3 loaded until yielding, b) at 6.9 MPa σ_3 loaded until macroscopic failure, c) at 13.8 MPa σ_3, and d) at 20.7 MPa σ_3. Experiment PERP 2 was ended prematurely during unloading.

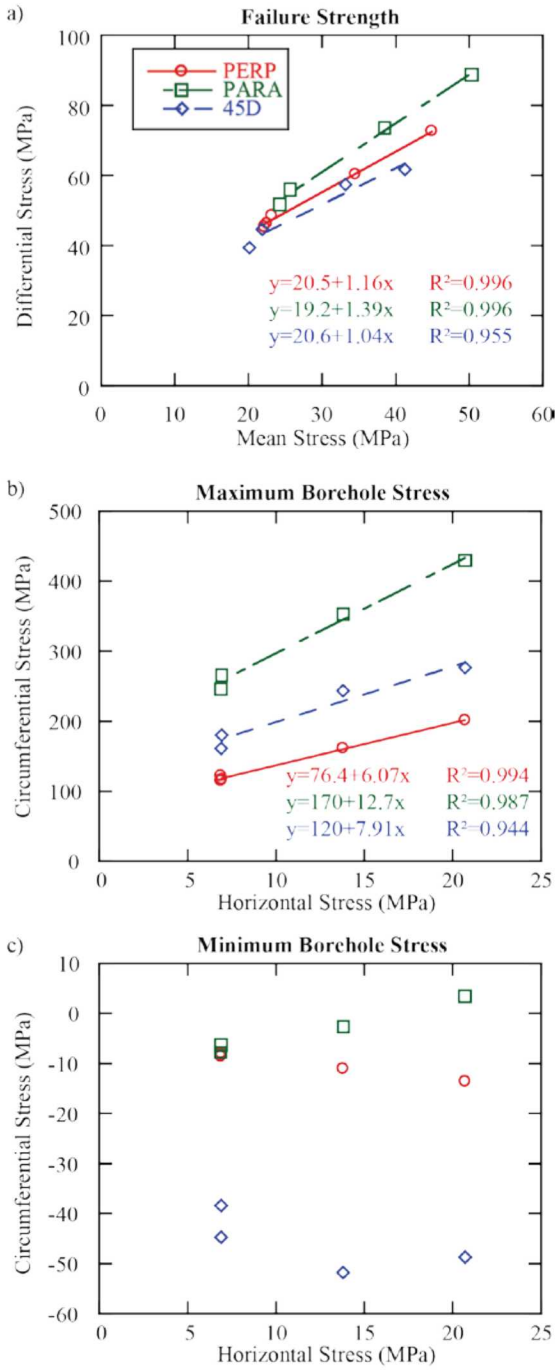

Figure 4.7: Peak stress for different sample orientations. a) Peak differential stress versus mean stress. b) Maximum calculated circumferential stress at the wellbore. c) Minimum calculated circumferential stress at the wellbore.

	σ_3 (MPa)	σ_1 (MPa)	Mean Stress (MPa)	Kirsch Stress (MPa)	VTI Maximum Stress (MPa)	VTI Minimum Stress (MPa)
Perpendicular to Laminations						
PERP 1.1	6.9	45.3	22.2	151.1	115.0	-8.0
PERP 1.2	6.9	48.6	23.2	160.1	122.5	-8.6
PERP 1.3*	6.9	46.3	22.5	153.8	117.2	-8.2
PERP 2	13.8	60.3	34.5	214.1	122.5	-8.6
PERP 3	20.7	72.6	44.9	259.4	161.3	-11.1
Parallel to Laminations						
PARA 1.1	6.9	51.7	24.3	170.0	246.3	-6.3
PARA 1.2*	6.9	55.9	25.7	182.4	265.9	-7.8
PARA 2	13.8	73.6	38.5	249.6	353.6	-2.6
PARA 3	20.7	88.8	50.3	307.7	429.6	3.4
45 Degrees to Laminations						
45D 1.1	6.9	44.6	21.9	148.7	180.3	-44.7
45D 1.2*	6.9	39.4	20.2	133.1	161.2	-38.4
45D 2	13.8	57.5	33.2	202.0	243.9	-51.8
45D 3	20.7	61.8	41.3	226.9	276.2	-48.7

* Samples deformed to failure

Table 4.1: List of samples and failure strengths.

4.4.1.2. Modeling results

Elastic modeling in Abaqus CAE demonstrates that the Kirsch solution for a hole in a semi-infinite plate does not adequately describe the state of stress at the simulated borehole in this study. An elastic model using isotropic material properties demonstrates that the stress concentration at the horizontal springline of the borehole is greater than the Kirsch solution (Figure 4.8a). Modelled tensile stresses at the vertical springline are less than predicted, and no portion of the borehole experiences significant tensile stresses. The models used in this study do not incorporate plasticity, which would act to reduce maximum stresses (Gaede et al., 2013). The models demonstrate the distribution of stresses around the wellbore from geometry and anisotropy, but absolute values at failure are an overestimate of the stresses present at breakout locations.

The inclusion of material anisotropy into the model changes the stress concentration around the wellbore (Figure 4.8). A model was performed at peak stresses observed in each experiment; the maximum and minimum circumferential stresses are listed in Table 4.1. For PERP 1.1, material anisotropy reduced the stress concentrations at the horizontal and vertical springlines of the borehole compared to the Kirsch solution (Figure 4.8b). The compressive peak is broader than the isotropic modeling example (Figure 4.8a, b). For PARA 1.1, the stress concentration at the horizontal springline is much greater than the Kirsch solution (Figure 4.8c). A low tensile stress is distributed evenly around ±30° around the vertical springline. The solutions for PERP and PARA samples are in general agreement with analytical solutions for aeolotropic plates (Green and Taylor, 1939, 1940). For 45D 1.1, the maximum and minimum stresses no longer align with

the applied stress directions (Figure 4.8d). The compressive stress is greater than the Kirsch solution, and aligned at 80° from the axial stress direction. Tensile stress is greater than the analytical solution and aligned at 30° from the axial stress direction. 45D samples are the only orientation where the stress concentrations are rotated to the applied stress state (Figure 4.8). The distribution of stresses around the wellbore are similar for experiments performed at higher confining pressures.

All orientations have a linear relationship between σ_B^{VTI} and σ_3. σ_B^{VTI} was greater in PARA samples than 45D samples, which was greater than PERP samples. The slopes of the failure envelopes have a similar relationship (Figure 4.7b, 4.8, Table 4.1). PERP and PARA samples experience small tensile stresses at the vertical springlines; 45D samples experience significant tensile stresses 30° off the σ_A axis (Figure 4.7c). PERP samples become increasing tensile with increasing σ_3, and PARA samples become increasingly compressive. 45D samples experience -40 to -50 MPa tensile circumferential stress for different σ_3 tested.

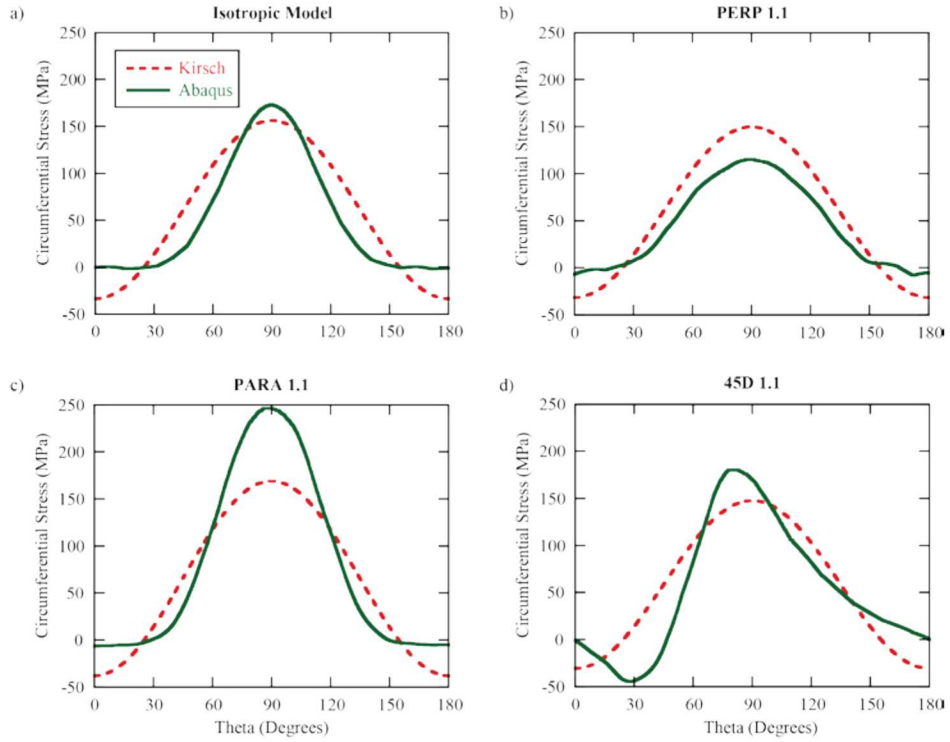

Figure 4.8: Circumferential stress calculated at inner surface of borehole using analytical Kirsch solution compared to elastic finite element models in Abaqus for a) an isotropic example, b) model based on PERP 1.1, c) model based on PARA 1.1, d) model based on 45D 1.1. 0° is towards the applied axial stress, positive is counterclockwise around the borehole. Material orientation is rotated counterclockwise around the borehole axis.

4.4.2. Fracture Geometry

Visual inspection of sample exteriors and thin sections after deformation show the borehole breakout originated in the expected region (Figure 4.4, 4.5, 4.9, 4.10). Fractures were concentrated in the borehole region, except for three samples deliberately deformed to failure (Figure 4.9, 4.11). SEM micrographs show the breakouts consist of a network of fine-scale fractures growing in series away from the wellbore (Figure 4.10). Fractures are evenly distributed along the length of the wellbore (Figure 4.5, 4.11). With increasing applied minimum stress, the breakouts increase in width and length, growing further into the formation (Figure 4.4). Closer inspection of the breakouts demonstrate that the fracture patterns vary with lamination orientation, minimum stress, and load increments.

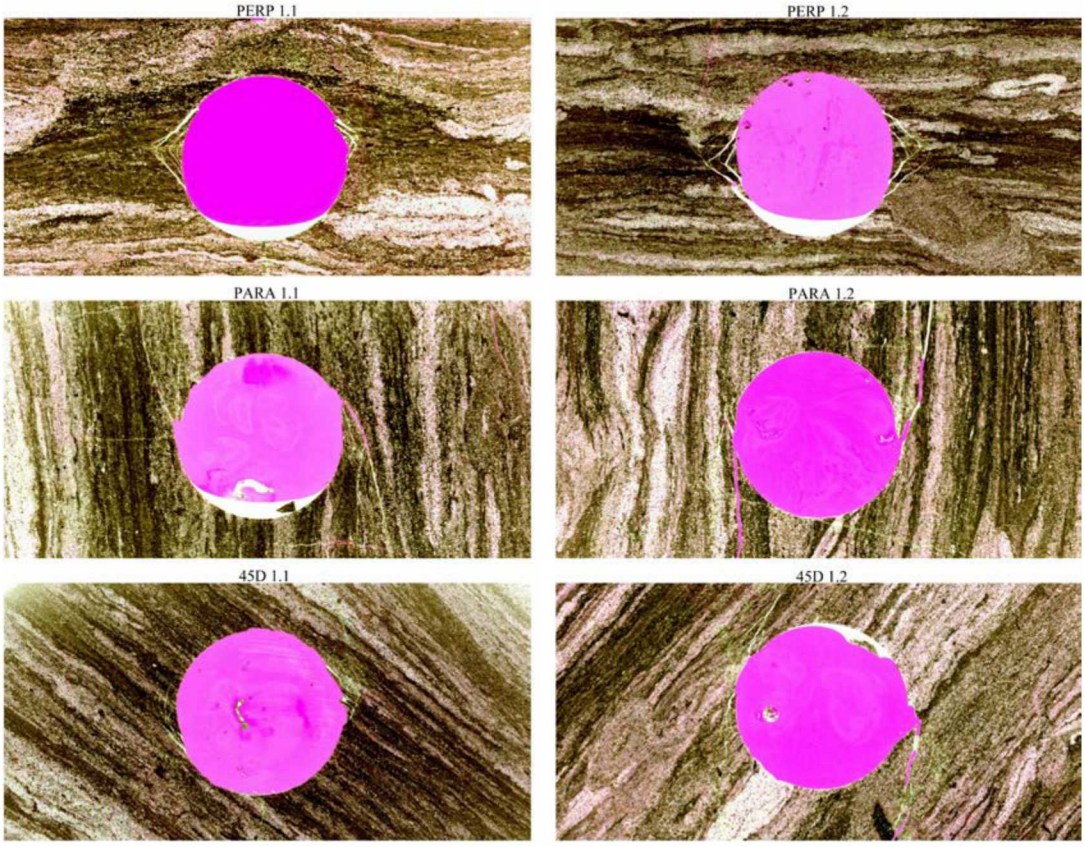

Figure 4.9: Thin section of Mancos shale showing borehole breakouts under the maximum principal stress, σ_1, applied perpendicular (PERP); parallel (PARA); and 45 degree (45 D) to the lamination planes, respectively. Experiments conducted at 6.9 σ_3. The diameter of the undeformed borehole is 11.3 mm.

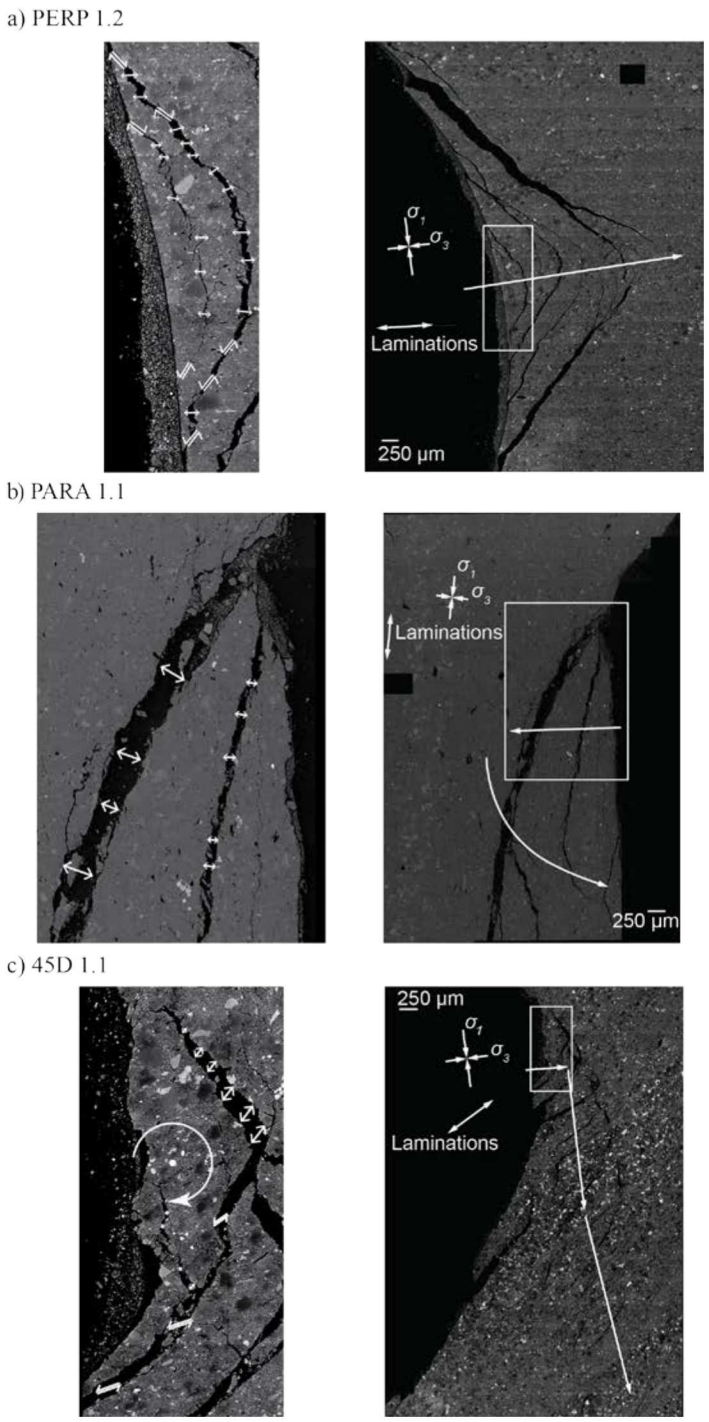

Figure 4.10: SEM micrographs of borehole breakouts. Left column are close-up views of breakout initiation point. Motion along fractures has been annotated. Right column is larger breakout view. Close up view is shown by white outline. Arrows mark direction of breakout growth

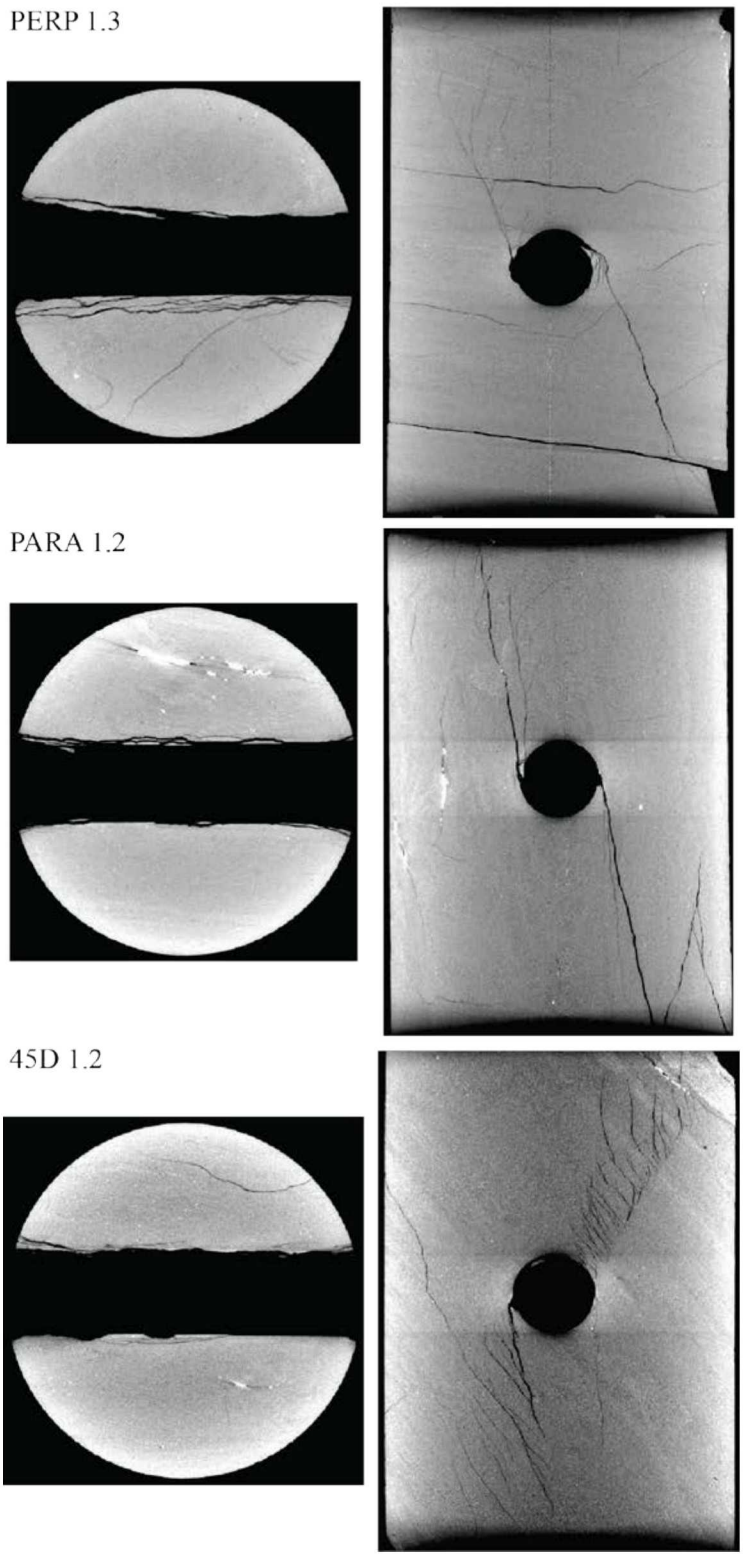

Figure 4.11: CT images of borehole breakouts in samples deformed to failure. Horizontal slice, left, and vertical slice, right, for the different lamination orientations deformed to failure at 6.9 MPa σ_3.

For PERP samples, breakouts are slightly asymmetrical around the borehole with respect to the vertical plane for all confining pressures tested (Figure 4.4). Breakouts consist of a series of fractures growing in size and progressing into the formation, maintaining a V- shape (Figure 4.5, 4.9, 4.10). Fractures next to the wellbore are small and linear; in the formation the fractures are larger and terminate in horsetail splays (Figure 4.9, 4.10). Fracture orientation is visually affected by lamination type: fractures are shallow when propagating in darker laminations and steeper when propagating in lighter laminations (Figure 4.5, 4.9). At the highest confining pressure tested, the breakout grows the furthest into the formation with rounded shape, and the width takes up a significant portion of the borehole.

In PARA samples, a typical breakout is not observed as that in PERP samples. Breakouts are small, and they do not form from the same pattern of intersecting and evolving fractures. Fractures start from the wellbore and propagate towards the maximum principle stress. Fractures are long and appear to propagate along preferred dark laminations (Figure 4.9, 4.10). Deformation can be manifest as highly asymmetric breakouts depending on the distribution of different types of laminations: the breakout is much larger on the side of the sample where there is a higher concentration of dark layers (Figure 4.4). Small deformations at the borehole wall result in a small, sharp breakout; continued deformation results in a larger, rounded breakout.

The 45D sample breakout geometries are highly dependent on confining pressure. At the lowest σ_3 value tested, the resulting breakouts are highly asymmetric and misoriented to the applied axial stress (Figure 4.4, 4.9). Breakout location is controlled by the distribution of laminations along the borehole radius (Figure 4.9). Fractures grow parallel and within laminations in an en echelon pattern and curve towards the axial stress, forming a breakout. When breakouts form, fractures first grow along laminations, and then cut perpendicular across the laminations to complete breakouts. A series of en echelon fractures grows upwards from the breakout (Figure 4.9, 4.10). With increasing confining pressure, the resulting breakout geometries become symmetric with respect to the vertical plane. In sample 45D 2, fractures propagate parallel and perpendicular to laminations to form sharp, V-shaped geometries. On both sides of the wellbore, the breakouts appear to be controlled by dark laminations (Figure 4.4). In 45D 3, the breakouts are the largest observed in this study with a rounded, broad tip geometry, and the width is nearly equal to the diameter of the borehole (Figure 4.4).

The interaction between the borehole breakouts and the development of a through-going shear fracture differs for different lamination orientations. In PERP 1.3, shear fractures grow away from the tips of breakouts towards the corners of the samples. Fracture grow at a steeply dipping angle, with subvertical splays near the ends of the samples (Figure 4.11). The breakout geometry is similar to the sample without a through going fracture, suggesting that fractures formed after the development of the breakouts in response to continued loading (Figure 4.9, 4.11). In PARA and 45D samples, the resulting failure geometry is an extension of the geometries seen in the samples that were only loaded to yielding. In PARA 1.2, failure is accomplished by extending the subvertical fracture from the wellbore to the ends of the sample, with increasing aperture on the fractures. In 45D 1.2, the resulting geometry is an extension of the en echelon fractures seen in 45D 1.1 that now increase in size to the ends of the samples (Figure 4.9, 4.11).

4.4.3. Lamination Influence on Fracture Orientation

To quantify lamination effects on fracture growth, ImageJ analysis software was used to trace fracture lengths and orientations for thin sectioned samples (Table 4.2). For all samples, the highest concentration of fractures is observed in dark laminations. More than half of the total fractures occur in dark laminations, with the remaining fractures split between light laminations and mixed fractures. With the exceptions of PARA 1.1 and 45D 1.1, the fractures in dark laminations are longest. Total number of fracture increases with continued loading, as demonstrated by samples loaded to failure. The increase in fracture count in PARA 1.2 is slight as the through going shear fracture consists of larger, more continuous fractures that split the sample vertically (Table 4.2). Although it is a relative comparison, the fractures in PARA samples are noticeably longer than the other lamination orientations.

	Lamination Angle	Light				Dark				Mixed				Total		
		Number	Average Length	Total Length	Angle	Number	Average Length	Total Length	Angle	Number	Average Length	Total Length	Angle	Number	Average Length	Total Length
Perpendicular to Laminations																
PERP 1.1	96	10	55.2	552.0	13	92	96.2	8845.8	30	28	72.91	2041.5	19	130	88.0	11439.3
PERP 1.2	90	30	85.6	2568.9	2	164	67.8	11125.8	157	35	59.46	2081.1	162	229	68.9	15775.8
Parallel to Laminations																
PARA 1.1	4	29	136.9	3971.0	2	45	158.5	7133.4	5	22	183.24	4031. 3	11	96	157.7	15135.7
PARA 1.2	176	20	177.4	3547.2	5	66	204.2	13475.2	176	15	172.27	2584.1	171	101	194.1	19606.5
45 Degrees to Laminations																
45D 1.1	141	14	98.0	1371.3	121	94	74.6	7012.4	123	3	53.40	160.2	101	111	77.0	8543.9
45D 1.2	139	74	126.4	9352.1	179	249	174.8	43532.7	150	80	146.05	11684.0	162	403	160.2	64568.8

Table 4.2: Fracture characteristics as measured from thin sections.

The average fracture orientations in light laminations, dark laminations, and mixed fracture for six thin sections are plotted as rose diagrams in equal angle, polar grid stereonets (Figure 4.12). For PERP samples, clear differences in fracture orientation can be seen between the different

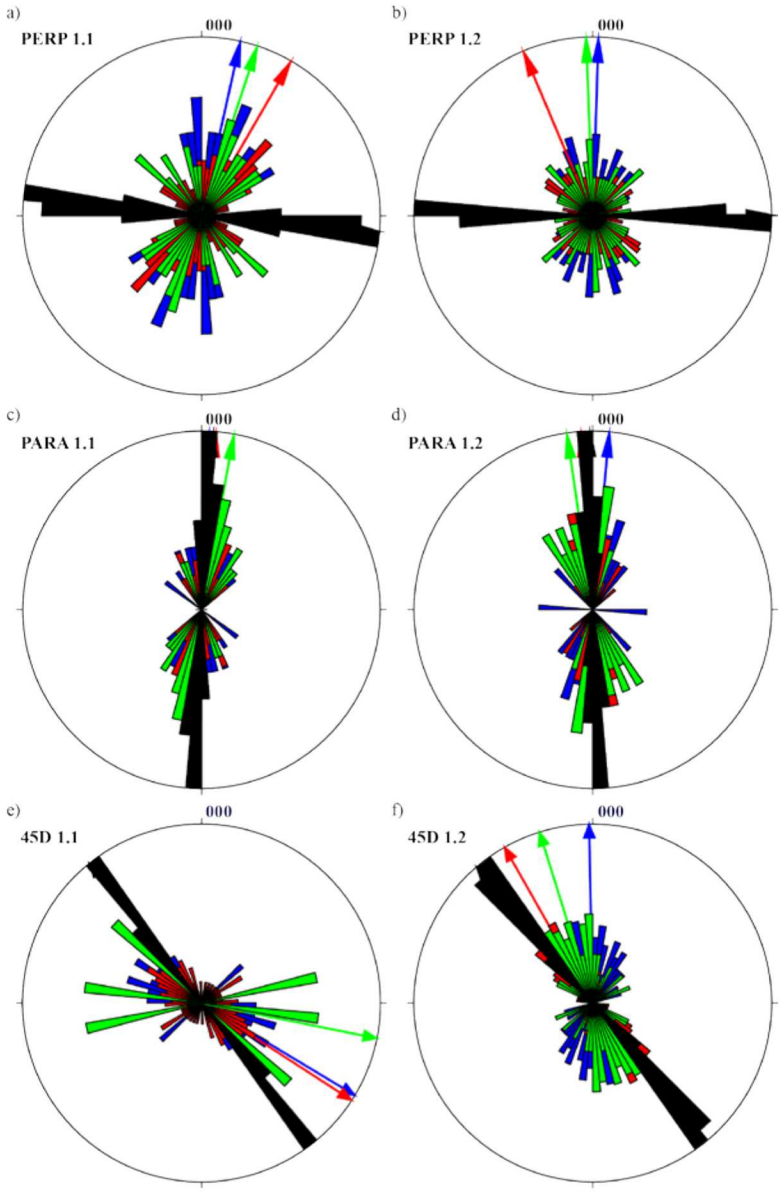

Figure 4.12: Rose diagrams of fracture orientations plotted in equal angle, polar stereonets. Stereonets are normalized to laminations measurements. Lamination measurements are in black, fractures in light laminations are in blue, fractures in dark laminations are in red, and mixed fractures are green. Arrows indicated average orientation for a category. 0 degree, vertical, is at the top of the stereonet. a) PERP 1.1. b) PERP 1.2. c) PARA 1.1. d) PARA 1.2. e) 45D 1.1. f) 45D 1.2.

lamination types (Figure 4.12a, b). Fractures in light laminations have a broad range of orientations, resulting in a near vertical average orientation for splitting fractures parallel to the axial stress. For fractures with mixed growth between the two laminations, fractures are sporadic with an average orientation slightly shallower than light laminations. Fractures in dark laminations have a much clearer clustering with an average orientation of 30º off of the vertical axis.

The fractures in PARA samples are subvertical splitting fractures parallel to the axial stress and close to the lamination orientation (Figure 4.12c, d). Fractures are strongly oriented towards vertical in PARA 1.1, with average orientations for the light, dark, and mixed categories at 2º, 5º, and 11º respectively. There is a noticeable absence of fractures with dips between 45º and 135º. The total number of fractures, fracture length, and average orientation are similar for PARA 1.1 and 1.2, suggesting that the continued loading in PARA 1.2 does not induce extra damage, but rather increases aperture on pre-existing fractures (Figure 4.12c, d; Table 4.2).

The majority of observed fractures in 45D samples are concentrated between 90º and 145º, and do not dip steeper than the laminations (Figure 4.12e, f). Fractures in light and dark laminations have similar dips that are within 20º of lamination (Table 4.2). Fractures in mixed laminations have a shallower, near horizontal dip. With increased loading, 45D 1.2 displays a slightly different distribution of fracture orientations (Figure 4.12f). Fractures in dark laminations are subparallel to the lamination dip, but fractures in light and mixed laminations are much steeper. Fracture in light laminations have a vertical average orientation. Fractures orientations are concentrated between the dip of laminations and vertical, there is a lack of fractures with shallow and horizontal dips.

4.5. Discussion

4.5.1. Micromechanics of Borehole Breakout

The microstructures observed in this study demonstrate clear differences in the interaction between fracture growth and lamination angle for the different lamination orientations. Due to observed mineralogical differences, it is expected that light laminations will be stronger than dark laminations, and micromechanical testing from previous studies illustrates clear differences in strength between clastic and clay rich layers in shales (Bennett et al., 2015; Bobko and Ulm, 2008; Ulm et al., 2007). For all lamination orientations, fractures preferentially form in dark laminations. The highest number of fractures were recorded in dark laminations, and fractures in dark laminations are, in general, longer than other fractures and shallower in dip (Table 4.2). All cores had approximately the same ratio of light and dark laminations, suggesting that lamination orientation and not sample to sample variability is responsible for observed differences in strength and geometry.

In PERP samples, the resulting breakouts are the closest to the idealized geometry, with a V-shape and only a slight asymmetry around the borehole with respect to the vertical plane. Thin sections and SEM micrographs of sample PERP 1.1 demonstrate that the breakouts consist of a series of fractures growing in size into the formation (Figure 4.9, 4.10). The fractures are inclined at the borehole, and vertical at the nose of the breakout. The inclinations of the fractures are clearly affected by the lamination type, as fracture segments steepen in presumably stronger light laminations (Figure 4.9, 4.12; Table 4.2). The inclined fractures also terminate at lamination

transitions with a series of steep horsetail splays in lighter laminations. Shear displacement is observed on inclined segments, with opening mode displacement on steeper segments. The resulting geometry is similar to mixed mode fracture meshes observed in layered stratigraphies, e.g., the Monterrey Formation in Santa Barbara, California (Gross, 1995; Sibson, 1996). At the innermost breakout at the borehole wall, the geometry is very broad with little contribution from inclined segment. The first fractures were likely vertical fractures just inside the formation from the wellbore, creating a buckling motion that completed the first breakout. The next breakout is larger in size with mostly vertical segments but increasing shear displacement on inclined segments. The stepped pattern suggest that the vertical fractures grew first, and were subsequently linked by inclined fractures. The subsequent breakouts have a different growth pattern than the innermost breakouts. The inclined fractures originate at the borehole wall, and propagate at an angle into the formation towards the horizontal centerline of the borehole. These fractures either reorient at the lighter laminations or end in splays. These vertical segments or splays from different sides of the horizontal centerline link to complete the breakout. The breakout becomes sharper as it grows into the formation, as less of the total breakout is affected by the light lamination centered on the borehole.

Fractures originating at the wellbore for PARA samples do not form idealized breakout geometries. In PARA 1.1, the breakouts form outside of the expected area, the size is limited, and the shape results from fragmentation rather than fracture bounded sections (Figure 4.9, 4.10). Fractures are steep and curve away from the borehole towards the axial stress direction. Motion on the long, steep fractures originating at the wellbore is primarily opening mode. The first fractures to form are thin, vertical cracks adjacent to the borehole wall (Figure 4.10). Because of the influence of laminations on growth directions, the fractures grow longer along the borehole as opposed to forming a breakout like PERP 1.1. The starting point of subsequent fractures is controlled by stress concentrations created by different strength laminations intersecting the borehole. Fractures grow in series into the formation. The outermost fracture grows towards the ends of the sample and outside of the vicinity of the wellbore. As the outermost fracture opens, the curved section near the borehole causes the fractured rock to flex into the borehole, creating a series of inclined fractures that delineate flakes of rock that could spall into the borehole.

In 45D samples, the breakouts at the lowest confining pressure tested are asymmetric and misaligned to the axial stress direction (Figure 4.4). In 45D 1.1, only one side of the borehole has a fracture bounded breakout; the remaining side has fractures that grow away from the wellbore with horsetail splays oriented in the axial stress direction (Figure 4.8). The breakouts do not form along the centerline of the borehole as predicted by the Kirsch solution, but instead occur at locations rotated away from the stress direction where anisotropic elastic modeling predicts a significant tensile stress. The breakouts occur at boundaries between light and dark laminations, suggesting that stress contrasts between different strength laminations also influence breakout location. Microstructures of the fracture bounded breakout demonstrate that the geometry is highly dependent on lamination direction (Figure 4.9, 4.10, 4.12). There are two main orientations of fractures in the breakout: longer fractures growing along laminations, and shorter fractures growing perpendicular to laminations. Shear motion is visible on lamination parallel fractures, and opening mode displacement is visible on lamination perpendicular fractures (Figure 4.10). The development of fractures on the side without a breakout demonstrates that the lamination parallel fractures are the first fractures to form. Fractures from at the wellbore and grow into the

formation along the laminations, terminating in a series of vertical horsetail splays (Figure 4.9). Elastic modeling indicates that a significant tensile stress is present at these locations. This suggests that the fractures originally formed as opening mode fractures and propagated in weak laminations until clear of the borehole stress concentration where fractures turned towards the axial stress. The applied load would have activated these cracks in shear, allowing lamination planes to slip into the borehole. On the side with a breakout, lamination parallel fractures initiate at the borehole wall and grow into the formation. Motion along these fractures creates the lamination perpendicular fractures, which are wing cracks that grow towards the wellbore to complete the breakout. These lamination perpendicular fractures originate at the terminations of lamination parallel fractures, and aperture decreases the intersection point (Figure 4.10). Movement along laminations and the wing cracks allow the flakes created by the breakout to rotate and slide into the borehole. Breakouts grow larger in size as a series of en echelon fractures into the formation, where the lamination perpendicular fractures are roughly aligned (Figure 4.9, 4.10).

Observed breakout width varied with applied σ_3 values and not with the extent of axial loading (Figure 4.4, 4.8, 4.10). At the lowest σ_3 value tested, breakout widths are the smallest portion of the borehole (Figure 4.4). Continued loading does not change breakout widths, as breakouts are similar for samples loaded to peak stress as samples loaded to shear fracture (Figure 4.8, 4.10). With increasing σ_3, breakouts are an increasing portion of the borehole (Figure 4.4). At 20.7 MPa σ_3, breakouts are a significant portion of the wellbore, and their width is nearly equal to the diameter of the borehole. Observed damage is greater at 20.7 MPa σ_3, and there is significant spalling of material in the borehole for PERP 3 and 45D 3 (Figure 4.4).

Calculated σ_B^{VTI} and σ_B^{Kir} values at breakout locations are well in excess of observed unconfined compressive strengths, UCS, for Mancos Shale (Yoon et al., In Prep). Incorporating anisotropy into numerical models reduces the predicted stress for PERP samples, but increases predicted stress values for PARA and 45D samples. 45D samples are also predicted to have a tensile stress several times larger than common rock tensile strengths (Figure 4.8). Both the isotropic analytical solution and the anisotropic numerical solution do not incorporate plasticity, likely overestimating the stress at breakout locations. Models incorporating damage demonstrate that the dissipative strain-softening can reduce the predicted stress at breakout locations (Gaede et al., 2013). Incorporating damage would act to reduce our predicted stresses, but it is likely that predictions would still be greater than UCS measurements. Several experimental and modeling studies have reported strengthening of smaller laboratory-scale breakouts (Bazant et al., 1993; Cuss et al., 2003; Ewy, 2002; Ewy and Cook, 1990a; Song and Haimson,1997; van den Hoek, 2001). These studies determined that grain size related to microstructural breakout mechanism controlled this relationship (Cuss et al., 2003; Herrick and Haimson, 1994); Mancos Shale samples would also be affected by lamination size relative to the borehole.

4.5.2. Borehole Geometry Compared to Other Rock Types

These breakout geometries observed in this study are consistent with previous experimental work investigating borehole breakouts. True triaxial deformation of borehole breakouts in Lac du Bonnet granite and Westerly granite result in sharp, V-shaped breakouts oriented perpendicular to the maximum principal stress (Haimson, 2007; Haimson and Herrick, 1986; Lee and Haimson, 1993; Song and Haimson, 1997). Microstructural investigations show that the fractures grow by a series of extensile microcracks highly concentrated around the borehole that form subparallel to

the axial stress (Haimson, 2007; Lee and Haimson, 1993; Song and Haimson, 1997). Porous rocks also demonstrate similar behavior. These microfractures either link together to fail in shear around the wellbore (Ewy and Cook, 1990b; Haimson and Song, 1993; Herrick and Haimson, 1994), or form columns that buckle and spall into the wellbore (Bazant et al., 1993; Lee and Haimson, 1993; Zheng et al., 1989). Borehole breakouts in Indiana limestone consist of sharp, V-shaped breakouts formed by a series of fractures and pervasive grain crushing and cement disaggregation in the breakout (Haimson and Herrick, 1986). In Cordova Cream limestone, the geometry of breakouts is similar, but fractures propagate along grain boundaries and do not result in split grains (Haimson and Song, 1993). Overall growth of the breakout is asymmetric and similar in shape to PERP 1.2 (Figure 4.5) (Haimson and Song, 1993). In sandstones, experiments show sharp, V-shaped breakouts which propagate as a series of fractures along grain boundaries (Haimson, 2007; Lee et al., 2016; Song and Haimson, 1997). With increasing confining pressure, borehole breakout geometry changes as shear fractures transition to compaction bands, forming slot shaped fractures with intensely crushed grains (Haimson, 2001; 2003; 2007; Haimson and Kovacich, 2003; Haimson and Lee, 2004). Due to smaller grain sizes and lower porosity, this study does not observe similar manifestations of grain comminution and cataclasis, but the geometries show a transition to long breakouts at the higher σ_3 values (Figure 4.4). In plane strain experiments on Berea sandstone, the resulting breakouts are sharp, V-shaped geometries with shear fractures growing away from the breakout tip, similar to PERP 1.3 (Figure 4.11) (Fakhimi et al., 2002; Labuz and Biolzi, 2007). Localized acoustic emissions show that deformation is localized around the wellbore in Berea sandstone as breakouts initiate, then spread along the growing shear fractures (Labuz and Biolzi, 2007). Shear bands do not start to propagate until stress has peaked, consistent with observations from experiments herein conducted at 6.9 MPa σ_3.

Hydrostatic tests on hollow cylinder tests in shales and sandstones show that anisotropy can create oriented breakouts despite the isotropic stress state (Cuss et al., 2003; Ewy and Cook, 1990b; Meier et al., 2015). In oil shales, the breakout geometry depends on the lamination orientation (Meier et al., 2015). When laminations are parallel or slightly inclined to the cylindrical axis, the failure of the sample results in a rounded, broad breakout (Meier et al., 2015), similar to the breakouts observed in PERP 3, despite the isotropic stress state. In both studies, the breakouts propagate as a series of fractures, increasing in size into the formation. Similar phenomena have also been observed in Tennessee, Darley Dale, and Berea sandstones. Resulting breakouts are oriented with cross- bedding (Cuss et al., 2003; Ewy and Cook, 1990b), similar to observations that PARA and 45D samples are controlled by laminations (Figure 4.9, 4.10).

4.5.3. Effect of Lamination Orientation on Peak Strength

At all confining pressures tested, there is a consistent trend that PARA samples are stronger than PERP samples, which are stronger than 45D samples, reflected in peak differential stress, the failure envelope, and calculated stress at the borehole wall (Figure 4.6, 4.7; Table 4.1). Both PARA and 45D samples have fractures that are strongly controlled by lamination orientation, but there are dramatic differences in strength between the different orientations. PARA samples failed by the formation of long subvertical cracks along laminations which have to open against the confining pressure, and are therefore inhibited at higher confining pressures. Fractures in 45D samples are inclined subparallel to the laminations, i.e. planes of weakness have been reactivated due to stress concentrations from anisotropy.

Mancos Shale is a transversely anisotropic rock, consisting of alternating layers of clay rich and clastic laminations. The change in strength with lamination orientation is a characteristic feature of transversely anisotropic rocks, first established by the work of Donath (1961, 1969, 1972). More recent approaches have been developed to predict anisotropic failure, but the three lamination orientations from this study are insufficient for comparison (Crook et al., 2002; Jaeger et al., 2009; Tien and Kuo, 2001; Walsh and Brace, 1964). Peak stress is highly dependent on lamination orientation, and the results can be fit with a cosine based failure envelope:

$$Differential\ Stress = A - B * \cos(2(C - \theta)), \quad (3)$$

where θ is the inclination of laminations or bedding planes to axial stress, measured in degrees; A, B, and C are constants, with units of MPa (Donath, 1972). A θ of 0° corresponds to PARA samples, and a θ of 90° corresponds to PERP samples. A corresponds to the overall failure strength of the rock; B corresponds to the magnitude of strength change with θ; and C corresponds to the weakest orientation. Figure 4.12 shows the results from this study, as well as results from Pierre Shale and Tournemine Shale (Crook et al., 2002; Niandou et al., 1997). Results are fit with equation 3 (Table 4.3). Results from this study and all other results are presented as differential stress at failure. Mancos and Tournemine Shale samples are adequately described by equation 3 (Table 4.3). Only Pierre Shale is not well described by this relationship, as only the 45º θ sample showed weakening (Crook et al., 2002). Mancos Shale is similar in behavior to Tournemine Shale, and the calculated failure stresses for Mancos Shale are similar for a given confining pressure to Tournemine Shale, resulting in similar A values (Figure 4.13; Table 4.3). Tournemine and Mancos Shale both show that B values increase with confining pressure, or applied minimum stress, indicating larger differences in failure strength for the different lamination orientations (Figure 4.13; Table 4.3). This is also demonstrated by the failure envelopes for PERP, PARA, and 45D samples (Figure 4.7). Mancos Shale has lower B values to Tournemine Shale for similar conditions (Figure 4.13; Table 4.3).

Previous work shows that the minimum strength occurs at inclination angles between 30º and 45º and can increase with increasing confining pressure (Table 4.3) (Donath, 1969; 1972; Ibanez and Kronenberg, 1993; Niandou et al., 1997). For borehole experiments in Mancos Shale, the predicted inclination angle is 59º (Table 4.3). The larger inclination angle value could be a result of fewer data points compared to other studies, but it is likely a result of the fracture orientations associated with borehole breakouts. For standard triaxial compression at relatively low minimum stresses, a fracture angle estimate based on Mohr Coulomb would be around 30º inclination to the axial stress. When shales and foliated rocks are inclined at this orientation, fractures preferentially occur in weak laminations or along parting planes between foliations, resulting in decreased fracture strength compared to other orientations. For borehole breakouts, the expected fracture orientation is controlled by borehole stress concentrations and not by far field stresses. As observed in the PERP samples from this study and isotropic rocks from previous work, the fractures delineating breakouts have a larger inclination angle than larger shear fractures, 45º to 60º inclination (Figure 4.10; Table 4.3) (Haimson, 2007; Haimson and Herrick, 1986; Labuz and Biolzi, 2007; Lee and Haimson, 1993). 45D samples show that fractures grow preferentially along the dark laminations (Figure 4.9, 4.10, 4.12; Table 4.2); samples oriented at 60º inclination are predicted to be weaker with the laminations having a greater influence on fracture orientation.

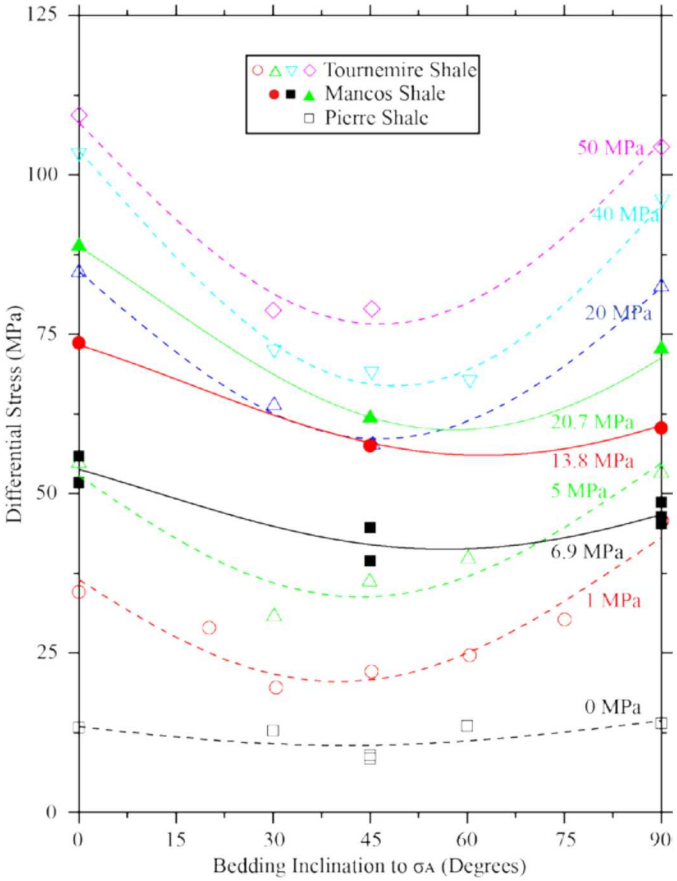

Figure 4.13: Differential stress versus inclination for shales. Inclination is measured as an angle between bedding and axial stress direction. Results from this study are solid symbols, results from other works are shown as open symbols. Confining pressure, or σ_3, is annotated. Data for different shales are fit with equation 3, for this study the curves are solid lines, for results from other works the curves are dashed lines. Curves are annotated with confining pressures. Pierre Shale UCS data is from Crook et al., 2002, and Tournemine Shale data is from Niandou et al., 1997.

Differential Stress = A - B cos 2 (C - bedding inclination)						
Source	Shale	σ_3 (MPa)	A (MPa)	B (MPa)	C (Degrees)	R^2
Crook et al., 2002	Pierre	0	13.9	3.4	41.3	0.45
Niandou et al., 1997	Tournemine	1	39.8	19.3	40.1	0.91
		5	53.8	20.0	43.5	0.9
		20	83.6	25.0	46.4	0.99
		40	99.6	32.7	48.7	0.99
		50	106.7	30.1	46.4	0.98
This Study	Mancos	6.9	50.27	9	56.6	0.83
		13.8	67	11	62.45	---
		20.7	80	20	57.8	---

Table 4.3: Failure envelope parameter fits for failure strength versus bedding angle.

4.5.4. Applications

Borehole breakouts are crucial components to estimate the in situ stress state. Vertical and horizontal stresses can be measured directly, but complications associated with deep petroleum and geothermal wells can lead to high uncertainty. By presuming a particular failure criterion and the mechanical behavior of rocks, borehole breakout measurements can be used to estimate σ_H with increased certainty (Barton et al., 1988; Vernik and Zoback, 1992; Zoback, 2010). This study highlights difficulties in applying this technique in shales and other anisotropic rock formations. Borehole strength depends on lamination orientation, and the relationship changes with confining pressure. The weakest lamination orientation can change as confining pressure changes (Donath, 1972; Niandou et al., 1997). 45D and PARA samples also highlight the issues with measuring breakout widths. At the lowest confining pressure, neither orientation makes a clear breakout. Breakouts are controlled by anisotropy, not stress orientation, similar to observations in hollow cylinders of shale and sandstone (Cuss et al., 2003; Meier et al., 2015). Field observations demonstrated that deviated wellbores and tunnels through shale and other anisotropic rocks can induce wellbore eccentricity, bedding related failure, and stability problems (Edwards et al., 2004; Lisjak et al., 2014; Moos et al., 1998; Okland and Cook, 1998; Vernik and Zoback, 1989; 1990). This type of behavior could lead to errors in stress magnitudes and orientation measurements. Bedding orientation could be particularly problematic for inclined and horizontal boreholes. Estimating maximum horizontal stress in these settings requires matching borehole shapes to model predictions (Peška and Zoback, 1995). Breakouts observed here are highly dependent on lamination distribution around the borehole, making it difficult to predict geometries a priori. Breakouts in wellbores intersecting anisotropic formations at low angles would see asymmetric breakouts unlikely to agree with model predictions, although at deeper depths with elevated pressures this could reverse. Wellbore strength would also be lower than expected, creating potential instability issues.

4.6. Conclusions

This study investigated the use of a novel experimental setup, the Sandia Wellbore Experimental Simulation geometry, or SWESI geometry, to investigate borehole behavior using standard geomechanics load frames. Experiments were conducted on Mancos shale, a finely laminated, transversely anisotropic rock. Samples were deformed in three different orientations with respect to the laminations: parallel, perpendicular, and inclined at 45°, and deformed under confinements of 6.9 MPa, 13.8, and 20.7 MPa applied minimum stresses. The SWESI geometry is capable of creating the type of wellbore deformation observed in the field, previously only achieved in true triaxial experiments. The results show that peak stress, breakout shape, and fracture orientation are dependent on orientation. PARA samples are stronger than PERP samples, which are stronger than 45D samples, and the differences increase with increasing confining pressure. The relationship between failure and confining pressure can be fit by a linear envelope, and the relationship between failure and lamination orientation can be fit by a cosine function. Elastic modeling demonstrates that anisotropy has a significant effect on stress distribution around the wellbore. PERP models predict reduced stress concentrations compared to the isotropic Kirsch solution; PARA models predict increased stress concentrations; and 45D models predict increased compressive and tensile stress concentration rotated away from the applied stress directions.

PERP samples display classic, V-shaped breakouts. Some 45D samples display V-shaped breakouts as well, but observations suggest that breakouts location are controlled by induced tensile stresses from material anisotropy that do not agree with the Kirsch solution. PARA samples do not display classic breakouts and deformation is controlled by the distribution of dark laminations. With increasing confinement, breakouts increase in width, and become a significant portion of the borehole. For PARA and 45D samples, fractures follow the laminations. For PERP samples, there are differences in fracture orientations between the different laminations as fractures in darker laminations are shallower than in light laminations. Fracture measurements also show that fractures occur preferentially in dark laminations. The changes in strength and breakout orientation observed in this study highlight risks for back-calculating in situ stress states in shale and other anisotropic formations.

5. UW PRESTRESSED BOREHOLE TESTING

A series of prestressed borehole breakout tests were performed at the University of Wisconsin Geological engineering lab. The work was overseen by Bezalel Haimson and performed by Cecilia Cheung. Tests were performed at ambient and elevated temperature. The results of these tests were used in subsequent modeling efforts to correlate results from the models to the result of the experiments. The report, generated by UW, is attached in Appendix 1.

Results of this testing showed that relatively high differential stresses between the two horizontal stresses (maximum and minimum principal stress, intermediate stress was always the vertical stress) in order to generate breakouts in this particular rock, which is relatively large grained for a granite, and quite strong.

6. BOREHOLE MODELING

6.1. Section Summary

A series of numeric simulations were run to parameterize the model space which encompasses the prestressed borehole tests performed at the University of Wisconsin. Simulations were performed at many more levels than the tests were in order to fully parameterize the stress space. Results show that there is significant tensile stress generated within the sample in the maximum principal stress plane (σ_H). These are 90 degrees from the location of the borehole breakouts which form due to increased compressive stress at the borehole wall from the far field stresses. The numeric constitutive model implemented with the finite element solver was the Kayenta model described in Section 2 and parameterized with the experimental true triaxial data. This included the effect of the intermediate stress on failure. Results show that there is significant compressive failure around the borehole suggesting that breakouts would form in many of the simulations, the data corresponds well to the experiments performed at the University of Wisconsin. Table 6.1 lists all

Table 6.1. Suite of triaxial test boundary conditions (all pressures in MPa)

Test #	σ_V	σ_H	σ_h	Test #	σ_V	σ_H	σ_h	Test #	σ_V	σ_H	σ_h
1	30	90	30	26	30	90	45	52	30	90	60
2	40	90	30	27	40	90	45	53	40	90	60
3	50	90	30	28	50	90	45	54	50	90	60
4	60	90	30	29	60	90	45	55	60	90	60
5	70	90	30	30	70	90	45	56	70	90	60
6	80	90	30	31	80	90	45	57	80	90	60
7	90	90	30	32	90	90	45	58	90	90	60
8	30	150	30	33	45	90	45	59	30	150	60
9	40	150	30	34	30	150	45	60	40	150	60
10	50	150	30	35	40	150	45	61	50	150	60
11	60	150	30	36	50	150	45	62	60	150	60
12	70	150	30	37	60	150	45	63	70	150	60
13	80	150	30	38	70	150	45	64	80	150	60
14	90	150	30	39	80	150	45	65	90	150	60
15	120	150	30	40	90	150	45	66	120	150	60
16	150	150	30	41	120	150	45	67	150	150	60
17	30	200	30	42	150	150	45	68	30	200	60
18	40	200	30	43	30	200	45	69	40	200	60
19	50	200	30	44	40	200	45	70	50	200	60
20	60	200	30	45	50	200	45	71	60	200	60
21	70	200	30	46	60	200	45	72	70	200	60
22	80	200	30	47	70	200	45	73	80	200	60
23	90	200	30	48	80	200	45	74	90	200	60
24	140	200	30	49	90	200	45	75	140	200	60
25	200	200	30	50	140	200	45	76	200	200	60
				51	200	200	45				

of the far field conditions for the simulations. Please note that in the SIERRA mechanics solver there is no provision for positive compression, so in this section the maximum principal stress is the least compressive, and the minimum principal stress is most compressive, i.e., breakouts form due to the minimum principal stress.

6.2. Description of Computational Model

Besides from the actual test conditions, the computational model for this analysis comprises four essential elements: the computational mesh used for the finite element simulations; the finite element code Adagio; the Kayenta constitutive model for the behavior of a porous geomaterial; and the development of the parameter values for the Kayenta model based on experimental test results. These four elements are described in detail now.

6.2.1. Computational Mesh

The computational mesh for the simulations is shown in Figure 6.1. The mesh geometry matches the geometry of the test samples – 0.127 m (5 inches) square by 0.178 m (7 inches) tall, with a concentric hole of 0.0254 m (1 inch) radius along the height of the test block. The mesh contains 20,080 8-node hexadecimal elements. For plotting convenience, the mesh was grouped in four quartile blocks, with all blocks receiving the same material properties. Figure 6.1 also illustrates

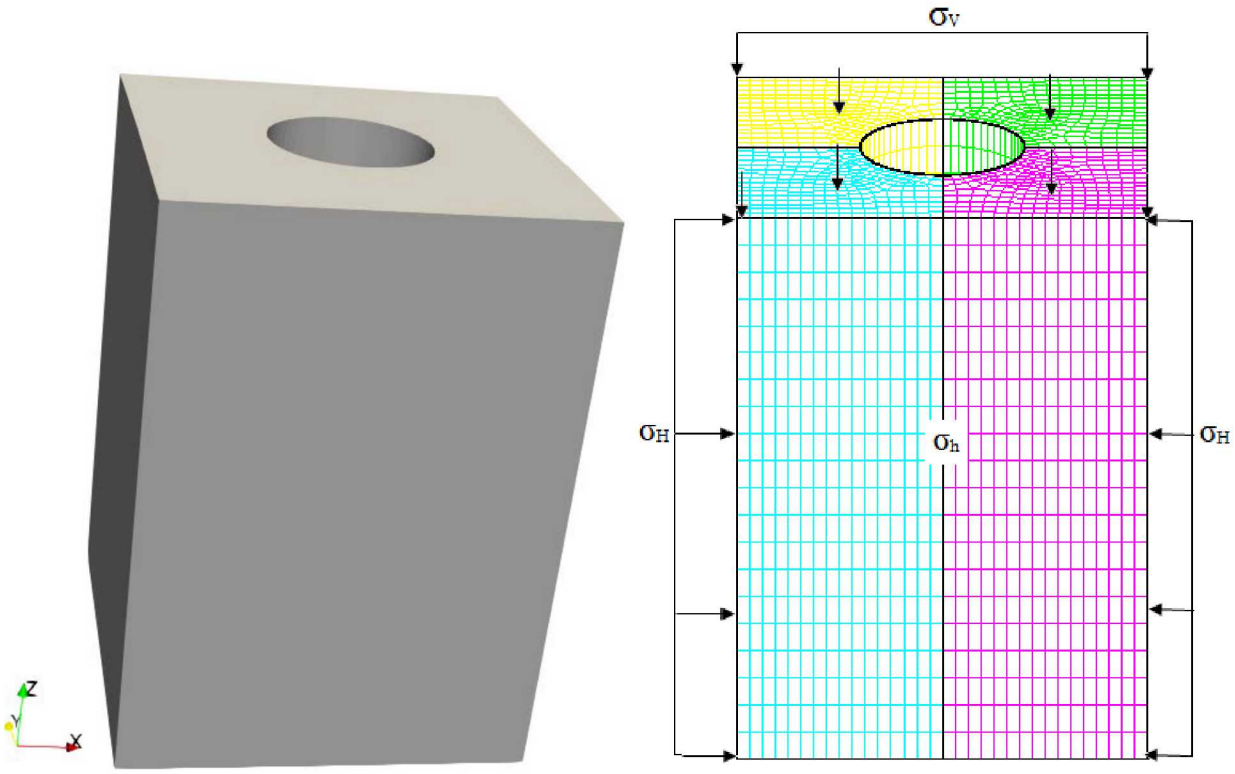

Figure 6.1. Computational domain, mesh and boundary conditions used for analyses.

the boundary conditions applied to the mesh: an axial pressure σ_V applied to the top of the block, and separate horizontal pressures σ_H and σ_h applied to the sides, as described in Table 6.1. For each simulation, the boundary pressures are linearly increased from zero to the final values over a period of one hour, then allowed to remain at the final values for the remainder of a 24-hour period.

6.2.2. Description of Sierra/Adagio

This analysis utilized the high-performance finite element code Adagio (SIERRA Team, 2010, 2011; Arguello et al., 2012), a three-dimensional finite element program developed by Sandia National Laboratories, and designed to solve large quasi-static nonlinear mechanics problems. Adagio is written for parallel computing environments, and its solvers allow for scalable solutions of very large problems. Adagio uses the SIERRA Framework, which allows for coupling with other SIERRA Mechanics codes. The development of the SIERRA Mechanics code suite has been funded by the Department of Energy (DOE) Advanced Simulation and Computing (ASC) program for nearly twenty years (Edwards and Stewart, 2001). The goal is development of massively parallel multi-physics capabilities to support the Sandia engineering sciences mission. SIERRA Mechanics was designed and developed from its inception to run on the latest, most sophisticated, massively parallel computing hardware. It has the capability to span the hardware range from a single workstation to computer systems with thousands of processors. The foundation of SIERRA Mechanics is the SIERRA toolkit, which provides finite element application-code services such as: (1) mesh and field data management, both parallel and distributed; (2) transfer operators for mapping field variables from one mechanics application to another; (3) a solution controller for code coupling; and (4) included third party libraries (e.g., solver libraries, communications package, etc.). The SIERRA Mechanics code suite comprises application codes that address specific physics regimes. Adagio is used for solid mechanics problems by solving quasi-static, large deformation, large strain behavior of nonlinear solids in three dimensions. Adagio has Sandia-developed (i.e., proprietary) technology for solving solid mechanics problems, that involves matrix-free iterative solution algorithms for efficient solution of extremely large and highly nonlinear problems. This advanced technology is especially well-suited for scalable implementation on massively parallel computers.

6.2.3. Description of Kayenta Model

The Kayenta constitutive model (Brannon et al., 2009) is used to model the mechanical response of the granite. The Kayenta model includes features and fitting functions appropriate to a broad class of materials including rocks, rock-like engineered materials such as concretes and ceramics, and metals. Fundamentally, the Kayenta model is a computational framework for generalized plasticity models. As such, it includes a yield surface, but the term "yield" is generalized to include any form of inelastic material response including microcrack growth and pore collapse. In the simplest cases, Kayenta can model linear elastic behavior such as Mohr-Coulomb failure, but with more detailed parameterization can also model complex behavior such as material softening and rate dependence of viscoplastic and pore crushing materials; hydrostatic and triaxial testing are base testing requirements to parameterize more complex behavior. Kayenta has recently used to model behavior of cement casings under a variety of stress conditions (Park, 2014; Gomez et al., 2015).

In the Kayenta model, the bulk and shear moduli are formulated to allow for them to stiffen as voids collapse. These moduli are permitted to vary with plastic strain according Equations 1 and 2, as functions of I_1, the first invariant of the Cauchy stress tensor, J_2, the second invariant of the deviatoric stress, ε_v^p, the plastic compaction volume, and $\gamma^p{}_{equiv}$, the equivalent plastic shear strain:

$$K\left(I_1, J_2, \varepsilon_v^p\right) = \left[b_0 + b_1 \exp\left(-\frac{b_2}{|I_1|}\right)\right] - b_3 \exp\left(-\frac{b_4}{|\varepsilon_v^p|}\right) \qquad [1]$$

$$G\left(J_2, \gamma_{equiv}^p\right) = g_0 \left[\frac{1-g_1 \exp\left(-g_2 J_2^{1/2}\right)}{1-g_1}\right] - g_3 \exp\left(-\frac{g_4}{\gamma_{equiv}^p}\right) \qquad [2]$$

Kayenta models microcracked material by providing flexible fitting functions that can reproduce octahedral and meridional yield profiles observed for real materials. The shear limit function used in Kayenta sets the shear limit surface behavior in triaxial compression as a function of I_1:

$$F_f(I_1) = a_1 - a_3 e^{-a_2 I_1} + a_4 I_1 \qquad [3]$$

This shear limit forms the basis for the yield surface (or failure surface) function, which also includes a dependence upon the Lode angle $\bar{\theta}$. By definition, the Lode angle varies from $\bar{\theta} = \pi/6$ for triaxial extension, $\bar{\theta} = 0$ for simple shear, and $\bar{\theta} = -\pi/6$ for triaxial compression (for the convention of tension being positive). The failure surface formulation in Kayenta is:

$$\sqrt{J_{2,yield}} = F_f(I_1)/\Gamma(\bar{\theta}, \varphi) \qquad [4]$$

The Lode angle dependence function Γ depends on a parameter ψ which is an expression of the triaxial extension/compression strength ratio at a given pressure. Kayenta allows three options for Lode angle dependence: 1. Gudehus (an efficient smoothed profile, with restrictions on convexity); 2. Willam-Warnke (a relatively inefficient smooth profile with no convexity constraints); and 3. Mohr-Coulomb (distorted hexagon polygon). All three of the models honor the data in a curve-fitting sense, and produce an octahedral yield profile that presumes that only the size of the octahedral yield profile — not its shape — varies with pressure. Instruction provided in Brannon et al. (2009) were used to fit the test data using the three different options for Γ. Ultimately, the best fit was obtained using the Willam-Warnke model, with an R^2 value of 0.99. The Willam-Warnke Γ function is defined as (Willam and Warnke, 1975):

$$\textbf{Willam-Warnke: } \Gamma(\bar{\theta}) = \frac{4(1-\psi^2)\cos^2\alpha^* + (2\psi-1)^2}{2(1-\psi^2)\cos\alpha^* + (2\psi-1)\sqrt{4(1-\psi^2)\cos^2\alpha^* + 5\psi^2 - 4\psi}},$$

$$\text{where } \alpha^* = \frac{\pi}{6} + \bar{\theta}. \quad \text{The Willam-Warnke option is convex for } \frac{1}{2} \le \psi \le 2. \qquad [5]$$

The Kayenta model parameters developed from are listed in Table 6.2. The yield surface generated by the Eqs. 3, 4, and 5 parameters in Table 6.2 (a1, a2, a3, a4, and RK or ψ), are illustrated in Figure 6.2. Originally, the yield function parameters a2 and a3 in Eq. 3 were assumed to be zero, as the yield behavior of the granite samples exhibited a nearly linear behavior as a function of I1

and J2. However, there were some numerical issues in initiating the calculations as the boundary pressures were increased from zero. A remedy for this was found by including relatively small values for a2 and a3, which changes the shear function only slightly at very low pressures. Figure 6.3 illustrates the shear function with both sets of parameters.

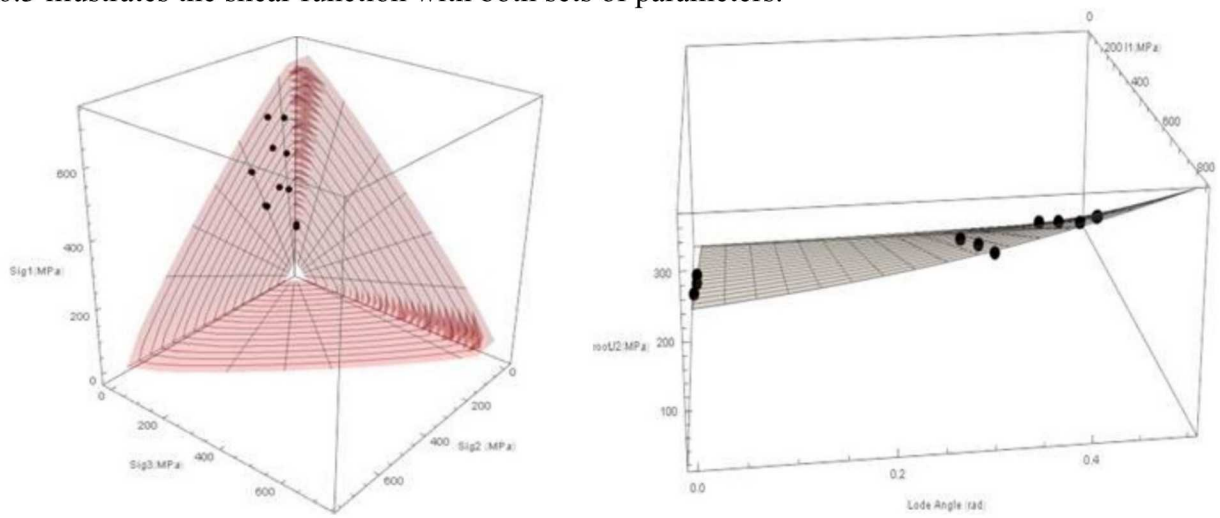

Figure 6.2. Yield surface of the granite samples used in the laboratory tests.

Table 6.2: Material properties of granite samples using the Kayenta constitutive model (Brannon et al., 2009).

Parameter	Value	Description
ρ	2100 kg/m^3	Density
v	0.2773	Poisson's Ratio
B0	61.024x10^9 Pa	Initial elastic bulk modulus (Eq. 1)
B1	144.3x10^9 Pa	High pressure coefficient in nonlinear elastic bulk modulus function
B2	148x10^6 Pa	Curvature parameter in nonlinear elastic bulk modulus function
B3	100x10^6 Pa	Coefficient in nonlinear elastic bulk modulus to allow for plastic softening
B4	0.002	Power in nonlinear elastic bulk modulus softening
G0	31.919x10^9 Pa	Initial elastic shear modulus (Eq. 2)
G1	0.05	Coefficient in shear modulus hardening
G2	0.02 Pa^{-1}	Curvature parameter in shear modulus hardening
G3	1x10^9 Pa	Coefficient in shear modulus softening
G4	0.03	Power in shear modulus softening
A1	28.815x10^6 Pa	Constant term for meridional profile function of ultimate shear limit surface (Eq. 3)
A2	0.03x10^{-6} Pa^{-1}	Curvature decay parameter in the meridional profile function
A3	6.51x10^6 Pa	Parameter in the meridional profile function
A4	0.419 rad	High-pressure slope parameter in meridional profile function
P0	-1.0x10^{99} Pa	One third of the elastic limit pressure parameter at onset of pore collapse (default value)
P1	0 Pa^{-1}	One third of slope of porosity vs. pressure crush curve at elastic limit
P2	0 Pa^{-2}	Parameter for hydrostatic crush curve
P3	0.0	Asymptote of the plastic volumetric strain for hydrostatic crush
CR	0.001	Parameter for porosity affecting shear strength
RK	0.579	Triaxial extension strength to compression strength ratio (ψ in Willam-Warnke model)
J3TYPE	2	Type of 3rd deviatoric stress invariant function (1-Gudehus,2-Willam-Warnke,3-Mohr-Coulomb)

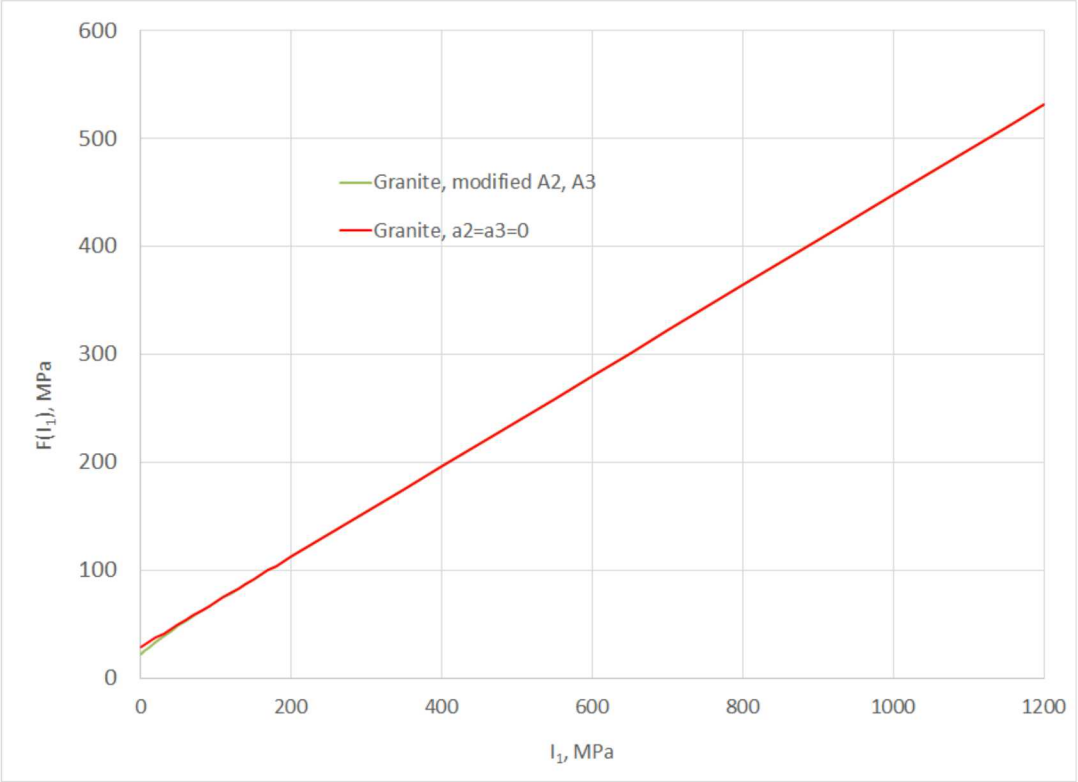

Figure 6.3. Effect of minor changes to a2, a3 in Equation 3.

6.3. Results of Computational Model

For all the tests except for those with the smallest difference in the applied horizontal stresses, the simulations predict regions of tensile and compressive stresses resulting in deviatoric stresses high enough to reach the yield stress curve shown in Figure 6.3. The tensile stresses occur due to the triaxial extension created by the large x-direction horizontal boundary pressure, which is greater than the vertical and orthogonal horizontal boundary pressures coupled with the hole in the specimen. Compressive stresses arise directly from the applied load as well as the stress concentration due to the hole in the specimen. The next several figures illustrate these conditions for Test 8, for which σ_V =30 MPa, σ_H =150 MPa, and σ_h =30 MPa. Figure 6.4 plots the vertical stresses predicted in the block, and also separates those elements for which that stress is larger in compression than the applied vertical load. Note that the 30 MPa pressure applied at the top surface changes drastically down into the test sample, with much larger compressive stresses on the back side of the borehole and large tensile stresses on the left and right sides of the borehole. The drastic stress differences are caused by stress concentrations around the hole in the specimen created by the larger x-direction horizontal pressure. This observation is enhanced in Figure 6.5, where the minimum principal stress is shown ("minimum" in this case being most negative, so either most compressive or least tensile stress). The region of minimum principal stress includes both the region of negative vertical stress and an extension up to the top of the test block. These negative stresses occur at the borehole surface normal to the direction of the larger horizontal pressure (y-direction). As expected the minimum principal stress on the y-direction surface of the borehole are extremely compressive indicating that a borehole breakout is likely in that region.

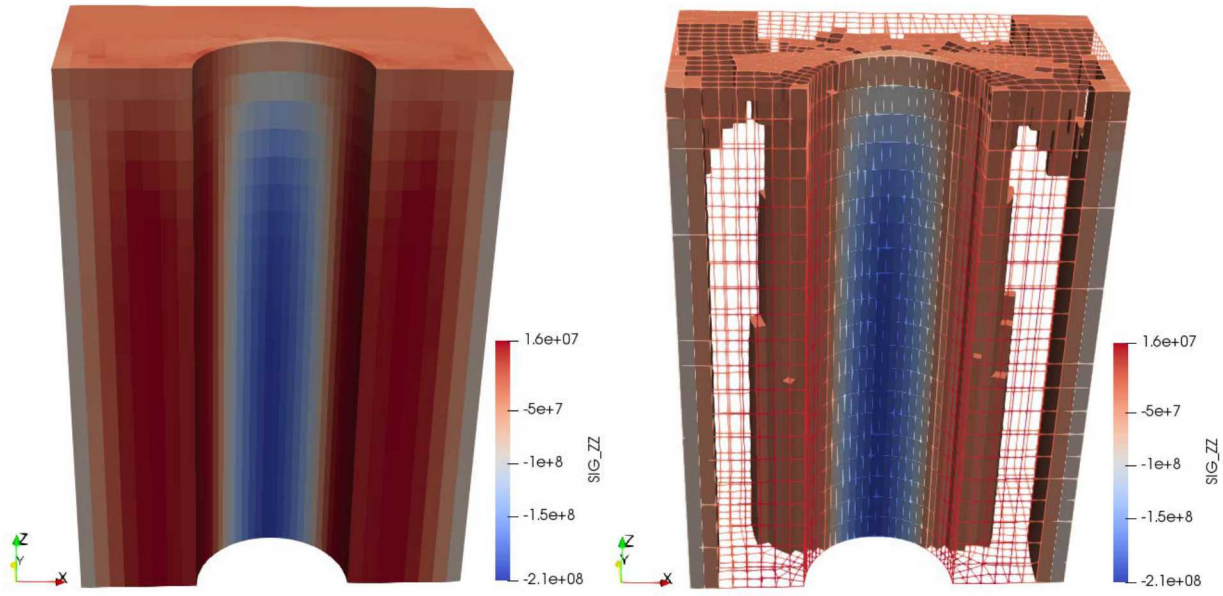

Figure 6.4. Results of Test 8 simulation, showing elements of compressive vertical stress larger than the applied stress(MPa).

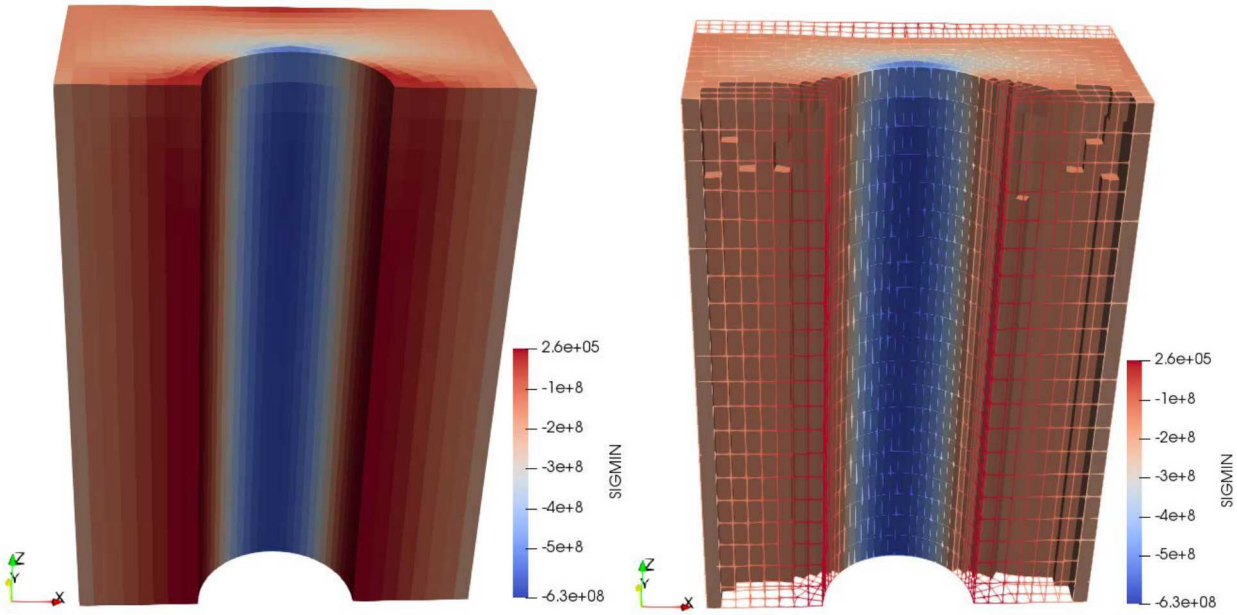

Figure 6.5. Results of Test 8 simulation, showing elements of negative minimum principal stress (MPa).

Figure 6.6 shows the predicted x- and y-directions stresses for Test 8. All stresses in the x-direction are predicted to be compressive, with the expected zero stress at the x-axis edges of the borehole. The back side of the borehole shows compressive stresses which are over four times the horizontal applied pressure of 150 MPa, indicating a region which is well suited for borehole breakout. For

the y-direction stresses, the edges of the borehole at the front are predicted to have significant hoop stress tension.

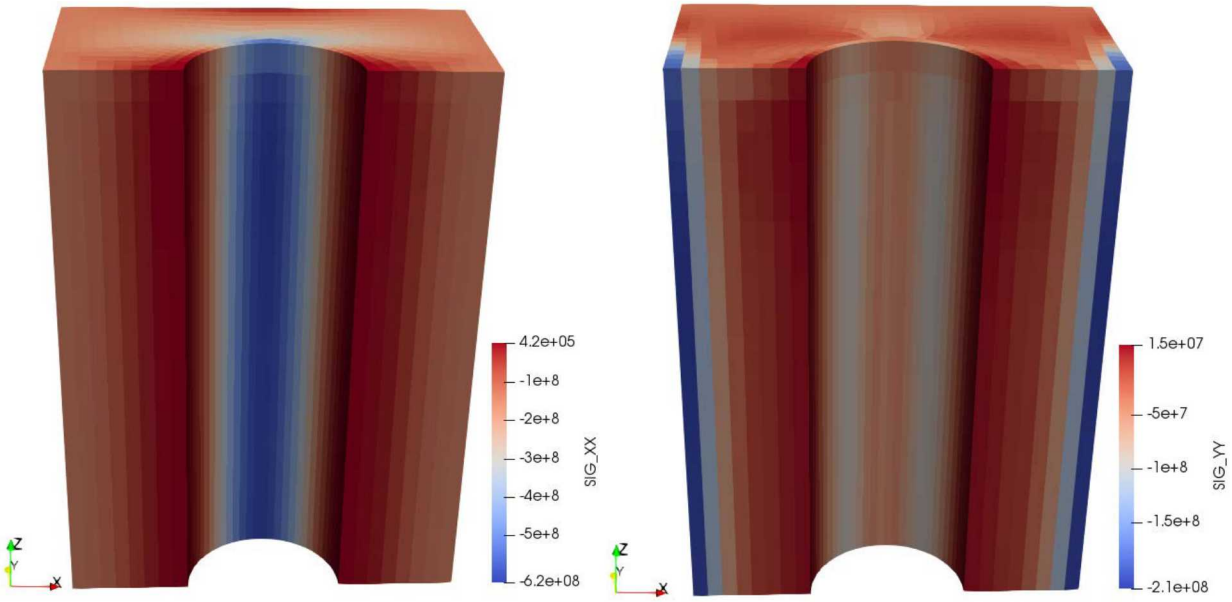

Figure 6.6. Results of Test 8 simulation, with x-direction and y-direction stresses (MPa).

In addition to the behavior of normal stresses resulting from the triaxial application of pressures, there are shear stresses generated as well. Equations 3 and 4 express how the Kayenta model defines the failure envelope in terms of J_2, the second invariant of the deviatoric stress. The computational model calculates J_2, for each element. When and where this value reaches the yield stress value defined by Eq. 4, the sample is predicted to experience failure. A post-simulation variable, RJ2_KAY, was defined to express the condition of the deviatoric stress; this ratio equals 1 when yield conditions are reached:

$$RJ2_{KAY} = \frac{\sqrt{J_2}}{\sqrt{J_{2,yield}}} \qquad [6]$$

Figures 6.7 through 6.10 show the extent of predicted yield stresses for four of the tests, which describe a wide range of the stress regimes of the suite of tests. Figure 6.7 plots these values for Test 8, and also which elements achieve shear stress conditions such that RJ2_KAY=1. In comparison with Figures 6.4 and 6.5, the region in Figure 6.7 indicating failure in shear includes most, if not all, of the tensile stress regimes, and then elements along the borehole wall in the y-direction indicating a high likelyhood of borehole breakouts. The results in Figure 6.7 indicate that large deviatoric stresses will extend into the direction of the larger horizontal pressure. Figure 6.8 shows these results for Test 7 (σ_V =90 MPa, σ_H =90 MPa, σ_h =30 MPa), for which the vertical and major horizontal pressures are the same. The region of predicted shear failure is small and at the borehole aligned with the larger, x-direction pressure, indicating that borehole breakout is not likely. Figures 6.9 and 6.10 show the results for tests with increasingly larger pressure differentials: Test 16 (σ_V =150 MPa, σ_H =150 MPa, σ_h =30 MPa), and Test 17 (σ_V =30 MPa, σ_H =200 MPa, σ_h =30 MPa). Finally, several simulations for tests with smaller deviations among the

three applied pressures did not predict any regions where the shear yield surface was attained; these tests were Tests 26 through 33, and 52-58.

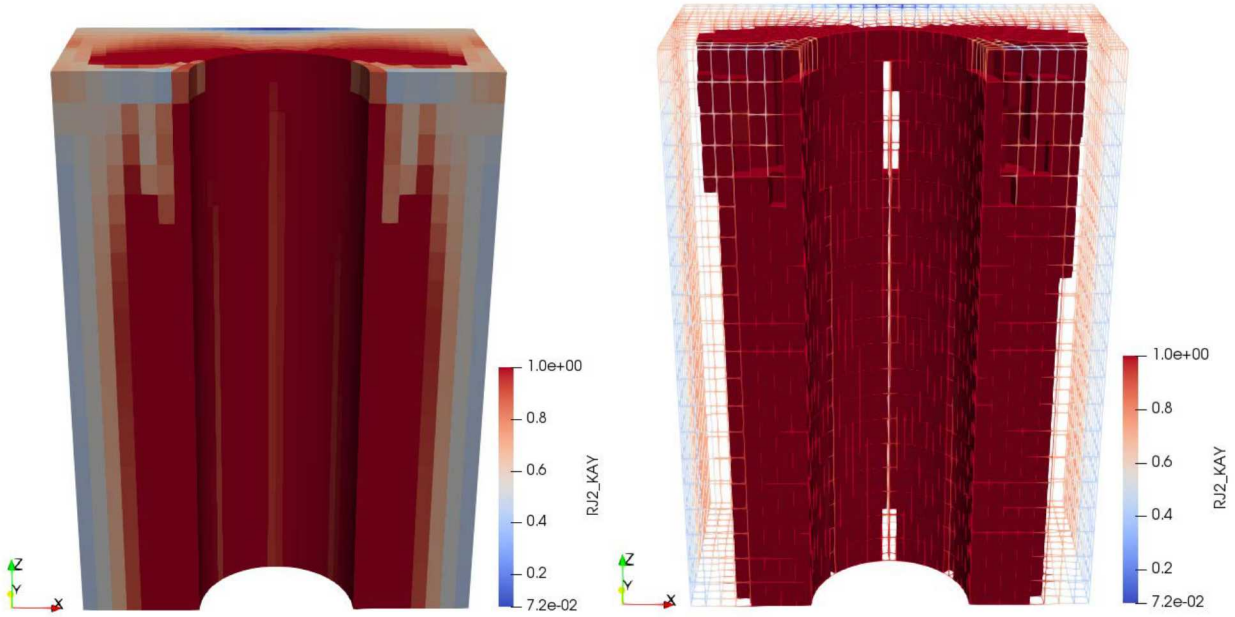

Figure 6.7. Results of Test 8 simulation, showing elements where predicted shear stresses match yield conditions.

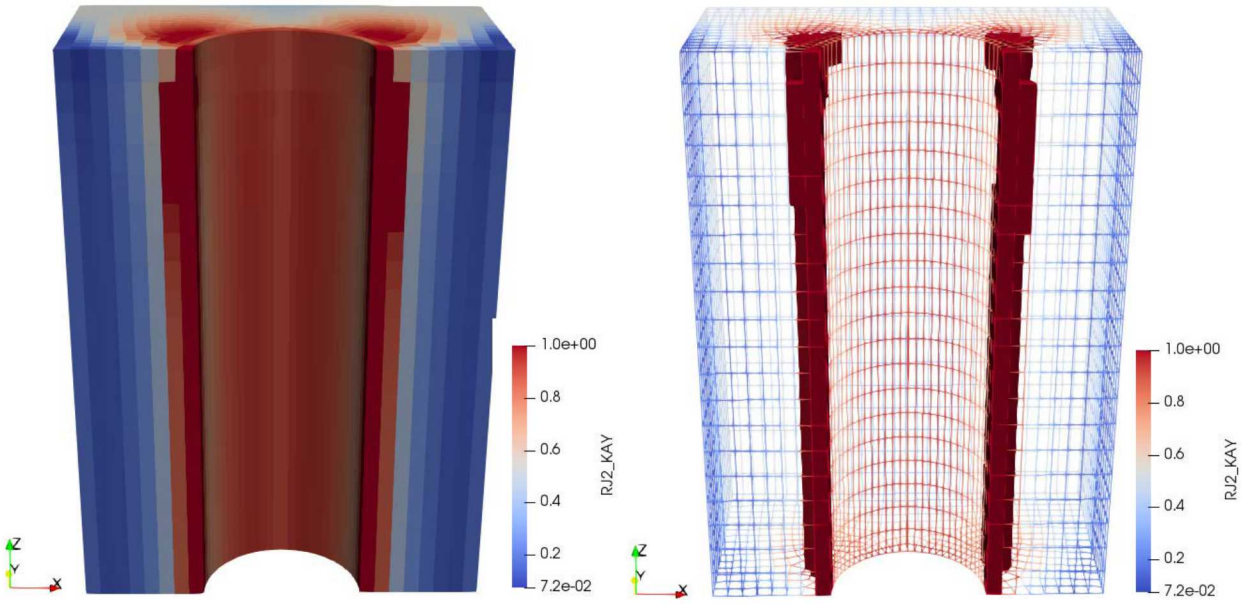

Figure 6.8. Results of Test 7 simulation, showing elements where predicted shear stresses match yield conditions.

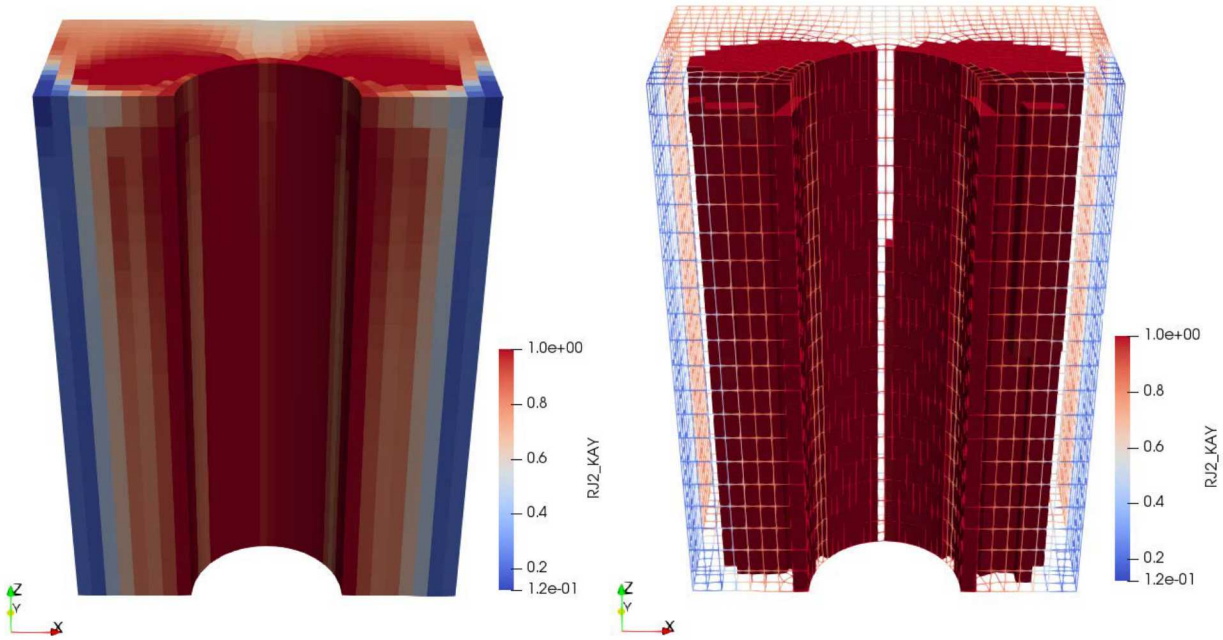

Figure 6.9. Results of Test 16 simulation, showing elements where predicted shear stresses match yield conditions.

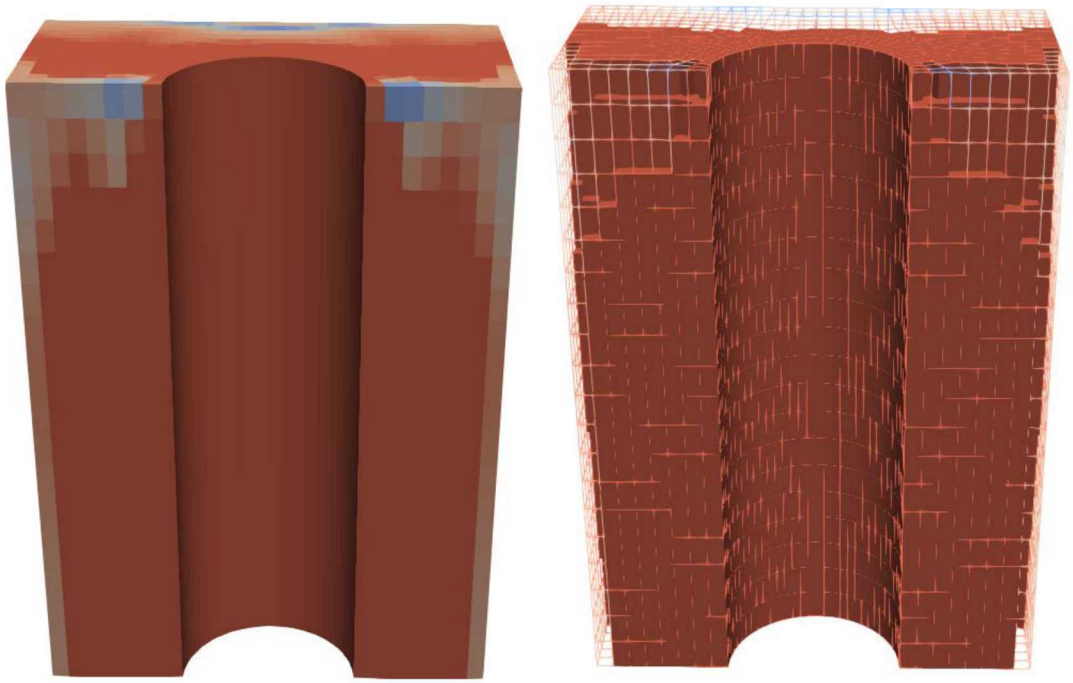

Figure 6.10. Results of Test 17 simulation, showing elements where predicted shear stresses match yield conditions.

The volume of each of the test samples that achieved yield in shear according to the Kayenta model varied greatly depending on the average pressure and corresponding deviatoric stress of each test. In order to make a comparison of the effect of the pressure differentials on the scale of predicted

shear failure, certain parameters have been defined based on the test conditions. Using a test value of I_1 equal to the sum of the three applied pressures, with a resulting average pressure $s=I_1/3$, a deviatoric stress based on test boundary conditions can be defined:

$$\sqrt{\sim J_2} = \sqrt{0.5[(s-\sigma_V)^2 + (s-\sigma_H)^2 + (s-\sigma_h)^2]} \qquad [7]$$

Figures 6.11 and 6.12 show the percentage of elements in the computational model for each test whose predicted shear stresses met the yield surface. These values approximately represent the percentage volume of the sample to reach yield in shear. Figure 6.11 plots these percentages against the test-based deviatoric stress in Equation 7; Figure 6.12 plots them against the ratio of deviatoric stress to average pressure. Red dots indicate simulations where the final stress state was not reached in the calculation due to numerical instability and lack of convergence (Tests 17-25, for which ($\sigma_H - \sigma_h$) was the largest); for these simulations, the stress state at the last time step that reached convergence is plotted. There is a stronger correlation to the effective, test-based deviatoric stress.

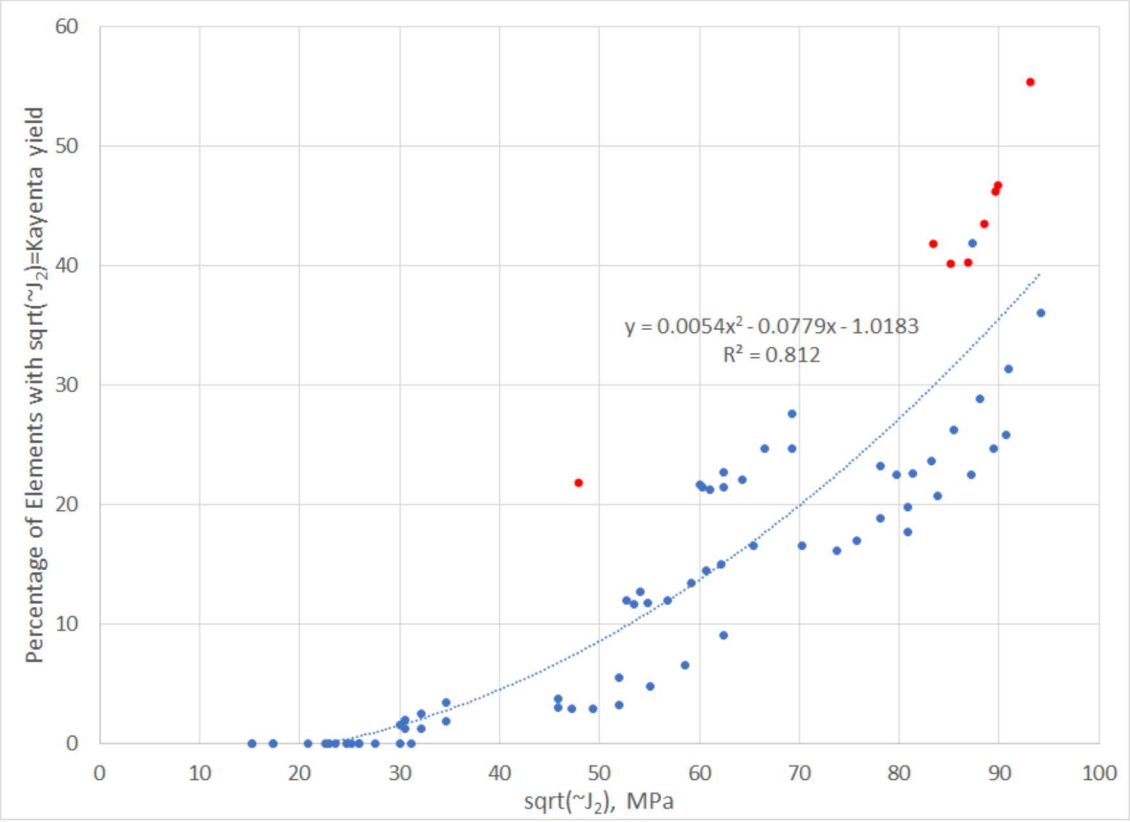

Figure 6.11. Percentage of elements reaching yield stress for each test as function of deviatoric stress based on boundary pressures (Eq. 6).

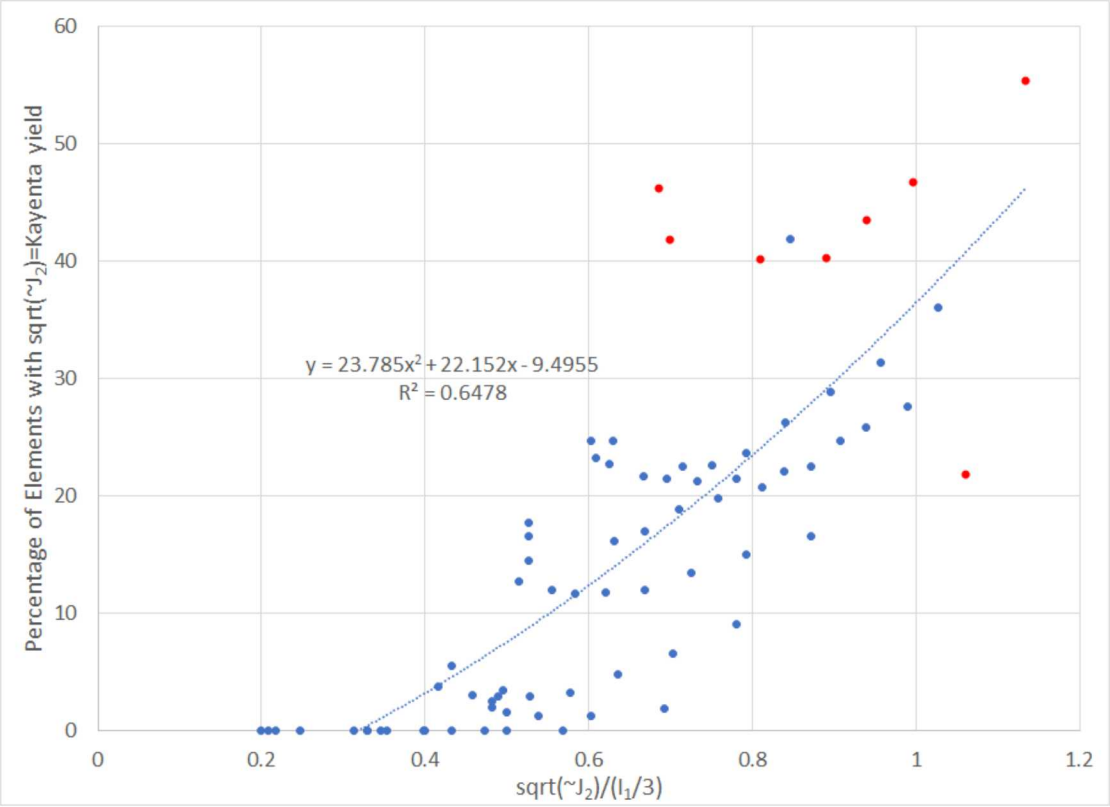

Figure 6.12. Percentage of elements reaching yield stress for each test as function of ratio of deviatoric stress to average pressure.

7. CONCLUSIONS

There are a number of conclusions to be drawn from this work. Most importantly is that the application of more advanced constitutive models can greatly improve the estimation of borehole breakout. This allows for a better understanding of the state of stress in the earth. This primarily arises from the effect of the intermediate principal stress on the elasto-plastic response of materials. Elastic modeling, in its current state using relatively simplistic constitutive models works well for Sierra White granite, indicating that it is sufficient for nearly isotropic and homogeneous rocks. It is suspected that this is likely not true for anisotropic and heterogeneous materials, however more testing is necessary. The elasto-plastic modeling was shown to depend significantly on the intermediate principal stress, even for isotropic and homogeneous materials. This effect should be amplified as the material in question becomes more complicated.

Results from modeling and experimental investigations show good correlation between the experiments and simulations run with the more advanced constitutive model. The numeric simulations did not have the ability to remove failed elements, so it is difficult to exactly model the experimental results, but a good correlation is seen regardless.

Also, a new test geometry was developed for testing borehole breakout in conventional triaxial cells. This was validated with numeric modeling, using both Sierra White granite and Mancos Shale. This suggests that the testing configuration should be valid for most geomaterials.

Results suggest that a more advanced constitutive model applied to borehole breakout data should be able to reduce the uncertainty in estimations of the intermediate principal stress in situ. This would allow for more accurate modeling of the subsurface, and better selection of well sites.

REFERENCES

Al-Ajimi AM, Zimmerman RW (2005) Relation between the Mogi and the Coulomb failure criteria. Int. J. Rock Mech. Min. Sci. 42:431-439.

Arjang, B., and Herget, G. (1997). In situ ground stress in the Canadian hardrock mines: an update. *International Journal of Rock Mechanics and Mining Sciencs, 34*(3-4), 15e1-15e16.

Barton, C. A., Zoback, M. D., and Burns K. L. (1988). In-situ stress orientation and magnitude at the Fenton Geothermal Site, New Mexico, determined from wellbore breakouts. *Geophysical Research Letters, 15*(5), 467-470, doi:10.1029/GL015i005p00467.

Bateman, P.C., Sawka, W.N. (1981) Raymond Quadrangle, Madera and Mariposa counties, California – analytic data. United States Geological Survey Professional Paper 1214, 16p.

Baud, P., Louis, L., David, C., Rawling, G. C., and Wong T. F. (2005). Effects of bedding and foliation on mechanical anisotropy, damage evolution and failure mode. *Geological Society, London, Special Publications, 245*(1), 223-249.

Bauer, S. J., Holland, J. F., and Parrish, D. K. (1985). *Implications about in situ stress at Yucca Mountain*. Paper presented at 26th U.S. Symposium on Rock Mechanics, Rapid City, South Dakota.

Bazant, Z. P., Lin, F., and Lippman, H. (1993). Fracture energy release and size effect in borehole breakouts. *International Journal for Numerical and Analytical Methods in Geomechanics, 17*(1), 1-14.

Bell, J. S., and Gough, D. I. (1979). Northeast-southwest compressive stress in Alberta. Evidence from oil wells. *Earth and Planetary Science Letters 45*(1). 475-482.

Bennett, K. C., Berla, L. A., Nix, W. D., and Borja R. I. (2015). Instrumented nanoindentation and 3D mechanistic modeling of a shale at multiple scales. *Acta Geotechnica, 10*(1), 1-14.

Bobko, C., and Ulm F. J. (2008). The nano-mechanical morphology of shale. *Mechanics of Materials, 40*(4), 318-337.

Borm G, Engeser B, Hoffers B, Kutter HK, Lempp C (1997) Borehole instabilities in the KTB main borehole. J. Geophys. Res. 102:18507-18517.

Bradley, W. B. (1979). Failure of inclined boreholes. *Journal of Energy Resource Technology, 101*(4), 232-239.

Brady PV, Arnold BW, Freeze GA, Swift PN, Bauer SJ, Kanney JL, Rechard RP, Stein JS (2009) Deep Borehole Disposal of High-Level Radioactive Waste. SAND2009-4401, Sandia National Laboratories, Albuquerque, New Mexico. doi:10.2172/985495

Brannon, R.M. (2007) Elements of Phenomenological Plasticity: Geometrical Insight, Computational Algorithms, and Applications in Shock Physics. Shock Wave Science and Technology Reference Library: Solids I. Springer, New York. 2, 189-274.

Brannon, R.M., A.F. Fossum, and O.E. Strack, 2009. KAYENTA: Theory and User's Guide, SAND2009-2282, Sandia National Laboratories, Albuquerque, New Mexico.

Brannon, R.M., Leelavanichkul, S. (2010) A multi-stage return algorithm for solving the classical damage component of constitutive models for rocks, ceramics, and other rock-like media. Int. J. Fract. 163, 133-149.

Brudy M, Zoback MD, Fuchs K, Rummel F, Baumgartner J (1997) Estimation of the complete stress tensor to 8 km depth in the KTB scientific drill holes: Implications for crustal strength. J. Geophys. Res. 102:18453-18475.

Brudy, M., Zoback, M. (1999) Drilling-induced tensile wall-fractures: implications for determination of in situ stress orientation and magnitude. Int. J. Rock Mech. Mining Sci. 36, 191-215.

Cardozo, N., and Allmendinger R. W. (2013). Spherical projections with OSXStereonet, *Computers & Geosciences, 51*, 193-205.

Cheatham, J. (1993). A new hypothesis to explain stability of borehole breakouts. *International Journal of Rock Mechanics and Mining Sciences & Geomechanics Abstracts 30*(7), 1095-1101.

Chang C, Haimson B (2000) True triaxial strength and deformability of the German Continental Deep Drilling Program (KTB) deep hole amphibolite. J. Geophys. Res., 105:18999-19013.

Choens, R. C., Ingraham, M. D., Lee, M. Y., and Dewers, T. A. (2017, December). *Novel experimental techniques to investigate wellbore damage mechanisms.* Presented at The AGU Fall Meeting, New Orleans, LA.

Crook, A. J., Yu, J.-G., and Wilson S. M. (2002). *Development of an orthotropic 3D elastoplastic material model for shale.* Paper presented at SPE/ISRM Rock Mechanics Conference, Irving, Texas.

Cuss, R., Rutter, E., and Holloway R. (2003). Experimental observations of the mechanics of borehole failure in porous sandstone. *International Journal of Rock Mechanics and Mining Sciences, 40*(5), 747-761.

Dewers, T., Eichhubl, P., Ganis, B., Gomez, S., Heath, J., Jammoul, M., Kobos, P., Liu, R., Major, J., Matteo, E., Newell, P., Rinehart, A., Sobolik, S., Stormont, J., Reda Taha, M., Wheeler, M., White, D. (2018) Heterogeneity, pore pressure, and inhectate chemistry: Control measures for geologic carbon storage. Int. J. Greenhouse Gas Control 68, 203-215.

Dewers, T., Newell, P., Broome, S., Heath, J., Bauer, S. (2014) Geomechanical behavior of Cambrian Mount Simon Sandstone reservoir lithofacies, Iowa Shelf, USA. Int. J. Greenhouse Gas Control 21, 33-48.

Dewers, T.A., Issen, K.A., Holcomb, D.J., Olsson, W.A., Ingraham, M.D. (2017) Strain Localization and Elastic-Plastic Coupling During Deformation of Porous Sandstone. International Journal of Rock Mechanics and Mining Sciences, 98C, 167-180.

Dewhurst, D. N., and Siggins, A. F. (2006). Impact of fabric, microcracks, and stress field on shale anisotropy. *Geophysical Journal International 165*(1), 135-148.

Dienes, J. (1975) A high-pressure kinematic hardening model for rocks and soils. J. Geophys. Res. 80, 3749-3754.

Donath, F. A. (1961). Experimental study of shear failure in anisotropic rocks. *Geological Society of America Bulletin, 72*(6), 985-989.

Donath, F. A. (1969). The development of kink bands in brittle anisotropic rock. *Geological Society of America Memoirs, 115*(1), 453-494.

Donath, F. A. (1972). Effects of cohesion and granularity on deformational behavior of anisotropic rock. *Geological Society of America Memoirs, 135*(1), 95-128.

Durrheim, W. D., Roberts, R. J., Haile, M. K. C., Hagan, A. T., Jager, A. J., Handley, M. F., Spottiswoode, S. M., and Ortlepp, W. D. Factors influencing the severity of rockburst damage in South African gold mines. *Journal of the Southern African Institue of Mining and Metallurgy, 98*(2), 53-57.

Dresen, G., Stanchits, S., and Rybacki E. (2010). Borehole breakout evolution through acoustic emission location analysis. *International Journal of Rock Mechanics and Mining Sciences, 47*(3), 426-435.

Edwards, H. C., & Stewart, J. R. 2001. *SIERRA: A Software Environment for Developing Complex MultiPhysics Applications*. Amsterdam : Elsevier, 2001. In K. J. Bathe (ed.), First MIT Conference on Computational Fluid and Solid Mechanics.

Edwards, S., Matsutsuyu, B., and Wilson, S. M. (2004). *Imaging unstable wellbores while drilling.* Paper presented at SPE Annual Technical Conference and Exhibition, San Antonio, TX.

Ellsworth, W. L. (2013). Injection-induced earthquakes. *Science, 341*(6142), 1225942-1-7.

Emmermann R, Lauterjung J (1997) The German Continental Deep Drilling Program KTB: Overview and major results. J. Geophys. Res. 102:18179-18201.

Ewy, R. T. (2002). 3D stress effects on the failure of tunnels, wellbores and hollow cylinders, paper presented at Proceedings of NARMS-TAC 2002, Toronto, Ontario, Canada.

Ewy, R. T., and Cook, N. G. W. (1990a). Deformation and fracture around cylindrical openings in rock – I. Observations and analysis of deformations. *International Journal of Rock Mechanics and Mining Sciences & Geomechanics Abstracts 27*(5), 387-407.

Ewy, R. T., and Cook, N. G. W. (1990b). Deformation and fracture around cylindrical openings in rock – II. Initiation, growth, and interaction of fractures. *International Journal of Rock Mechanics and Mining Sciences & Geomechanics Abstracts 27*(5), 409-427.

Fakhimi, A., Carvalho, F., Ishida, T., and Labuz J. F. (2002). Simulation of failure around a circular opening in rock. *International Journal of Rock Mechanics and Mining Sciences, 39*(4), 507-515.

Foster, C.D., Regueiro, R.A., Fossum, A.F., Borja, R.I. (2005) Implicit numerical integration of a three-invariant, isotropic/kinematic hardening cap plasticity model for geomaterials. Comput. Methods Appl. Mech. Eng. 194, 5109-5138.

Gaede, O., Karrech, A., and Regenauer-Lieb, K. (2013). Anisotropic damage mechanisms as a novel approach to improve pre- and post-failure borehole stability analysis. *Geophysics Journal International, 193*(3), 1095-1109

Ganzaniol, D., Forsans, T., Boisson, M. J. F., and Piau J-M., (1995). Wellbore failure mechanisms in shales: prediction and prevention. *Journal of Petroleum Technology, 47*(7), 589-595.

Gomar, M., Goodarznia, I., Shadizadeh, S. R. (2014) Transient thermos-poroelastic finite element analysis of borehole breakouts. Int. J. Rock Mechanics Mining Sci. 71, 418-428.

Gomez, S.P., S.R. Sobolik, E.N. Matteo, M.R. Taha, and J.C. Stormont, 2017. "Investigation of wellbore microannulus permeability under stress via experimental wellbore mock-up and finite element modeling," *Computers and Geotechnics*, Elsevier Ltd., 83, pp. 168–177.

Gough, D. I., and Bell, J. S. (1981). Stress orientations from oil-well fractures in Alberta and Texas. *Canadian Journal of Earth Sciences, 18*(3), 638-645.

Gough, D. I., and Bell, J. S. (1982). Stress orienations from borehole wall fractures with examples from Colorado, east Texas, and northern Canada. *Canadian Journal of Earth Sciences, 19*(7), 1358-1370.

Green, A. E., and Taylor, G. I. (1939). Stress systems in aeolotropic plates, I. *Proceedings of the Royal Society of London A, 173*(953), 162-172.

Green, A. E., and Taylor, G. I. (1940). Stress systems in aeolotropic plates, III. *Proceedings of the Royal Society of London A, 184*(997), 181-195.

Gross, M. R. (1995). The origin and spacing of cross joints: examples from the Monterey Formation, Santa Barbara Coastline, California. *Journal of Structural Geology, 15*(6), 737-751.

Haimson, B. C. (1989) Hydraulic fracturing stress measurements. *Rock Mechanics and Mining Sciences and Geomechanics Abstrasts*, *International Journal 26.*

Haimson B, Chang C (2000) A new true triaxial cell for testing mechanical properties of rock, and its use to determine rock strength and deformability of Westerly granite. Int. J. Rock Mech. Min. Sci. 37:285-296.

Haimson, B. C. (2001). Fracture-like borehole breakouts in high-porosity sandstone: Are they caused by compaction bands? *Physics and Chemistry of the Earth, Part A: Solid Earth and Geodesy, 26*(1), 15-20.

Haimson, B. C. (2003). Borehole breakouts in Berea sandstone reveal a new fracture mechanism. In Kumpel, H. J. (Ed.), *Thermo-Hydro-Mechanical Coupling in Fractured Rock* (pp. 813-831). Basel, Switzerland: Birkhauser.

Haimson, B. C. (2007). Micromechanisms of borehole instability leading to breakouts in rocks. *International Journal of Rock Mechanics and Mining Sciences, 44*(2), 157-173.

Haimson, B.C., Herrick, C.G. (1985) In situ stress evaluation from borehole breakouts – experimental studies. Proc. 26th U.S. Symp. Rock Mechanics. Rapid City, 1207-1218.

Haimson, B. C., and Herrick C. G. (1986). *Borehole breakouts-a new tool for estimating in situ stress?* Paper presented at International Symposium on Rock Stress and Rock Stress Measurements, Stockholm, Sweden.

Haimson, B. C., and Kovacich J. (2003). Borehole instability in high-porosity Berea sandstone and factors affecting dimensions and shape of fracture-like breakouts. *Engineering Geology, 69*(3), 219-231.

Haimson, B. C., and Lee H. (2004). Borehole breakouts and compaction bands in two high-porosity sandstones. *International Journal of Rock Mechanics and Mining Sciences, 41*(2), 287-301.

Haimson, B. C., and Song I. (1993). Laboratory study of borehole breakouts in Cordova Cream: a case of shear failure mechanism. *International Journal of Rock Mechanics and Mining Sciences & Geomechanics Abstracts, 30*(7), 1047-1056.

Healy, J. H., Rubey, W. W., Griggs, D. T., and Raleigh, C. B. (1968). The Denver earthquakes. *Science, 161*(3848), 1301-1310.

Heidbach, Oliver; Rajabi, Mojtaba; Reiter, Karsten; Ziegler, Moritz; WSM Team (2016): World Stress Map Database Release 2016. GFZ Data Services. http://doi.org/10.5880/WSM.2016.001.

Heidbach, O., Tingay, M., Barth, A., Reinecker, J., Kurfeß, D., & Müller, B. (2010). Global crustal stress pattern based on the World Stress Map database release 2008. Tectonophysics, 482(1-4), 3–15. doi:10.1016/j.tecto.2009.07.023.

Herrick C. G., and Haimson, B. C. (1994). *Modeling of episodic failure leading to borehole breakouts in Alabama limestone.* Paper presented at 1st North American Rock Mechanics Symposium, Austin, TX.

Hickman, S.H., Healey, J.H., Zoback, M.D. (1985) In situ stress, natural fracture distribution and borehole elongation in the Auburn geothermal well, Auburn, New York. J. Geophys. Res. 90, 5497-5512.

Hoek, E., Kaiser, P. K., and Bawden, W. F. (2000). *Support of underground excavations in hard rock.* London, UK: CRC Press.

Holcomb DJ, Rudnicki JW (2001) Inelastic constitutive properties and shear localization in Tennessee marble. Int. J. Numer. Analytical Methods Geomechanics. 25:109-129.

Horsrud, P., Bostrom, B., Sonstebo, E., and Holt R. (1998). *Interaction between shale and water-based drilling fluids: laboratory exposure tests give new insight into mechanisms and field consequences of KCl contents*. Paper presented at SPE Annual Technical Conference and Exhibition, New Oreans, LA.

Hunsche U, Albrecht H (1990) Results of True Triaxial Strength Tests on Rock Salt. Eng. Frac. Mech., 35:867-877.

Ibanez, W. D., and Kronenberg A. K. (1993). Experimental deformation of shale: Mechanical properties and microstructural indicators of mechanisms. *International Journal of Rock Mechanics and Mining Sciences & Geomechanics Abstracts, 30*(7), 723-734.

Idaho National Laboratory (2006) The Future of Geothermal Energy. Prepared under Idaho National Laboratory Subcontract No. 63 00019 for the U.S. Department of Energy, Assistant Secretary for Energy Efficiency and Renewable Energy, Office of Geothermal Technologies, Under DOE Idaho Operations Office Contract DE-AC07-05ID14517.

Ingraham MD, Issen KA, Holcomb DJ (2013), Response of Castlegate sandstone to true triaxial states of stress. J. Geophys. Res. Solid Earth. doi:10.1002/jgrb.50084.

Ingraham MD, Issen KA, Holcomb DJ (2013) Use of acoustic emissions to investigate localization in high-porosity sandstone subjected to true triaxial stresses. Acta Geotech. 8: 645-663.

Jaeger, J. C., Cook, N. G., and Zimmerman R. (2009). *Fundamentals of rock mechanics*, Hoboken, NJ: John Wiley.

JASON, The MITRE Corporation. (2014). *Subsurface Characterization Letter Report* (JSR-14-Task-013). McLean, VA.

Keranen, K. M., Weingarten, M., Abers, G. A., Bekins, B. A., and Ge, S. (2014). Sharp increase in central Oklahoma seimicity since 2008 induced by massive wastewater injection. *Science, 345*(6195), 448-451.

Kirsch, E. G. (1898). Die Theorie der Elastizit t und die Bed rfnisse der Festigkeitslehre. *Zeitshrift des Vereines deutscher Ingenieure 42*(1), 797-807.

Kocurek (2013). *Mancos Shale* (https://kocurekindustries.com/mancos-shale). Caldwell, TX: Kocurek Industries.

Kwasniewski M (2013) Mechanical behavior of rocks under true triaxial compression conditions – A review. In Kwasniewski M, Li X, Takahashi M (eds.) True Triaxial Testing of Rocks, CRC Press, London, pp. 99-131.

Labuz, J. F., and Biolzi L. (2007)., Experiments with rock: remarks on strength and stability issues. *International Journal of Rock Mechanics and Mining Sciences, 44*(4), 525-537.

Labuz, J. F., and Bridell J. (1993). Reducing frictional constraint in compression testing through lubrication. *International Journal of Rock Mechanics and Mining Sciences and Geomechanics, 30*(4), 451-455.

Labuz JF, Dai S-T, Papamichos E (1996) Plane-strain Compression of Rock-like Materials. Int. J. Rock Mech. Min. Sci. 33:573-584.

Lade, P.V., Inel, S. (1997) Rotational kinematic hardening model for sand. Part I. Concept of rotating yield and plastic potential surfaces. Comp. Geotechnics 21, 183-216.

Lee, H., Moon, T., and Haimson B. C. (2016). Borehole breakouts induced in arkosic sandstones and a discrete element analysis. *Rock Mechanics and Rock Engineering, 49*(4), 1369-1388.

Lee, M. Y., and Haimson, B. (1993). Laboratory study of borehole breakouts in Lac du Bonnet granite: a case of extensile failure mechanism. *International Journal of Rock Mechanics and Mining Sciences & Geomechanics Abstracts, 30*(7), 1039-1045.

Lee, M. Y., and Haimson, B. (1999). *Initial stress measurements in the Exploratory Studies Facility Yucca Mountaion, Nevada*. Paper presented at the 37th U.S. Symposium on Rock Mechanics, Vail, Colorado.

Lee H, Haimson BC (2011) True triaxial strength, deformability, and brittle failure of granodiorite from the San Andreas Fault Observatory at Depth. Int. J. Rock Mech. Min. Sci., 48:1199-1207.

Lisjak, A., Grasselli, G., and Vietor, T. (2014). Continuum-discontinuum analysis of failure mechanisms around unsupported circular excavations in anisotropic clay shales. *International Journal of Rock Mechanics and Mining Sciences, 65*(1), 96-115.

Ma X, Haimson BC (2016) Failure characteristics of two porous sandstones subjected to true triaxial stresses. J. Geophys. Res. Solid Earth, 121:6477-6498.

Ma X, Rudnicki JW, Haimson BC (2017) The application of a Matsuoka-Nakai-Lade-Duncan failure criterion to two porous sandstones. Int. J. Rock Mech. Min. Sci., 92:9-18.

Ma X, Rudnicki JW, Haimson BC (2017) Failure characteristics of two porous sandstones subjected to true triaxial stresses: Applied through a novel loading path. J. Geophys. Res. Solid Earth, doi:10.1002/2016JB013637.

Mares, V. M., and Kronenberg A. (1993). Experimental deformation of muscovite. *Journal of Structural Geology, 15*(9-10), 1061-1075.

Marschall, P., Distinguin, M., Shao, H., Bossart, P., Enachescu, C., and Trick T. (2006), *Creation and evolution of damage zones around a microtunnel in a claystone formation of the Swiss Jura Mountains* (SPE 98537). Paper presented at SPE International Symposium and Exhibition on Formation Damage Control, Lafayette, LA.

Martin, C. D., and Lanyon, G. W. (2003). Measurement of in-situ stress in weak rocks at Mont Terri Rock Laboratory, Switzerland. *International Journal of Rock Mechanics and Mining Sciences, 40*(7-8), 1077-1088.

Meier, T., Rybacki, E., Backers, T., and Dresen G. (2015.), Influence of bedding angle on borehole stability: a laboratory investigation of transverse isotropic oil shale. *Rock Mechanics and Rock Engineering, 48*(4), 1535-1546.

Melendez- Martinez, J., and Schmitt, D. R. (2016). A comparative study of the anisotropic dynamic and static elastic moduli of unconventional reservoir shales: Implication for geomechanical investigations. *Geophysics, 81*(3), D245-D261.

Michelis P (1987) True triaxial cyclic behavior of concrete and rock in compression. Int. J. Plasticity 3:249-270.

Mogi K (1967) Effect of the Intermediate Principal Stress on Rock Failure. J. Geophys. Res. 72:5117-5131.

Mogi K (1971) Effect of the triaxial stress system on the failure of dolomite and limestone. Tectonophys. 11:111-127.

Mogi K (1971) Fracture and flow of rocks under high triaxial compression. J. Geophys. Res. 76:1255-1269.

Mogi K (1972) Effect of the triaxial stress system on fracture and flow of rocks. Phys. Earth Planet. Interiors 5:318-324.

Mogi K (1981) Flow and fracture of rocks under general triaxial compression. App. Math Mech. 2:635-651.

Moos, D., Peska, P., and Zoback, M. D. (1998). *Predicting the stability of horizontal welss and multi-laterals – The role of in situ stress and rock properties.* Paper presented at SPE International Conference on Horizontal Well Technology, Calgary, Alberta, Canada.

Newell, P., Yoon, H., Martinez, M. J., Bishop, J. E., and Bryant, S. L. (2017). Investigation of the influence of geomechanical and hyrdogeological properties on surface uplift at In Salah. *Journal of Petroleum Science and Engineering, 155*(1), 34-45.

Niandou, H., Shao, J., Henry, J., and Fourmaintraux D. (1997). Laboratory investigation of the mechanical behaviour of Tournemire shale. *International Journal of Rock Mechanics and Mining Sciences, 34*(1), 3-16.

Okland, D., and Cook J. (1998). *Bedding-related borehole instability in high-angle wells* (SPE/ISRM 47285). Paper presented at SPE/ISRM Eurock Conference, Trondheim, Norway.

Ong, O. N., Schmitt, D. R., Kofman, R. S., and Haug, K. (2016). Static and dynamic pressure sensitivity anisotropy of a calcareous shale. *Geophysical Prospecting 64*(4), 875-897.

Pariseau, W. G. (1968). *Plasticity theory for anisotropic rocks and soil* (ARMA-68-0627). Paper presented at 10th U.S. Symposium on Rock Mechanics, Austin, TX.

Park, B.Y., 2014. Geomechanical Analysis to Predict the Oil Leak at the Wellbores in Big Hill Strategic Petroleum Reserve. SAND2014-0669, Sandia National Laboratories, Albuquerque, New Mexico.

Pelessone D. (1989) A modified formulation of the cap model Gulf Atomics Report GAC19579, prepared for the Defense Nuclear Agency under Contract DNA-001086-C-0277, January.

Peška, P., and Zoback M. D. (1995). Compressive and tensile failure of inclined well bores and determination of in situ stress and rock strength. *Journal of Geophysical Research, 100*(B7), 12791-12811.

Rawling, G. C., Baud, P., and Wong T. F. (2002). Dilatancy, brittle strength, and anisotropy of foliated rocks: Experimental deformation and micromechanical modeling. *Journal of Geophysical Research, 107*(B10), ETG 8-1 – 8-14.

Regueiro, R., Foster, C., Fossum, A., and Borja, R. (2004) Bifurcation analysis of a three invariant, isotropic/kinematic hardening cap plasticity model for geomaterials. ARMA/NARMS 04-520 paper prepared for GulfRocks 2004, 6th North American Rock Mechanics Symposium, Houston TX.

Reik G, Zacas M (1978) Strength and Deformation Characteristics of Jointed Media in True Triaxial Compression. Int. J. Rock Mech. Min. Sci. 15:295-303.

Roegiers, J. C. (2002). Well modeling: an overview. *Oil and Gas Science and Technology, 57*(5), 569-577.

Rudnicki JW, Rice JR (1975) Conditions for the localization of deformation in pressure sensitive dilatant materials. J. Mech. Phys. Solids. 23:371-394.

Rudnicki JW (2008) Failure of Rocks in the Laboratory and in the Earth. In: Proceedings of 22nd International Congress on Theoretical and Applied Mechanics. Adelaide; 24-29 August 2008. pp. 199-215.

Rudnicki, J.W. (2017) A three invariant model of failure in true triaxial tests on Castlegate sandstone. Int. J. Rock Mech Mining Sci. 97, 46-51.

Rutqvist, J., Birkholzer, J., Cappa F., and Tsang, C-F. (2007). Estimating maximum sustainable injection pressure during geological sequestration of CO_2 using coupled fluid flow and geomechanical fault-slip analysis. *Energy Conversion and Management, 48*(6), 1798-1807.

Salisbury, D., Ramos, G., and Wilton B. (1991). *Wellbore instability of shales using a downhole simulation test cell*. Paper presented at The 32nd US Symposium on Rock Mechanics (USRMS), Norman, OK.

Sandler, I.S., Pucik, T.A. (1994) Non-uniqueness in dynamic rate-independent non-associated plasticity, in G.Z. Voyiadjis, et al. (eds) Mechanics of Materials and Structures, Elsevier Science B.V., New York, 221-240.

Sandler, I.S. (2005) Review of the development of cap models for geomaterials. Shock and Vibration 12, 67-71.

Sarout, J., and Guegen, Y. (2008). Anisotropy of elastic wave velocities in deformed shales: Part 1 – Experimental results. *Geophsyics, 73*(5), D75-D89.

Sayers, C. M. (2013). The effect of anisotropy on the Young's modulus and Poisson's ratios of shales. *Geophysical Prospecting, 61*(2), 413-426.

Schindelin, J., Arganda-Carreras, I., Frise, E., Kaynig, V., Longair, M., Pietzsch, T., Preibisch, S., Rueden, C., Saalfeld, S., and Schmid B. (2012a)., Fiji: an open-source platform for biological-image analysis. *Nature Methods, 9*(7), 676-682.

Schneider, C. A., Rasband, W. S., and Eliceiri K. W. (2012b). NIH Image to ImageJ: 25 years of image analysis, *Nature Methods, 9*(7), 671-675.

Shamir, G., and Zoback M. D. (1992). Stress orientation profile to 3.5 km depth near the San Andreas fault at Cajon Pass, California. *Journal of Geophysical Research, 97*(B4), 5059-5080.

Shen, B. (2008) Borehole breakouts and in situ stresses. SHIRMS 2008 (y. Potvin, J. Carter, A. Dyskin, R. Jeffrey, eds), 12p.

Sibson, R. H. (1996). Structural permeability of fluid-driven fault-fracture meshes. *Journal of Structural Geology, 18*(8), 1031-1042.

SIERRA Solid Mechanics Team, 2010. Adagio 4.18 User's Guide. SAND2010-6313, Sandia National Laboratories, Albuquerque, New Mexico.

SIERRA Solid Mechanics Team, 2011. Sierra/Solid Mechanics 4.22 User's Guide. SAND2011-7597, Sandia National Laboratories, Albuquerque, New Mexico.

Simpson, J. P., Dearing H., and Salisbury D. (1989), Downhole Simulation Cell Shows Unexpected Effects of Shale Hydration on Borehole Wall. *SPE Drilling Engineering, 4*(01), 24-30.

Sone, H., and Zoback M. D. (2013). Mechanical properties of shale-gas reservoir rocks—Part 1: Static and dynamic elastic properties and anisotropy. *Geophysics, 78*(5), D381-D392.

Song, I., and Haimson B. C. (1997). Polyaxial strength criteria and their use in estimating in situ stress magnitudes from borehole breakout dimensions. *International Journal of Rock Mechanics and Mining Sciences, 34*(3-4), 1-16.

Sonstebo, E. F., and Holt R. M. (2001). *Brine exposure effects on a tertiary North Sea shale*. Paper presented at DC Rocks 2001, The 38th US Symposium on Rock Mechanics (USRMS), Washington, D.C.

Streit, J. E., and Hillis, R. R. (2004). Estimating fault stability and sustainable fluid pressures for underground storage of CO_2 in porous rock. *Energy, 29*(9-10), 1445-1456.

Takahashi M, Koide H (1989) Effect of the intermediate principal stress on strength and deformation behavior of sedimentary rocks at the depth shallower than 2000 m, In: Maury V and Fourmaintraux D (eds.) Rock at Great Depth Balkema, Rotterdam, pp. 19–26

Tapponnier P, Brace WF (1976) Development of Stress-Induced Microcracks in Westerly Granite. Int. J. Rock Mech. Min. Sci. 13:103-112.

Thury, M., and Bossart, P. (1999). The Mont Terri rock laboratory, a new international research project in a Mesozic shale formation, in Switzerland. *Engineering Geology, 52*(3-4), 347-359.

Tien, Y. M., and Kuo, M. C. (2001), A failure criterion for transversely isotropic rocks. . *International Journal of Rock Mechanics and Mining Sciences, 38*, 399-412

Ulm, F. J., Vandamme, M., Bobko, C., Alberto Ortega, J., Tai, K., and Ortiz, C. (2007). Statistical indentation techniques for hydrated nanocomposites: concrete, bone, and shale. *Journal of the American Ceramic Society, 90*(9), 2677-2692.

van den Hoek, P. J. (2001). *Prediction of different types of cavity failure using bifurcation theory.* Paper presented at DC Rocks 2001, The 38th U.S. Symposium on Rock Mechanics, Washinton, D.C.

van Oort, E., B. B. Hoxha, A. Hale, M. Aldin, and R. Patterson (2016), How to test fluids for shale compatibility, paper presented at Proceedings of the AADE Fluids Technical Conference and Exhibition, Houston, TX.

Vernik, L., and Zoback, M. D. (1989). *Effects of rock elastic and strength properties in estimation of the state of stress at depth.* Paper presented at The ISRM International Symposium, Pau, France.

Vernik, L., and Zoback, M. D. (1990). *Strength anisotropy in crystalline rock: Implications for assessment of in situ stresses from wellbore breakouts*. Paper presented at The 31th U.S. Symposium on Rock Mechanics, Golden, CO.

Vernik, L., and Zoback, M. D. (1992). Estimation of maximum horizontal principal stress magnitude from stress-induced well bore breakouts in the Cajon Pass Scientific Research borehole. *Journal of Geophysical Research, 97*(B4), 5109-5119.

Voigt, W. (1928). *Handbook of Crystal Physics*. Teubner, Leipzig.

Walsh, J. B., and Brace, W. F. (1964). A failure criterion for brittle anisotropic rock. *Journal of Geophysical Research, 69,* 3449-3456.

Warpinski, N. R., and Teufel, L. W. (1991). In situ stress measurements at Rainier Mesa, Nevada Test Site – influence of topography and lithology on the stress state in tuff. *International Journal of Rock Mechanics and Mining Sciences & Geomechanics Abstracts, 28*(2-3), 143-161.

Wawersik WR, Carlson LW, Holcomb DJ, Williams RJ (1997) New methods for true-triaxial rock testing, Int. J. Rock Mechanics Min. Sci. 34(3-4), 330-e1.

Willam, K.J. and Warnke, E.P., 1975. Constitutive model for the triaxial behavior of concrete, ISMES Seminar on Concrete Structures Subjected to Triaxial Stresses, Bergamo, Italy, p. 1-30.

Willson, S. M., Edwards, S. T., Crook, A., Bere, A., Moos, D., Peška, P., and Last, N. (2007). *Assuring stability in extended-reach wells – analyses, practices, and mitigation.* Paper presented at 2007 SPE/IADC Drilling Conference, Amsterdam, The Netherlands.

Yoon, H., Ingraham, M. D., Grigg, J., Rosandick, B., Rinehart, A., Mook, W. M., Dewers, T. A., and Mozley, P. (In Review). Impact of depositional and diagenetic hererogeneity on multiscale mechanical behavior of Mancos Shale, New Mexico and Utah, USA. In W. Camp, K. Milliken, K. Taylor, N. Fishman, P. Hackley, J. McQuaker (Eds), *Mudstone diagenesis: New research perspectives for shale hydrocarbons reservoirs, seals, and source rocks.* Tulsa, OK: American Association of Petroleum Geologists, in press.

Zhang L, Zhu H (2007) Three-dimensional Hoek-Brown strength criterion for rocks. J. Geotech. Geoenvir. Eng. 133:1128-1135.

Zhang, J., Bai, M., and Roegiers, J. C. (2006). On drilling directions for optimizing horizontal well stability using a dual-porosity poroelastic approach. *Journal of Petroleum Science and Engineering, 53*(1-2), 61-76.

Zheng, Z., Kemen, J., Cook, N. G. W. (1989). Analysis of borehole breakouts. *Journal of Geophysical Research 94*(B6), 7171-7182.

Zoback MD, Byerlee JD (1975) The effect of cyclic differential stress on dilatancy in westerly granite under uniaxial and triaxial conditions. J. Geophys. Res. 80:1526-1530.

Zoback, M. D. (2010). *Reservoir geomechanics,* Cambridge, UK: Cambridge University Press.

Zoback, M. D., and Haimson, B. C. (1983). Workshop on hydraulic fracturing stress measurements. *National Academy Press*, 44-54.

Zoback, M. D., Moos, D., Mastin, L., and Anderson, R. N. (1985). Well bore breakouts and in situ stress. *Journal of Geophysical Research, 90*(B7), 5523-5530.

APPENDIX 1: UNIVERSITY OF WISCONSIN TESTING REPORT

The document from Wisconsin was received in PDF format and is added to the final generated PDF file.

Reliability of Borehole Breakouts as a Method of In Situ Stress Measurement under Different Conditions of Stress and Temperature

(*a research project conducted for Sandia National Laboratories, by the University of Wisconsin-Madison, Bezalel Haimson, PI , Department of Materials Science and Engineering, and the Geological Engineering Program*)

Final report

Introduction

This project was initiated on April 1, 2016 and ends on July 31, 2018. The experimental stage of the project was completed on September 30, 2017. That was followed by post-test analysis, including thin section interpretation, and preparation of this final report.

The main objective of the project was to study the occurrence of drilling-induced borehole breakouts in the Sierra White granite, and assess their suitability for estimating the prevailing state of in situ stress in boreholes drilled in granite to depths reaching 3 km. To do so, a laboratory testing program was undertaken, consisting of drilling slim vertical boreholes in the center of pre-stressed cuboidal Sierra White granite specimens extracted from a quarry near Raymond, California. All test specimens came from a single block of the granite. Its uniaxial compressive strength (UCS) is 176.2 MPa, and its density is 2.64 g/cc. It has a grain size ranging from 0.5 to 10 mm. Its mineralogical composition is mainly comprised of oligoclase, quartz and orthoclase .

The state of the simulated in situ stress in the test specimens, before and during borehole drilling was varied between tests, but maintained roughly within a range characteristic of 3 km depth. Tested specimens were saw-cut along planes normal to borehole axis at about 10 mm intervals, creating thin quadratic discs, or slices. Representative slices from each specimen were sent to a specialized lab, where they were used for thin sections preparation. The location and dimensions of the breakouts were read on the thin sections using a petrographic microscope in the Sandia Laboratories.

Experimental Procedure: Drilling Simulated Wellbores in White Sierra Granite Blocks Subjected to True Triaxial Stresses

The unique advantage of the University of Wisconsin True-Triaxial Testing (UW-TTT) System, which accommodates cuboidal rock specimens of maximum size 150x150x230 cm^3 (Figure 1), is its ability to facilitate the drilling of a borehole into a test specimen subjected in advance to a general state of stress ($\sigma_1 \geq \sigma_2 \geq \sigma_3$). This simulates real field conditions, where rock formations are subjected to an in situ state of stress prior and during wellbore drilling.

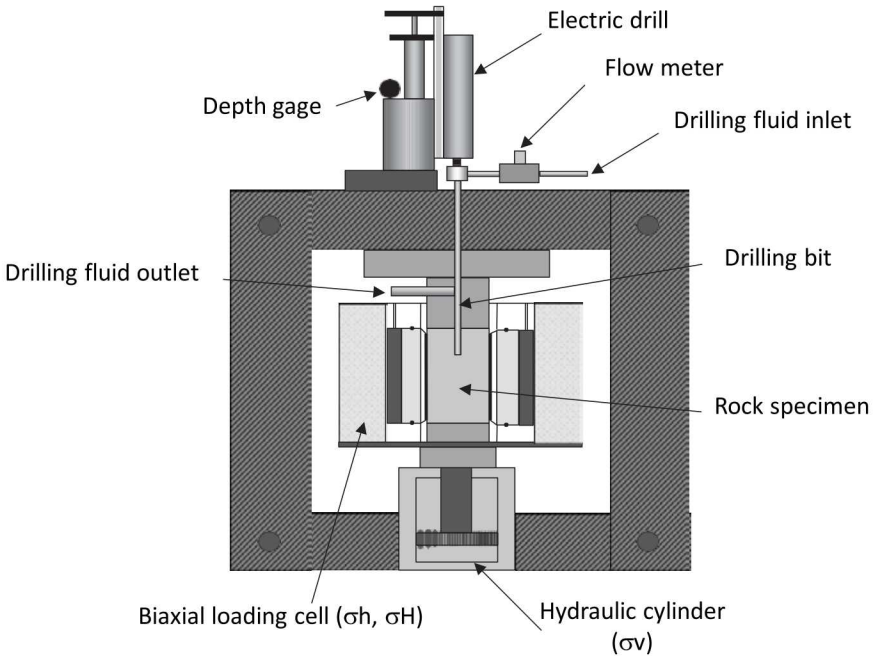

Figure 1. Borehole drilling into rock subjected to true triaxial stress condition in the UW-TTT system.

In the reported experiments, The UW-TTT System was used to apply a preset true triaxial state of stress to test specimens, prior to drilling the simulated wellbore. The System consists of a biaxial cell, which facilitates the application of horizontal loading (applying the principal stresses, σ_H and σ_h, to the specimen), seated inside a loading frame used for the application of the vertical stress (σ_v), and for the drilling of the simulated wellbore (Figure 1). The long axis of each block was aligned with the vertical direction. Thin copper shims, coated with a mixture of stearic acid and petroleum jelly, were placed between the specimen and the loading platens to reduce friction (Labuz and Bridell, 1993).

Test specimens were saw-cut from a single large White Sierra granite block, and then surface-ground to produce 13x13x18 cm^3 cuboids. Thirteen drilling tests (borehole radius: 13 mm) were conducted in the UW-TTT System, five at room temperature (25^{O}C), and eight at temperatures prevailing at about 3 km depth (87^{o}C). To increase the range of applied stresses capable of creating borehole breakouts in the Sierra White granite, a second suite of experiments was carried out on 10x13x18 cm^3 specimens, with a reduced area of the face subjected to σ_H. Eight room temperature (25^{O}C), and thirteen preheated (to 87^{o}C), tests were conducted using these specimens. The borehole radius in these tests was reduced to 11 mm, to maintain a similar ratio between the specimen nearest vertical face and the borehole radius.

All three principal stresses were increased at a constant rate of 0.1 MPa/s using three independent servo-controlled hydraulic lines. Once the prescribed level of the minimum horizontal principal stress (σ_h) was reached, it was held constant throughout the remainder of the test. The other two principal stresses were further increased until they reached the prescribed stress level for σ_v, at which time only the magnitude of σ_H continued to be raised to its preset level. Thereafter, the stresses were maintained constant during drilling of the simulated wellbore. In the reported series of tests the only general stress condition employed was one in which $\sigma_H > \sigma_v > \sigma_h$. The reason for that is two-fold: (a) a compilation of the variation of principal stresses with depth in the United States has shown that at a depth of 3 km the state of in situ stress would usually be one represented by $\sigma_H \geq \sigma_v > \sigma_h$, although at that depth σ_v is only slightly lower than σ_H (Haimson, 1978), (b) for the σ_h applied in our tests (30-50 MPa), no breakouts were formed in the White Sierra granite when the applied σ_H was equal or less than the vertical stress expected at 3 km depth (70-80 MPa). The minimum and maximum horizontal far-field principal stresses, (σ_h and σ_H) covered a range of ratios from 1:2.3 to as high as 1:6.7.

While maintaining constant the preset true triaxial loads on the specimen, a vertical borehole was drilled through the center of the specimen using the electric drill-rig mounted at top of the loading frame (Figure 1). The borehole was advanced at constant penetration rate of 0.01 cm/s, controlled manually by a potentiometer depth gage and a time-based drilling guide. Upon reaching the desired borehole depth (about 15 cm), the drill bit was retracted and the drilling fluid flow was turned off. Once drilling was completed, the specimen was kept under the same far-field stress conditions for an additional 20-30 min., to allow for the cessation of any delayed microcracking activity. Unloading proceeded at a rate similar to loading.

At the completion of each experiment, the tested specimen was removed from the biaxial cell. The specimen was dried overnight in an oven (40 – 50°C). When cooled, the drilled borehole was filled with thin epoxy in order to preserve the borehole condition. The specimen was then saw-cut into cross sectional slices, approximately 10 mm thickness, across the borehole axis. Critical slices were shipped to a specialized lab for the preparation of thin sections. These were then used to analyze breakout location and dimensions at borehole wall.

Thin Section Analysis of Breakout Parameters

Thin sections from tested specimens were scanned at 1200 dpi resolution using an HP Scanjet G4050 flatbed scanner. This image was used as a thin section map for observations. Observations and photomicrographs (1200 dpi resolution) at 4X magnified view on a Leitz Orthoplan petrographic microscope were used to define the geometry of each borehole breakout. Breakout span (θ) was defined as the angle encompassing the zone in which rock was absent from the original perimeter of the borehole with significant microfracture damage in the granite

(breakout). The radius of the borehole (r) was measured in Microsoft Powerpoint by overlaying the thin section image with lines that define each desired property. Placement of each line was guided by microscope observations. The angle that defines breakout span was measured using *ImageJ (*a public domain image-processing program developed at the National Institutes of Health). Radius of the borehole (r), breakout depth, and chord length of the breakout (c) (defined as the straight distance between the edges of breakout zone), were measured in Microsoft Powerpoint by overlaying the thin section image with lines that define each desired property. Placement of each line was guided by microscope observations. The angle that defines breakout span was measured using ImageJ (a Java-based image processing program developed at the National Institutes of Health.) The arc length of each breakout (s) was calculated from the breakout span and radius of the borehole. Accuracy of measurements is defined by the resolution of photomicrographs and scanned thin section maps, which allow linear measurements as small as 0.02 mm and angular measurements down to 0.01°. Tables 1 and 2 list the applied far-field principal stresses and the induced breakout spans in terms of location and deviation (dev.) from the expected 90° to the direction of σ_H.

Table 1. White Sierra granite far-field stresses, breakout spans, deviations in r=13 mm boreholes

Specimen	σh (MPa)	σv (MPa)	σH (MPa)	Temp (oC)	BktSpan1 (θb1) (angle)	BktSpan2 (θb2) (angle)	Dev of BktSpan1 from σH α1 (angle)	Dev of BktSpan2 from σH α2 (angle)	Ave. BktSpan θb (angle)
SGR2*[1]	35	60	90	25	–	–	–	–	
SGR3*[1]	50	60	120	25	–	–	–	–	
SGR17	40	70	160	25	27.32	18.53	-4	0	23
SGR6	50	80	160	25	48.96	35.56	-2	-3	42
SGR4	70	70	160	25	32.58	36.32	+5	+3	34
SGR14*[3]	30	70	140	87	28.43	-	+12	-	28
SGR19*[1]	40	70	140	87	-	-	-	-	
SGR10	30	70	150	87	32.31	-	+11	-	32
SGR13*[3]	50	70	150	87	42.43	32.70	-6	-14	38
SGR16	35	70	155	87	28.42	24.83	-3	+3	27
SGR18*[2]	50	70	155	87	-	-	-	-	
SGR11	30	70	160	87	32.37	27.33	-9	-2	30
SGR12	40	70	160	87	19.39	9.79	+6	+3	15

***[1] No thin section observations, only block samples observed to have no breakout**

***[2] No breakout visible in thin section**

***[3] Potential breakout visible in thin section**

Table 2. White Sierra granite far-field stresses, breakout spans, deviations in r=11mm boreholes

Specimen	σh (MPa)	σv (MPa)	σH (MPa)	Temp (°C)	BrktSpan1 θb1 (angle)	BrktSpan2 θb2 (angle)	Dev. of BktSpan1 from σH α1 (angle)	Dev. of BktSpan2 from σH α2 (angle)	Ave. BktSpan θb (angle)
SGR9	30	70	150	25	27	-	+11	-	27
SGR8	30	70	160	25	15	-	+4	-	15
SGR7	40	70	160	25	34	-	+1	-	34
SGR30*[2]	40	80	160	25	-	-	-	-	
SGR21*[3]	60	80	180	25	20	-	-4	-	20
SGR31	40	80	200	25	33	36	+2	-2	34
SGR20	48	80	200	25	20	18	+2	-7	19
SGR22*[3]	60	80	200	25	12	9	+3	+9	10.5
SGR15*[3]	30	70	120	87	38	-	+3	-	38
SGR29*[2]	30	80	180	87	-	-	-	-	
SGR25*[2]	60	80	180	87	-	-	-	-	
SGR27*[3]	40	80	185	87	19	-	-8	19	19
SGR34	30	80	190	87	25	-	+3	-	25
SGR35	35	80	190	87	15	-	+4	-	15
SGR33	30	80	200	87	21	22	+3	+6	22
SGR32*[3]	35	70	200	87	42	47	-6	-1	44.5
SGR26*[3]	40	80	200	87	23	-	-3	-	23
SGR28*[3]	40	80	200	87	21	-	+4	-	21
SGR36	45	80	200	87	21		-1	-	20.5
SGR24*[3]	50	80	200	87	29	-	-4	-	29
SGR23*[3]	60	80	200	87	38	-	-1	-	38

***[1] No thin section observations, only block samples observed to have no breakout**

***[2] No breakout visible in thin section**

***[3] Potential breakout visible in thin section**

Tables 1 and 2 represent the two sets of breakout producing tests in the White Sierra granite, one leading to boreholes of 13 mm radius, and the other to boreholes of 11 mm radius. Two immediate observations are: (1) within the limited scope of our testing program, no noticeable difference was observed between results of tests conducted at 25°C and those at the elevated temperature of 87°C, and (2) in the smaller radius boreholes, fewer than 50% of the tests resulted in two diametrically opposed breakouts. In the other tests no breakout, or only one breakout, developed. However, because in tests resulting in two breakouts, their spans were nearly equal and diametrically opposed, the assumption was made that the single span was a good approximation of the average span in the two-breakout test specimens. In order to distinguish the single span from the average of two spans, it was preceded by a tilde (~) in the column titled 'Ave BrktSpan'. Appendices A and B show images of the actual thin sections, showing cross sections of the borehole wall and the breakouts recorded.

Relating Breakout Spans to the Far-Field Stresses

In a vertical borehole drilled in a practically homogeneous, linear and isotropic elastic rock, such as granite, for which the vertical stress is a principal stress, the state of stress a the point of borehole-breakout intersection (point A or A' in Figure 2) in terms of the local radial, tangential, and vertical stresses, can be expressed as:

$$\sigma_{rr} = 0$$
$$\sigma_{\theta\theta} = -\sigma_H + \sigma_h - 2(\sigma_H - \sigma_h)\cos 2\propto_A$$
$$\sigma_{zz} = \sigma_v - 2\upsilon(\sigma_H - \sigma_h)\cos 2\propto_A \qquad (1)$$

where $\propto_A$ is the angular coordinate of point A, measured from the direction of σ_H, and υ is the Poisson's ratio. In terms of the measured borehole breakout span angle, θ_b, equation (1) becomes:

$$\sigma_{rr} = 0$$
$$\sigma_{\theta\theta} = -\sigma_H + \sigma_h - 2(\sigma_H - \sigma_h)\cos(180 - \theta_b)$$
$$\sigma_{zz} = \sigma_v - 2\upsilon(\sigma_H - \sigma_h)\cos(180 - \theta_b) \qquad (1a)$$

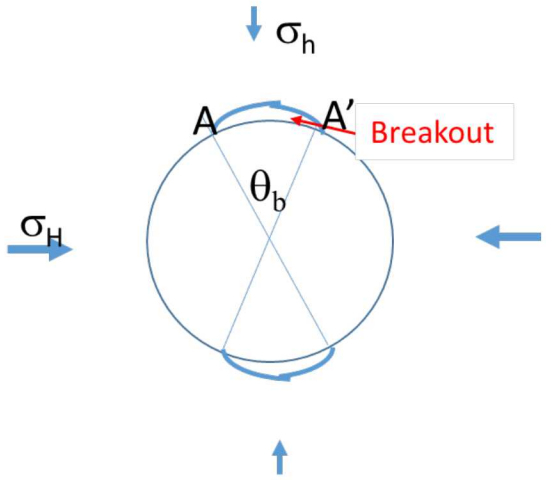

Figure 2. Cross-section of a vertical wellbore, showing two diametrically opposed breakouts and their span (θ_b).

At the point of borehole-breakout intersection, the state of stress is assumed to be in limit equilibrium, i.e. where the stress condition is that required to bring about failure, i.e. where the appropriate criterion of failure is met.

Since the state of stress at borehole-breakout intersection is true triaxial, in which the intermediate principal stress (σ_2) cannot be neglected, the 2D Mohr-Coulomb criterion of failure, which ignores σ_2, is not applicable. Hence, the failure criterion invoked was the one introduced by Mogi (1971, 2007), represented by:

$$\tau_{oct} = f[(\sigma_1 + \sigma_3)/2], \qquad (2)$$

where τ_{oct} (octahedral shear stress)= $1/3[(\sigma_1-\sigma_2)^2+(\sigma_2-\sigma_3)^2+(\sigma_3-\sigma_1)^2]^{1/2}$.

Mogi's failure criterion for White Sierra granite (SGR) was found to be (Ingraham, 2018):

$$\tau_{oct} = 0.7278(\sigma_1+\sigma_3)/2 + 13.605 \qquad R^{\wedge 2} = 0.983 \qquad (3)$$

Tables 3 (r=13 mm) and 4 (r = 11 mm) list the results of the tests conducted at UW-Madison, in the form of the applied far-field principal stresses, the average breakout span, the calculated principal stresses at borehole-breakout wall intersection, and the predicted failure stress based on Mogi's failure criterion.

Figures 3, 4, and 5 depict the variation of the Octahedral Shear Stress with Mogi's Effective Mean Stress for simulated wellbores of radius r= 13 mm, r=11 mm, and for combined r=11 mm and r=13 mm, respectively, based on our breakout tests. They are plotted on top of Mogi's failure criterion applied to true triaxial tests conducted at Sandia Labs (Ingraham et al., 2018). The plots show a near coincidence with the trend of the triaxial test results. One suspected reason for the minor discrepancies is the fact that the triaxial tests were conducted at one lab (Sandia National Labs), and the borehole drilling tests at another (UW-Madison).

Table3. White Sierra granite far-field stresses, breakout span and Mogi failure criterion in r=13 mm boreholes

Specimen	σh	σv	σH	Temp	Ave. BktSpan θb	σθθ	σrr	σzz	Predicted Failure Stress Per Mogi
	(MPa)	(MPa)	(MPa)	(oC)	(angle)	(MPa)	(MPa)	(MPa)	(MPa)
SGR2*[1]	35	60	90	25		235.00	0	60.00	59.0925
SGR3*[1]	50	60	120	25		310.00	0	60.00	75.468
SGR17	40	70	160	25	23	34.00	0	70.00	86.385
SGR6	50	80	160	25	42	373.49	0	80.00	90.024
SGR4	70	70	160	25	34	379.23	0	70.00	97.302
SGR14	30	70	140	87	28	364.25	0	70.00	75.468
SGR19*[1]	40	70	140	87		380.00	0	70.00	79.107
SGR10	30	70	150	87	32	383.53	0	70.00	79.107
SGR13*[3]	50	70	150	87	38	357.60	0	70.00	86.385
SGR16	35	70	155	87	27	403.84	0	70.00	82.746
SGR18*[2]	50	70	155	87		415.00	0	70.00	88.2045
SGR11	30	70	160	87	30	415.17	0	70.00	82.746
SGR12	40	70	160	87	15	431.82	0	70.00	86.385

***[1] No thin section observations, only block samples observed to have no breakout**

***[2] No breakout visible in thin section**

***[3] Potential breakout visible in thin section**

Table 4. White Sierra granite far-field stresses, breakout span, Mogi failure criterion in r=11 mm boreholes

Specimen	σh (MPa)	σv (MPa)	σH (MPa)	Temp (°C)	Ave Brkt Span θb (angle)	σθθ (MPa)	σrr (MPa)	σzz (MPa)	Predicted Failure Stress Per Mogi (MPa)
SGR9	30	70	150	25	27	393.84	0	70.00	79.107
SGR8	30	70	160	25	15	441.14	0	70.00	82.746
SGR7	40	70	160	25	34	398.97	0	70.00	86.385
SGR30*[2]	40	80	160	25		440.00	0	80.00	86.385
SGR21*[3]	60	80	180	25	20	465.53	0	80.00	100.941
SGR31	40	80	200	25	34	505.29	0	80.00	100.941
SGR20	48	80	200	25	19	535.44	0	80.00	103.8522
SGR22*[3]	60	80	200	25	10.5	535.31	0	80.00	108.219
SGR15*[3]	30	70	120	87	38	291.84	0	70.00	68.19
SGR29*[2]	30	80	180	87		510.00	0	80.00	90.024
SGR25*[2]	60	80	180	87		480.00	0	80.00	100.941
SGR27*[3]	40	80	185	87	19	499.20	0	80.00	95.4825
SGR34	30	80	190	87	25	510.02	0	80.00	93.663
SGR35	35	80	190	87	15	524.44	0	80.00	95.4825
SGR33	30	80	200	87	22	545.24	0	80.00	97.302
SGR32*[3]	35	70	200	87	44.5	470.37	0	70.00	99.1215
SGR26*[3]	40	80	200	87	23	534.56	0	80.00	100.941
SGR28*[3]	40	80	200	87	21	538.75	0	80.00	100.941
SGR36	45	80	200	87	20.5	535.37	0	80.00	102.7605
SGR24*[3]	50	80	200	87	29	512.39	0	80.00	104.58
SGR23*[3]	60	80	200	87	38	480.64	0	80.00	108.219

***[1] No thin section observations, only block samples observed to have no breakout**

***[2] No breakout visible in thin section**

***[3] Potential breakout visible in thin section**

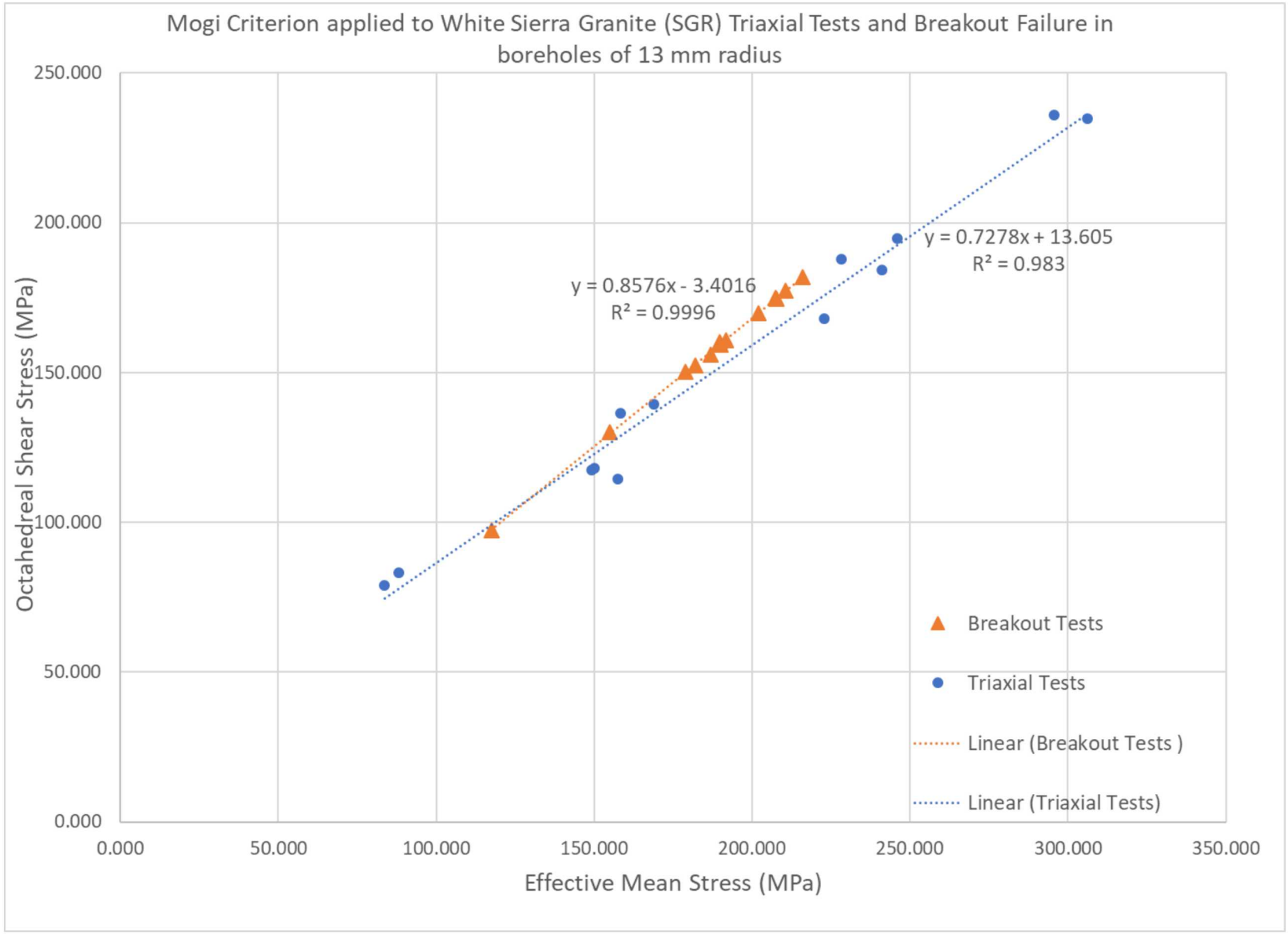

Figure *3*. Mogi Criterion applied to White Sierra Granite Triaxial Tests and Breakout Failure in boreholes of 13 mm radius

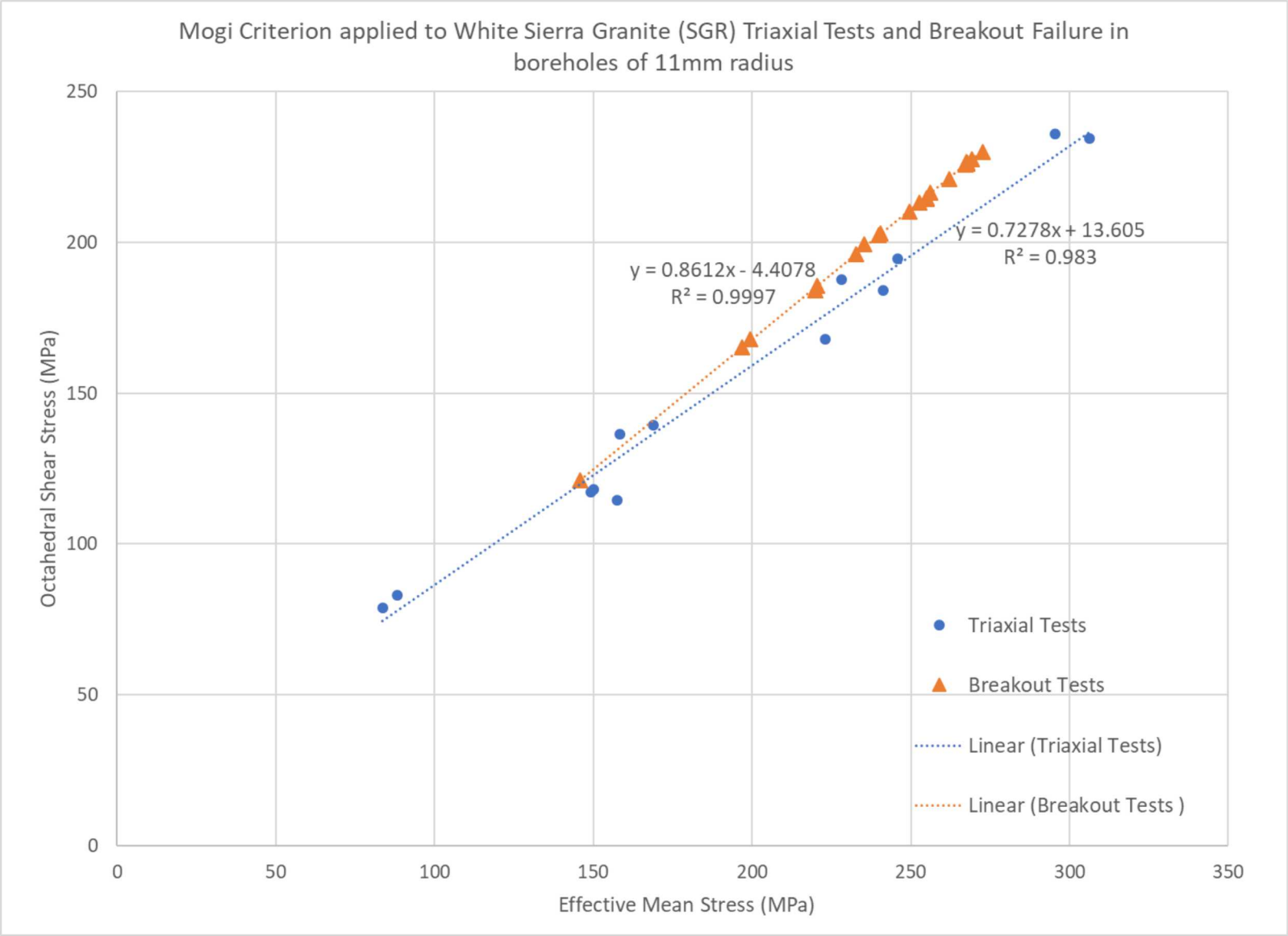

Figure 4. Mogi Criterion applied to White Sierra Granite Triaxial Tests and Breakout Failure in boreholes of 11mm radius

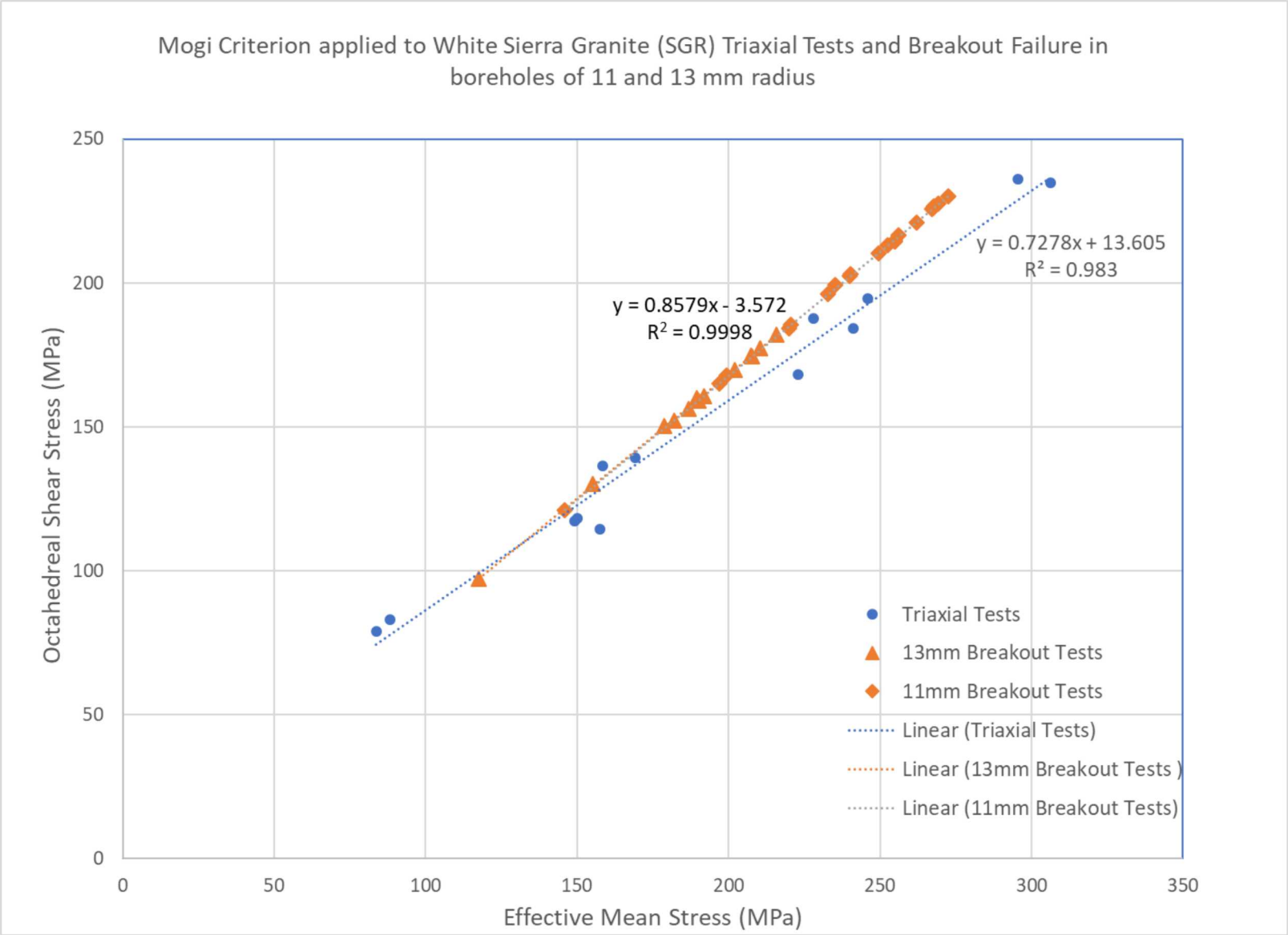

Figure 5. Mogi Criterion applied to White Sierra Granite Triaxial Tests and Breakout Failure in boreholes of 11mm and 13 mm radius.

What can we learn about the local state of stress from borehole beakouts?

Following the observation that the octahedral shear stress versus the effective mean stress at the intersection of breakout and borehole wall is well represented by the plot of the the octahedral shear stress versus the effective mean stress upon failure in triaxial tests conducted on the same rock (with minor discrepancies, probably owing to the two series of tests having been conducted in two separate labs), an equation is obtained in terms of the two principal horizontal far-field stresses, σ_H and σ_h. In the case of the tested White Sierra granite, in which we combine both the 11 mm and the 13 mm drilled boreholes (Figure 5) the equation becomes:

$$\tau_{oct} = 0.8579(\sigma_H+\sigma_h)/2 - 3.572 \quad (4)$$

where $\tau_{oct} = 1/3[(\sigma_H-\sigma_v)^2+(\sigma_v-\sigma_h)^2+(\sigma_h-\sigma_H)^2]^{1/2}$.

The vertical stress, σ_v, can often be approximated from the depth of the borehole and the density of the rock, so the only unknowns are the two principal horizontal stresses. There are several ways by which an additional independent equation is obtained. One is to conduct a hydraulic fractuiring test, and use the results to identify the minimum horizontal principal stess, σ_h, so that equation (4) can be solved. Another approach was recently suggested by Song and Chang (RMREJ, 2018) who used a stochastic method to solve equation (4), even when neither σ_H, nor σ_h is known.

Conclusions

We conducted a series of laboratory drilling tests in (10 or 13)x13x18 cm^3 cuboidal specimens of White Sierra granite, mostly at 87°C, to simulate conditions at 3 km depth. We subjected the granite to a variety of true triaxial stresses, within the range typically encountered at 3 km depth, in which σ_v is the intermediate principal stress. Test results point to a close approximation between Mogi failure criterion for the granite subjected to a series of triaxial compressive stresses, and that for a breakout intersecting the borehole wall. The coincidence between Mogi criterion for triaxial tests and that required for breakout initiation, renders one equation in two unknown principal stresses, σ_H and σ_h. In order to identify the two principal stresses, an additional equation is required, and that can be obtained in different ways, such as a hydraulic fracturing test in the borehole, rendering σ_h (the minimum principal horizontal stress), or the use of a stochastic approach (Song and Chang, 2018).

Appendix A. Images of thin sections showing cross-sections of borehole walls (radius=13 mm) and initiated breakouts.

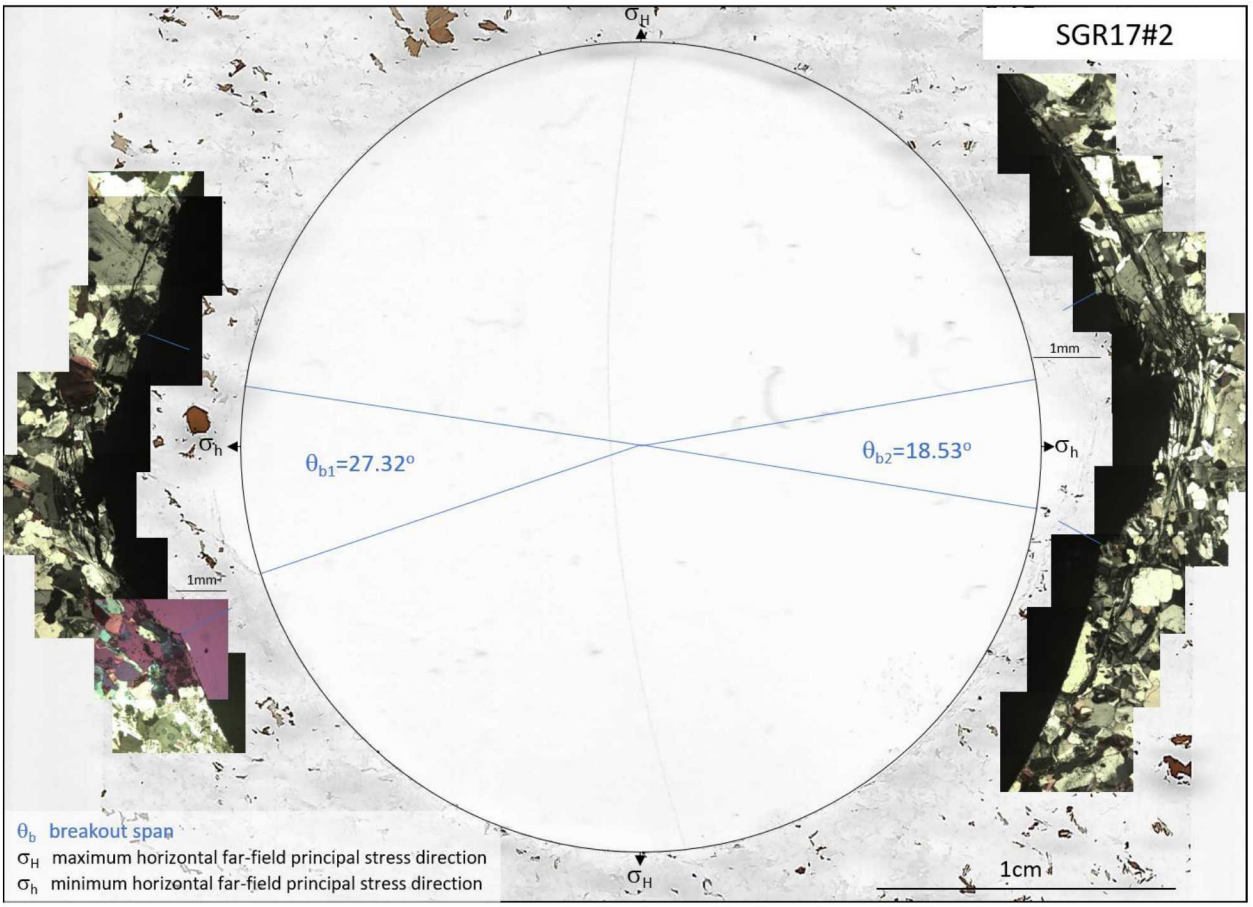
SGR17#2
σ_H
σ_h
θ_{b1}=27.32°
θ_{b2}=18.53°
1mm
1mm
1cm
θ_b breakout span
σ_H maximum horizontal far-field principal stress direction
σ_h minimum horizontal far-field principal stress direction

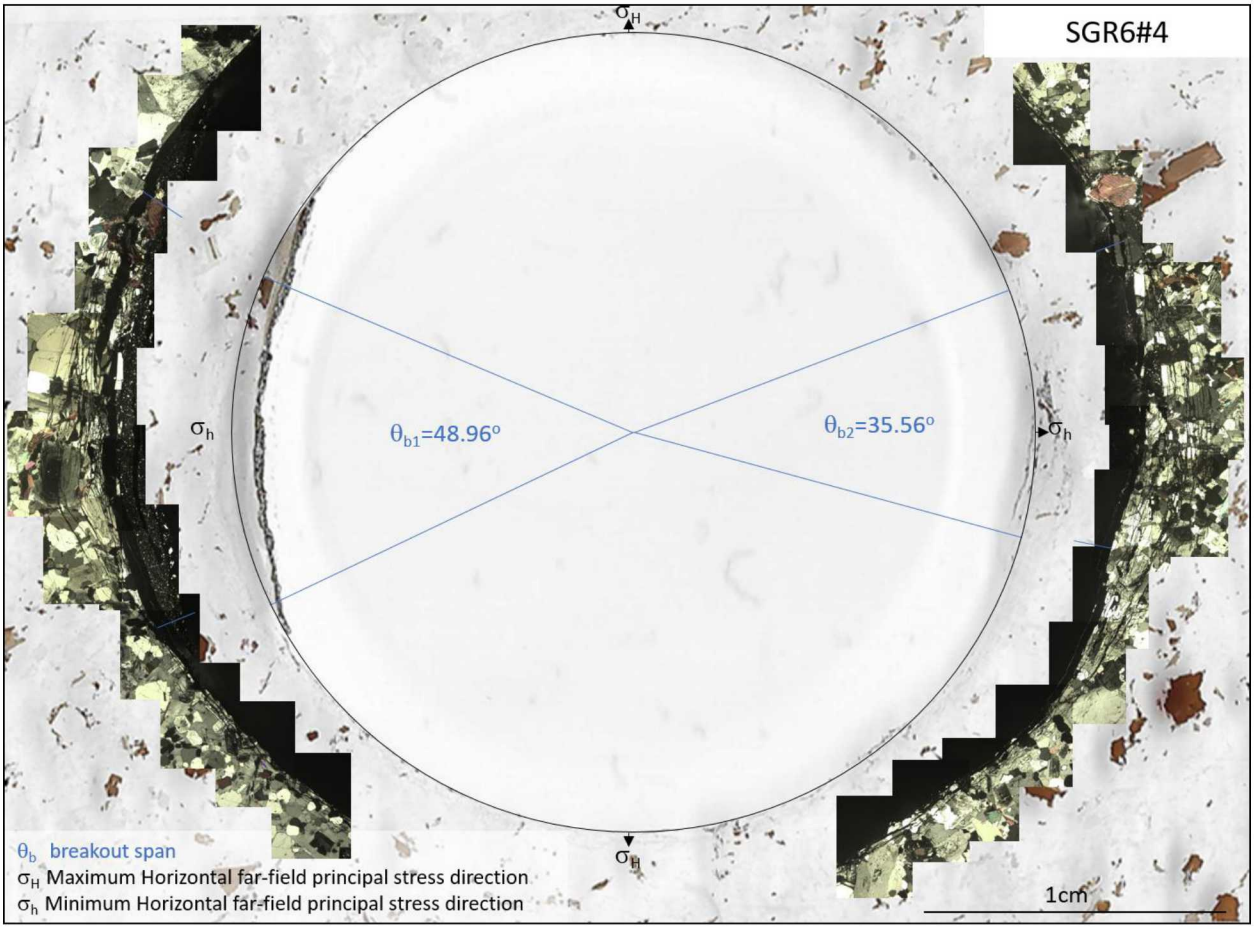
SGR6#4
σ_H
σ_h
θ_{b1}=48.96°
θ_{b2}=35.56°
1cm
θ_b breakout span
σ_H Maximum Horizontal far-field principal stress direction
σ_h Minimum Horizontal far-field principal stress direction

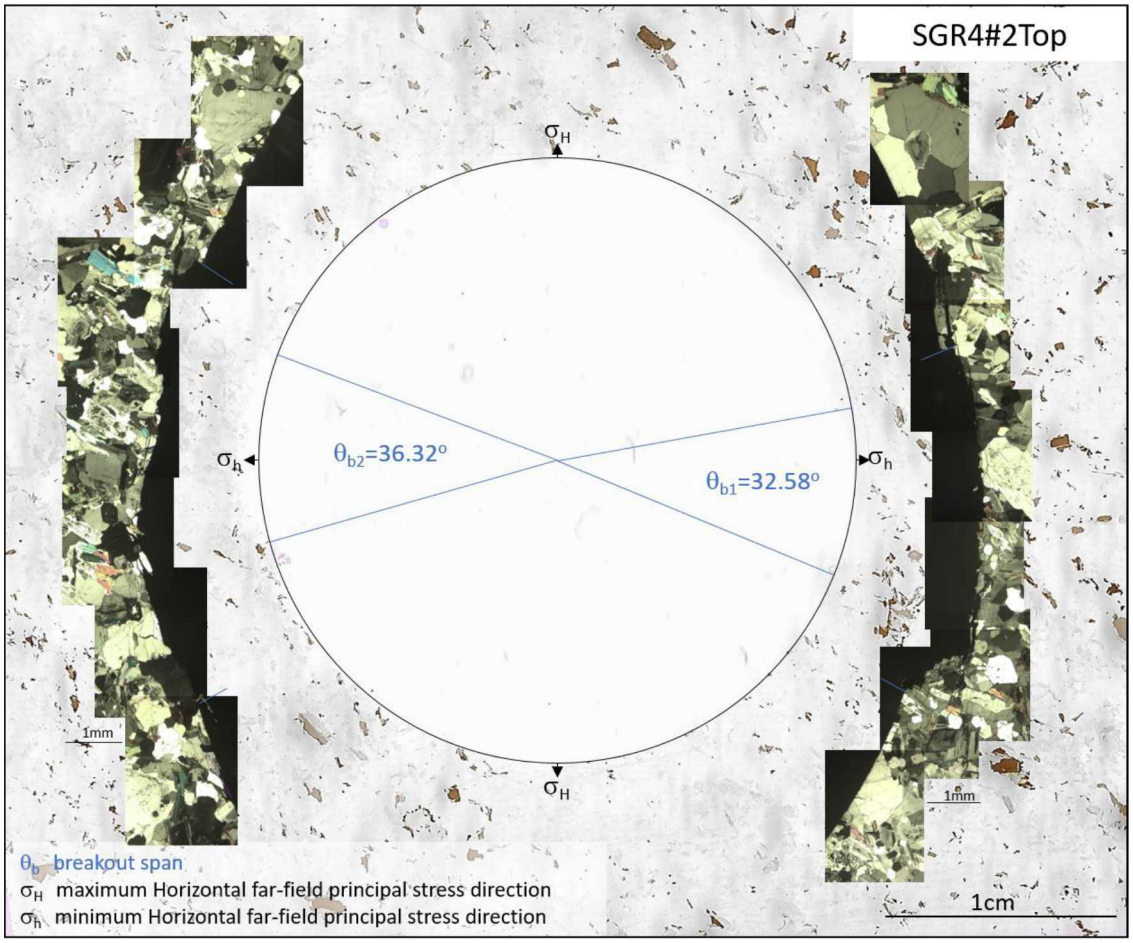
SGR4#2Top
σ_H
σ_h
θ_{b2}=36.32°
θ_{b1}=32.58°
σ_h
σ_H
1mm
1mm
1cm
θ_b breakout span
σ_H maximum Horizontal far-field principal stress direction
σ_h minimum Horizontal far-field principal stress direction

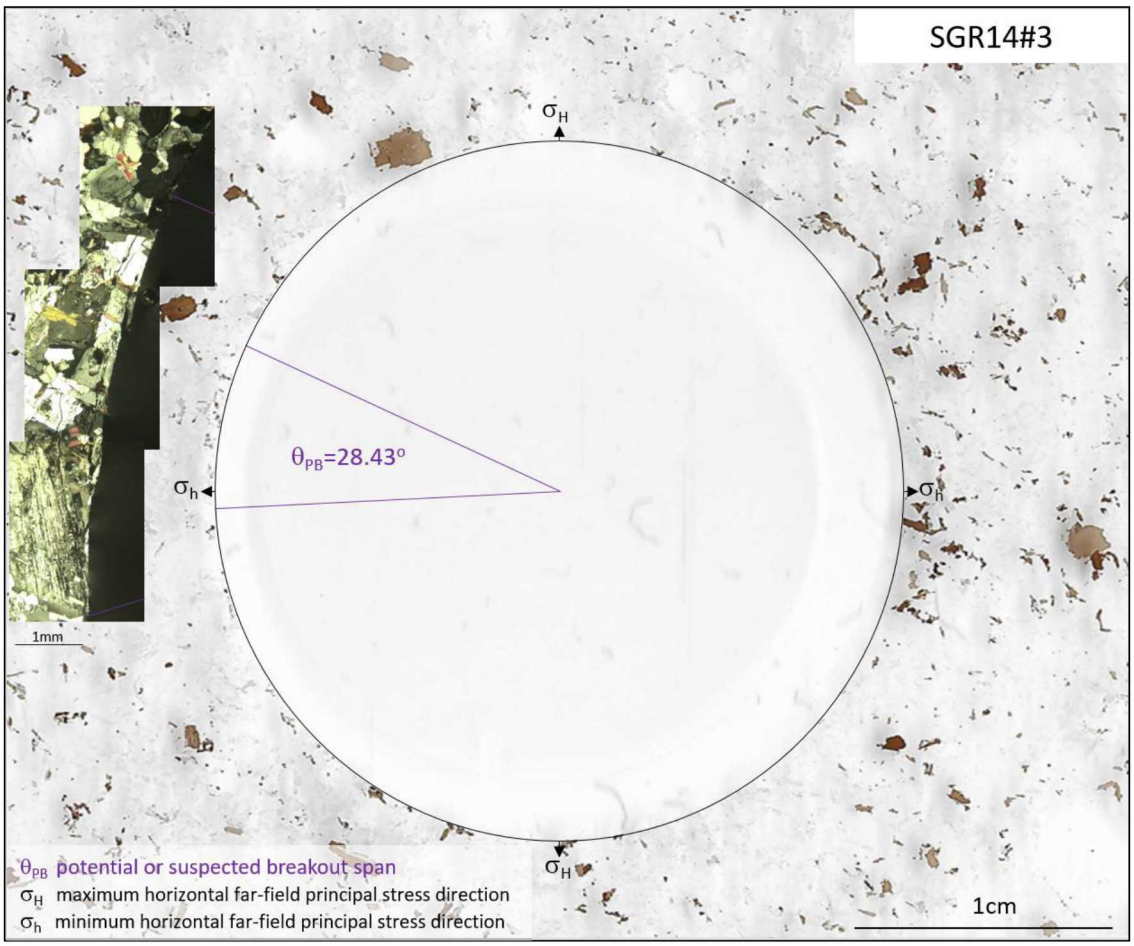
SGR14#3
σ_H
θ_{PB}=28.43°
σ_h
σ_h
σ_H
1mm
1cm
θ_{PB} potential or suspected breakout span
σ_H maximum horizontal far-field principal stress direction
σ_h minimum horizontal far-field principal stress direction

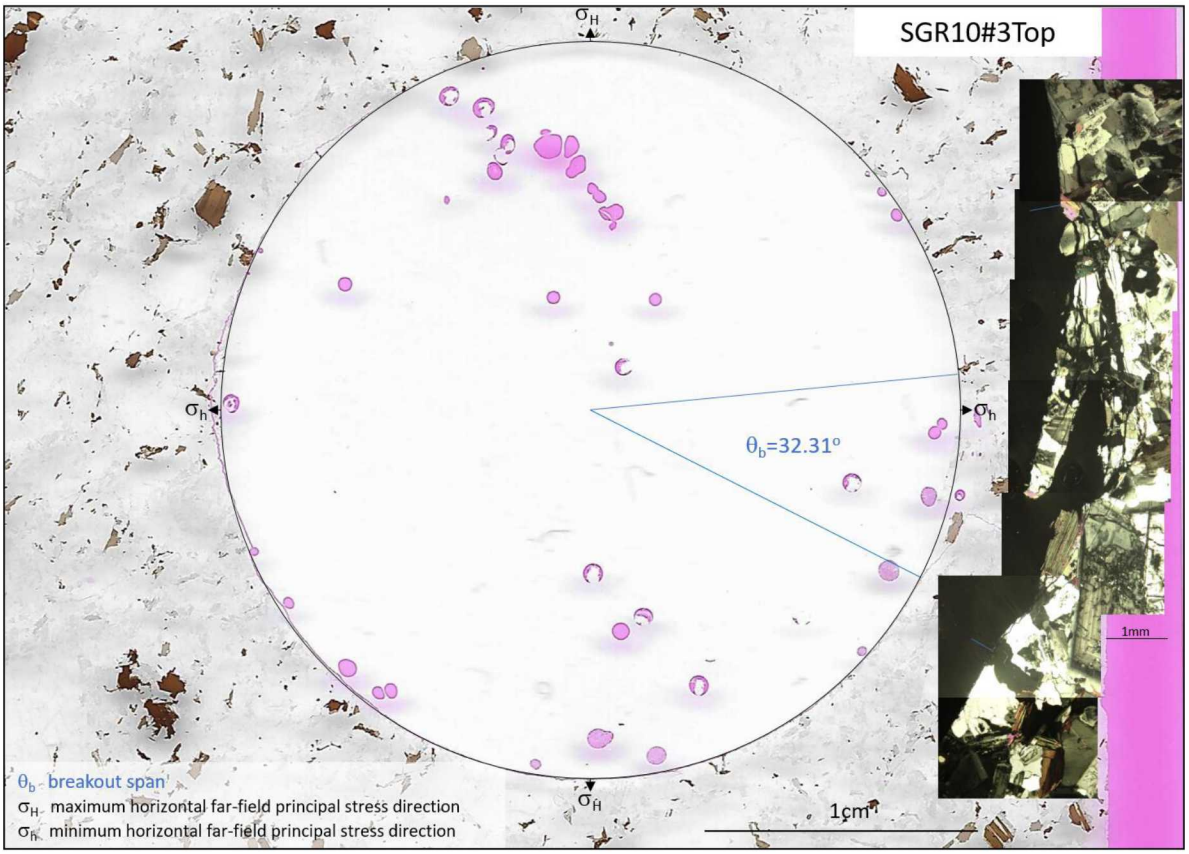
SGR10#3Top
σ_H
σ_h
θ_b=32.31°
1mm
1cm
θ_b - breakout span
σ_H maximum horizontal far-field principal stress direction
σ_h minimum horizontal far-field principal stress direction

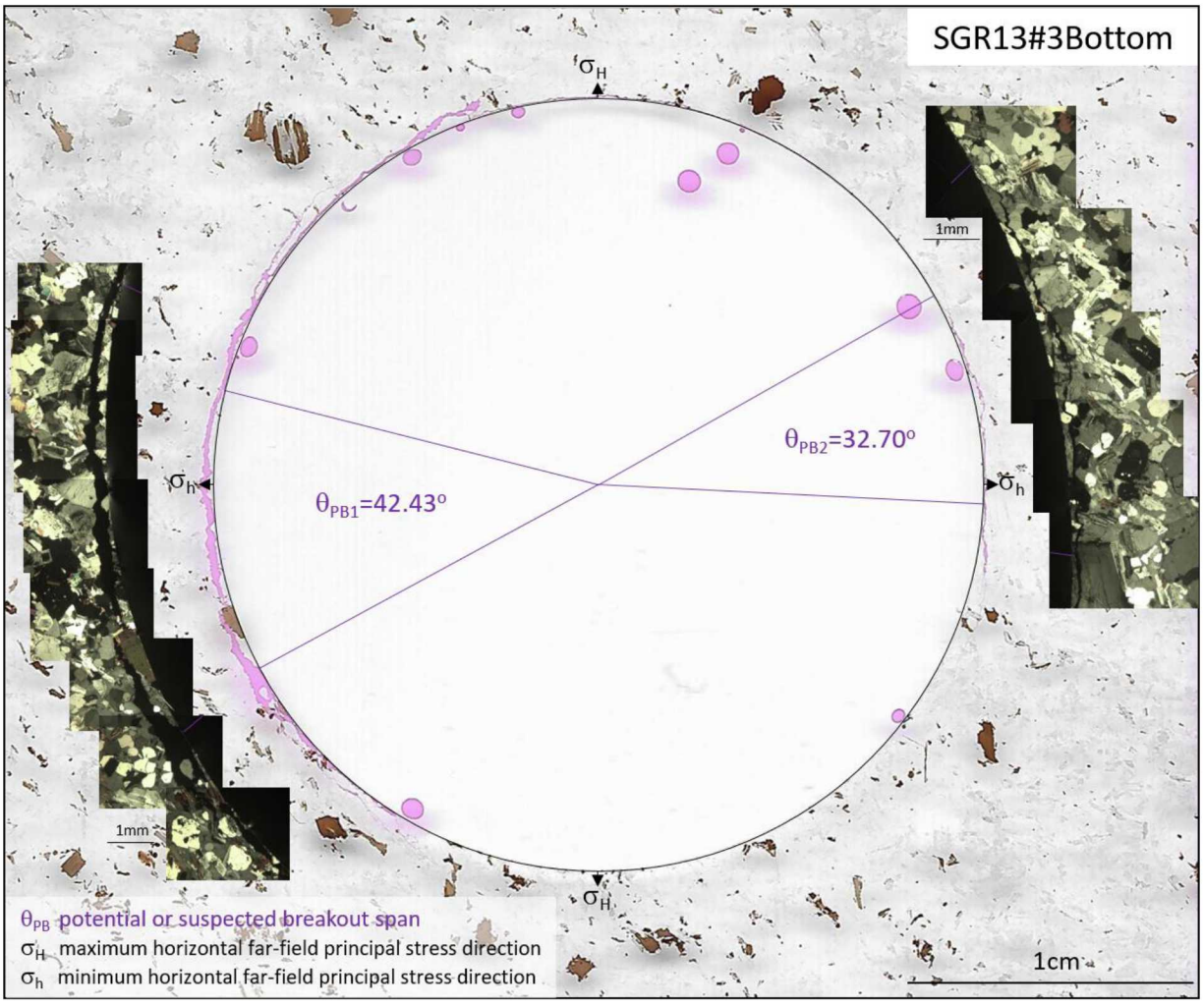
SGR13#3Bottom
σ_H
σ_h
θ_{PB1}=42.43°
θ_{PB2}=32.70°
1mm
1mm
1cm
θ_{PB} potential or suspected breakout span
σ_H maximum horizontal far-field principal stress direction
σ_h minimum horizontal far-field principal stress direction

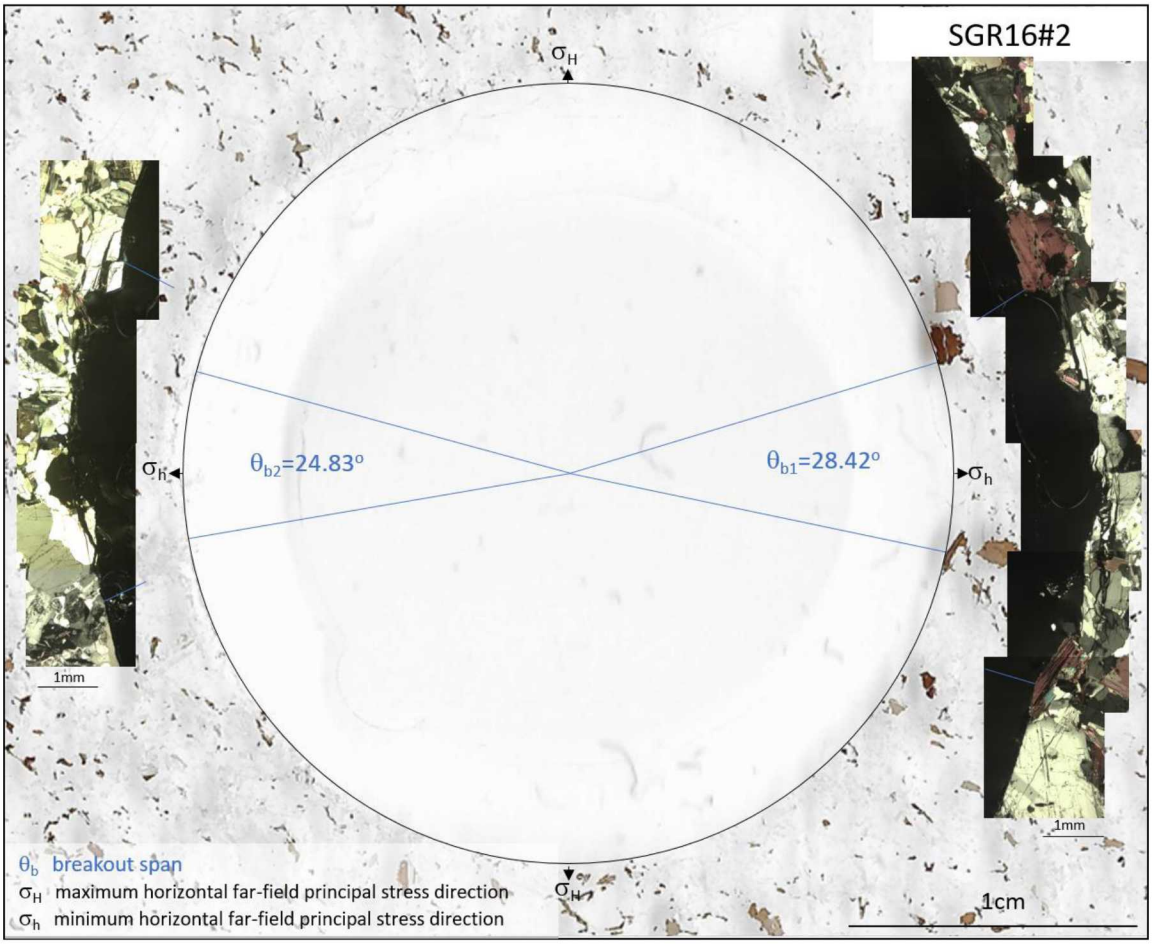
SGR16#2
σ_H
σ_h
θ_{b2}=24.83°
θ_{b1}=28.42°
1mm
1mm
1cm
θ_b breakout span
σ_H maximum horizontal far-field principal stress direction
σ_h minimum horizontal far-field principal stress direction


SGR18#4
σ_H
σ_h
σ_h
σ_H
σ_H maximum horizontal far-field principal stress direction
σ_h minimum horizontal far-field principal stress direction
1cm

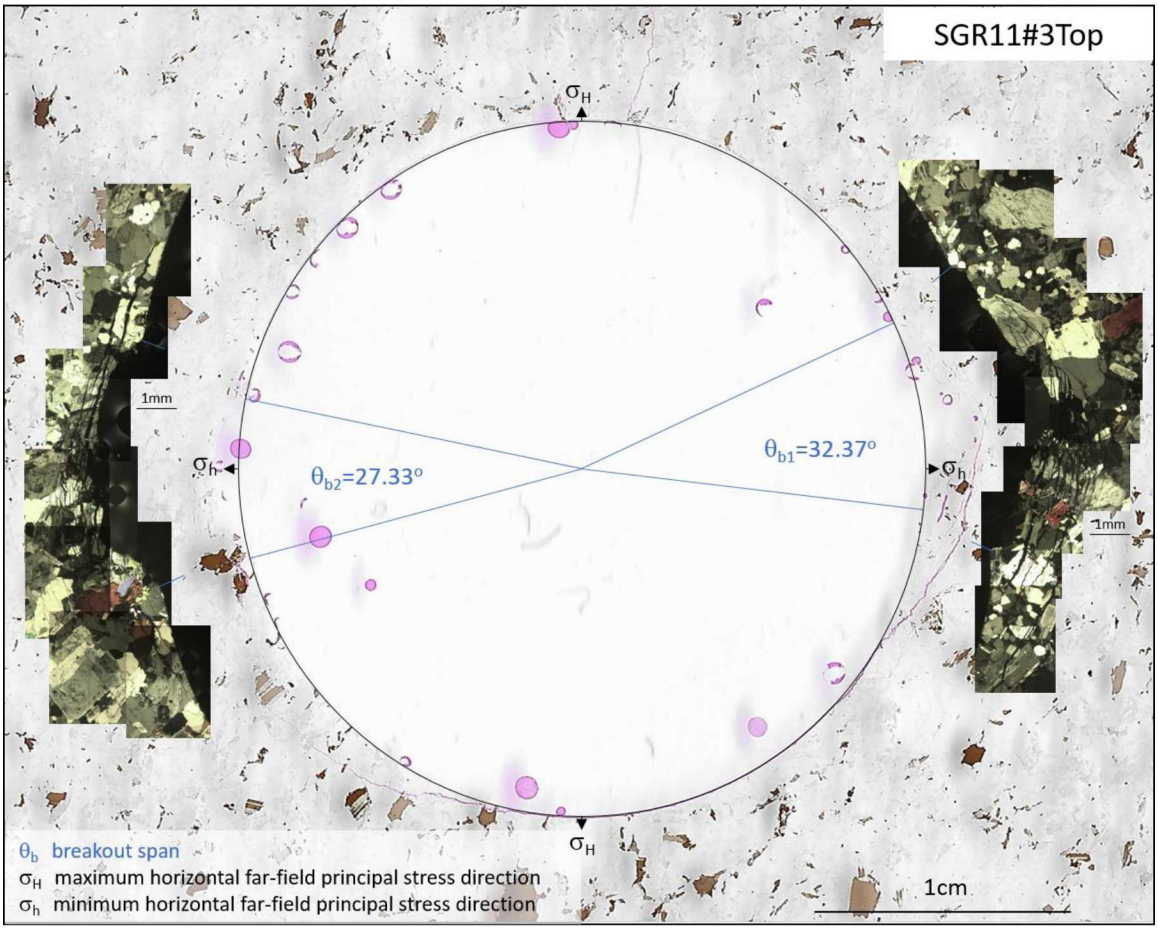
SGR11#3Top
σH
σh
θb1=32.37°
θb2=27.33°
1mm
1mm
1cm
θb breakout span
σH maximum horizontal far-field principal stress direction
σh minimum horizontal far-field principal stress direction

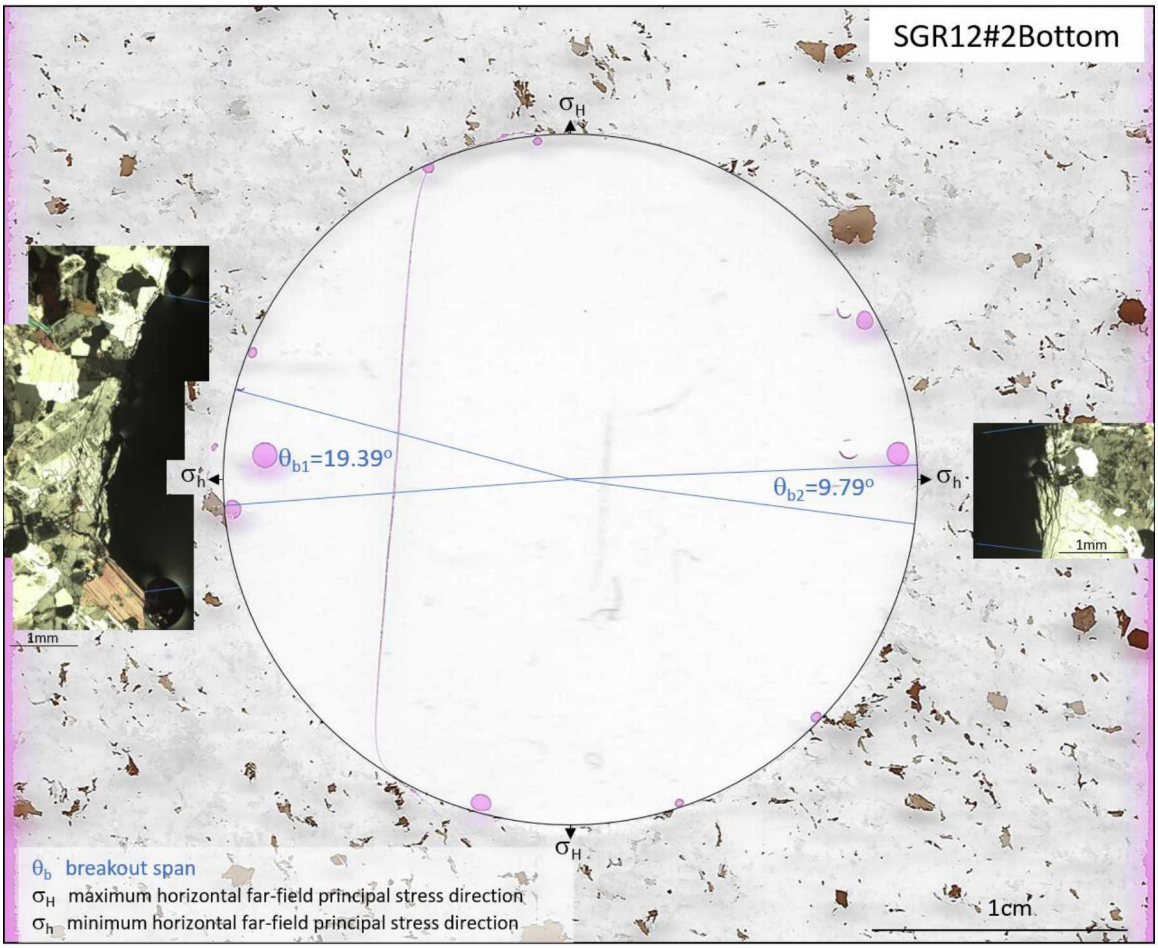
SGR12#2Bottom
σH
σh
θb1=19.39°
θb2=9.79°
1mm
1mm
1cm
θb breakout span
σH maximum horizontal far-field principal stress direction
σh minimum horizontal far-field principal stress direction

Appendix B. Images of thin sections showing cross-sections of borehole walls (radius=11 mm) and initiated breakouts.

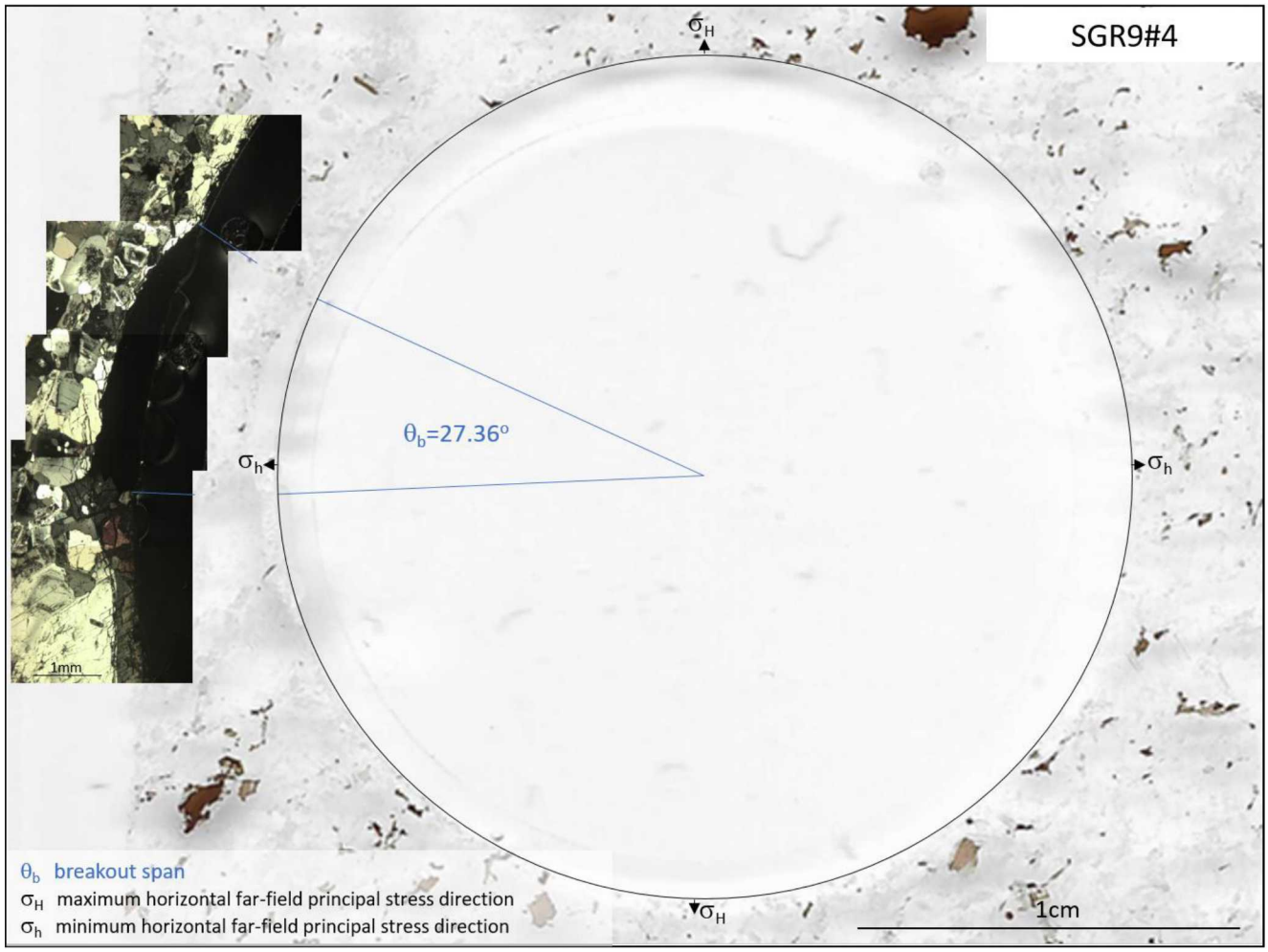
SGR9#4
σH
σh
σh
σH
θb=27.36°
1mm
1cm
θb breakout span
σH maximum horizontal far-field principal stress direction
σh minimum horizontal far-field principal stress direction

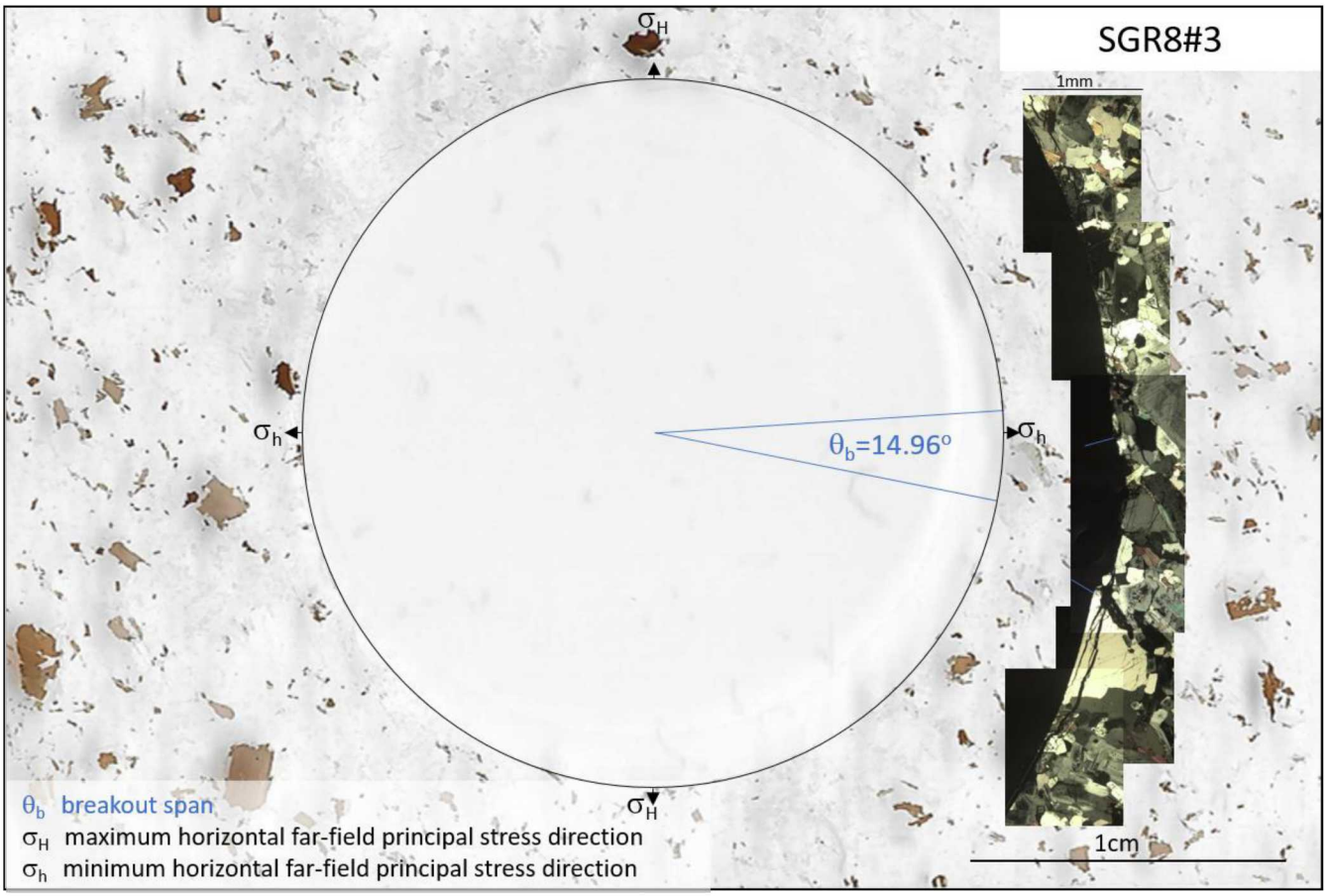
SGR8#3
σH
σh
σh
σH
θb=14.96°
1mm
1cm
θb breakout span
σH maximum horizontal far-field principal stress direction
σh minimum horizontal far-field principal stress direction

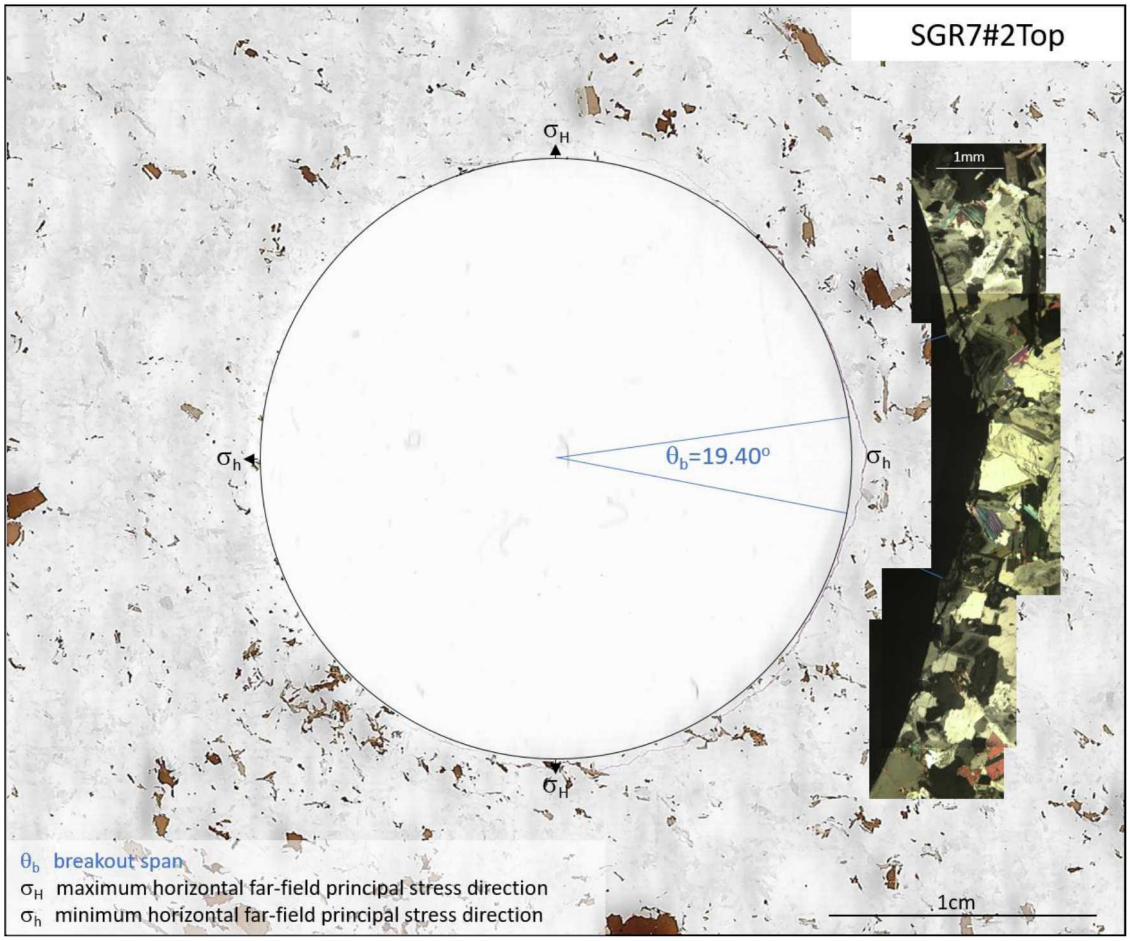
SGR7#2Top
σ_H
σ_h
σ_h
σ_H
θ_b=19.40°
1mm
1cm
θ_b breakout span
σ_H maximum horizontal far-field principal stress direction
σ_h minimum horizontal far-field principal stress direction


SGR30
σ_H
σ_h
σ_h
σ_H
1cm
σ_H maximum horizontal far-field principal stress direction
σ_h minimum horizontal far-field principal stress direction

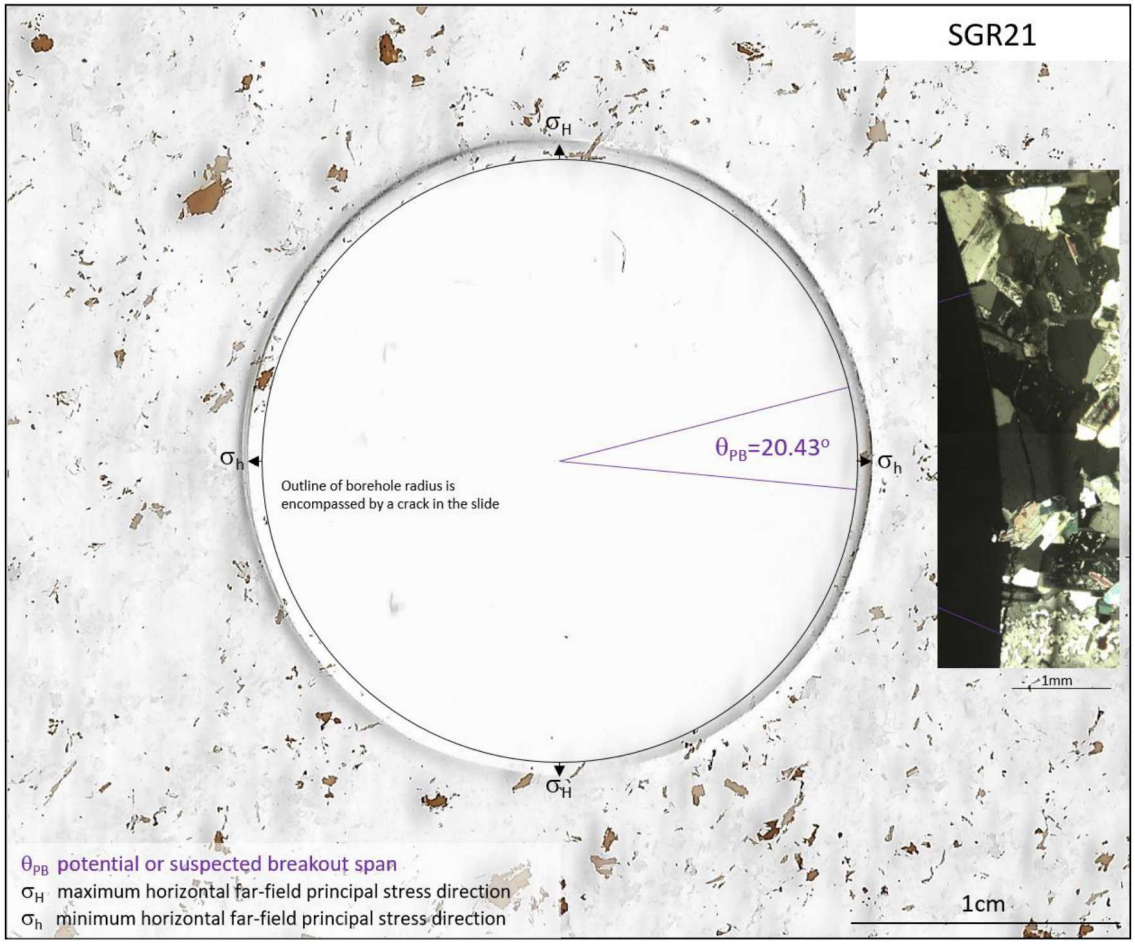
SGR21
σ_H
σ_h
θ_{PB}=20.43°
σ_h
Outline of borehole radius is encompassed by a crack in the slide
σ_H
1mm
θ_{PB} potential or suspected breakout span
σ_H maximum horizontal far-field principal stress direction
σ_h minimum horizontal far-field principal stress direction
1cm

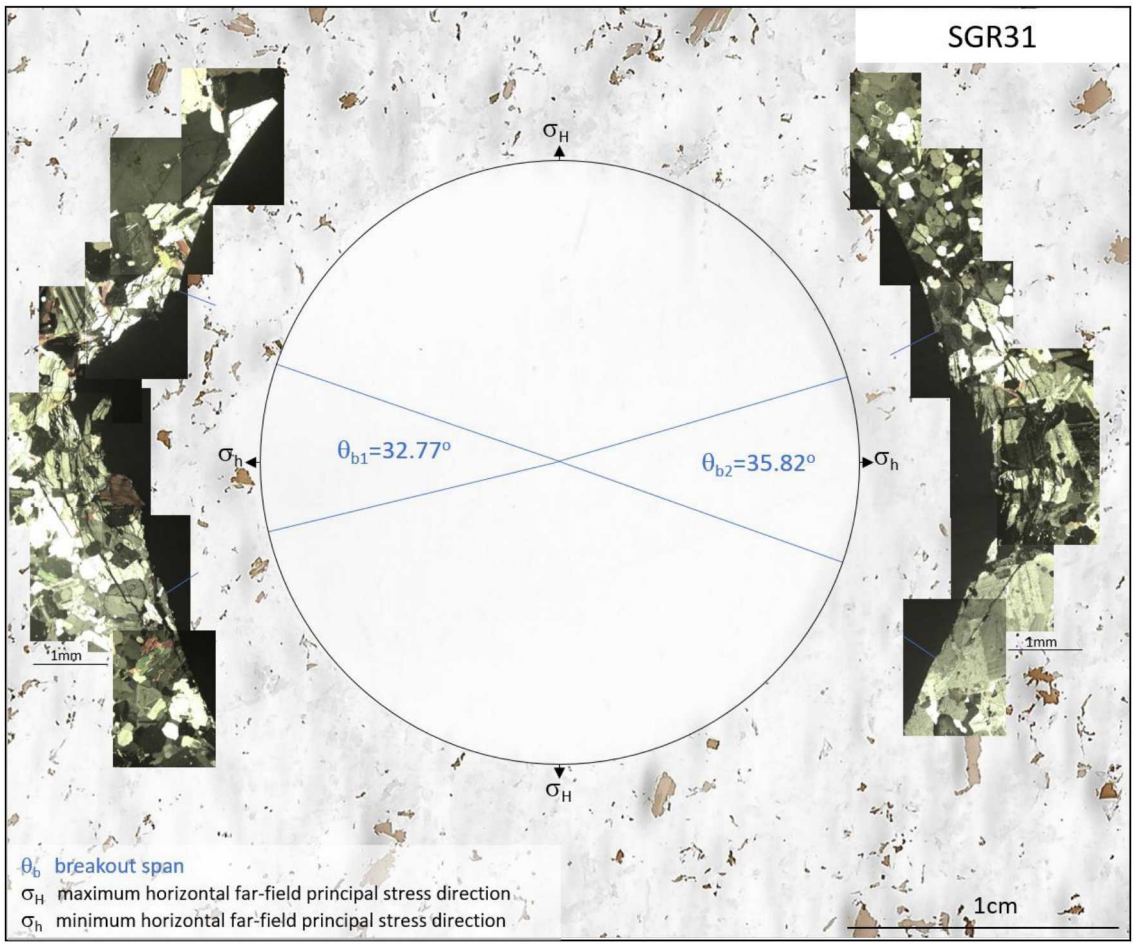
SGR31
σ_H
σ_h
θ_{b1}=32.77°
θ_{b2}=35.82°
σ_h
1mm
1mm
σ_H
θ_b breakout span
σ_H maximum horizontal far-field principal stress direction
σ_h minimum horizontal far-field principal stress direction
1cm

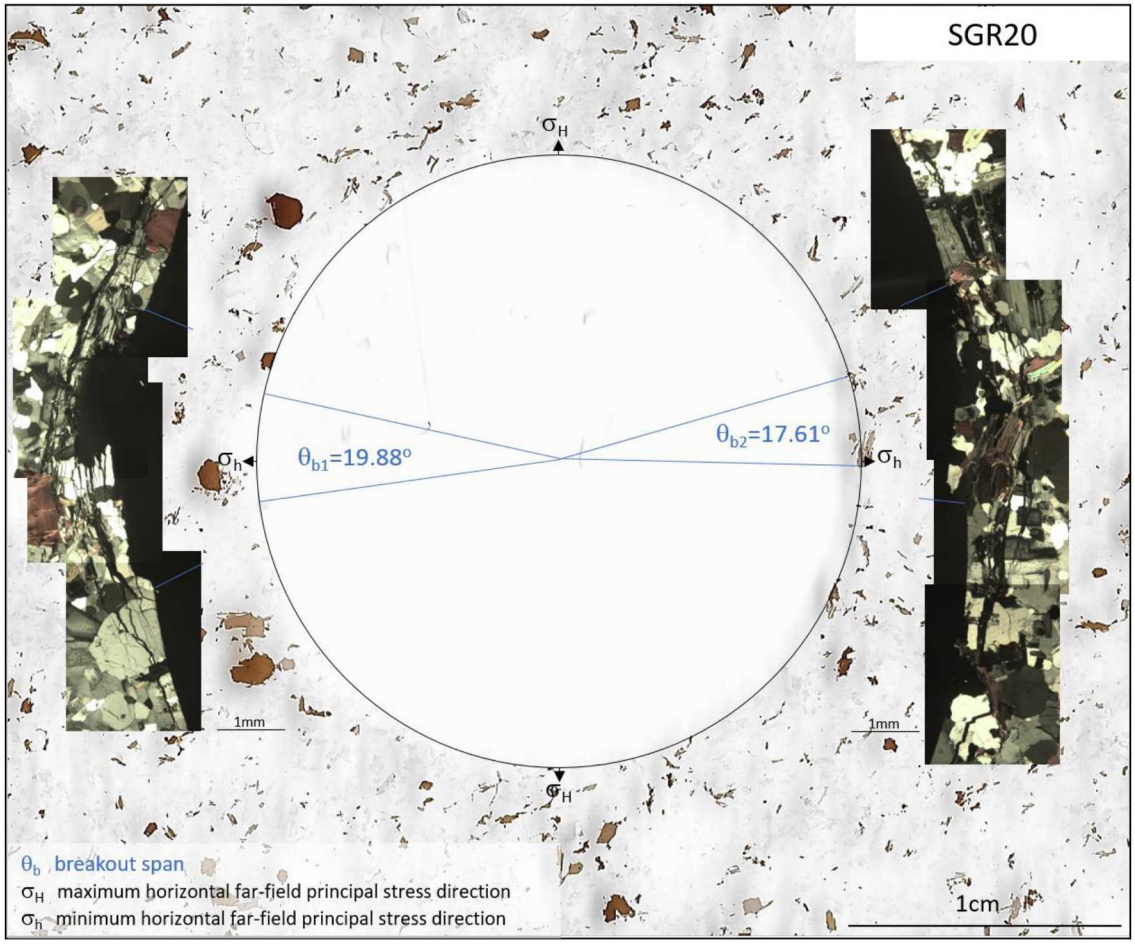
SGR20
σ_H
σ_h
θ_{b1}=19.88°
θ_{b2}=17.61°
1mm
1mm
σ_H
σ_h
1cm
θ_b breakout span
σ_H maximum horizontal far-field principal stress direction
σ_h minimum horizontal far-field principal stress direction

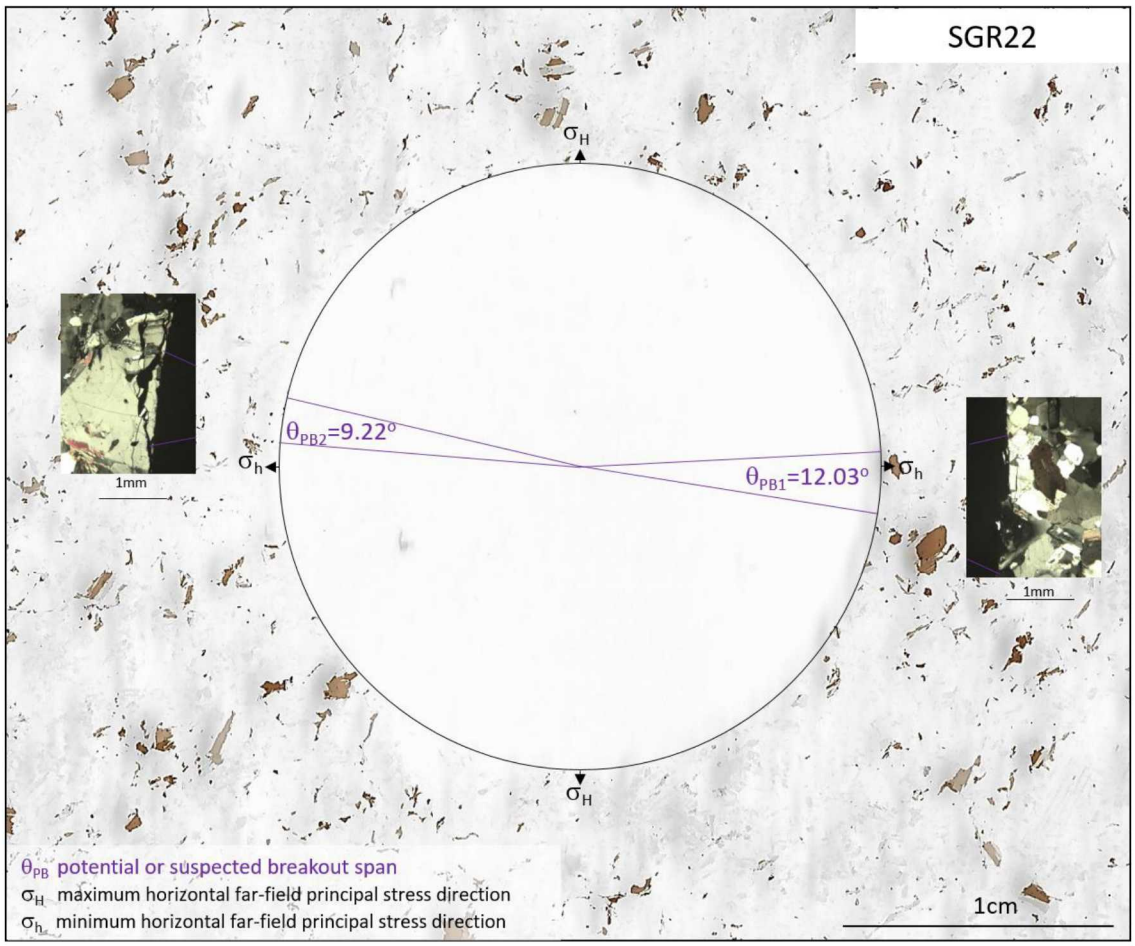
SGR22
σ_H
σ_h
θ_{PB2}=9.22°
θ_{PB1}=12.03°
1mm
1mm
σ_H
σ_h
1cm
θ_{PB} potential or suspected breakout span
σ_H maximum horizontal far-field principal stress direction
σ_h minimum horizontal far-field principal stress direction


SGR15#3
σ_H
σ_h
θ_{PB}=37.85°
σ_h
σ_H
1mm
1cm
θ_{PB} potential or suspected breakout span
σ_H maximum horizontal far-field principal stress direction
σ_h minimum horizontal far-field principal stress direction

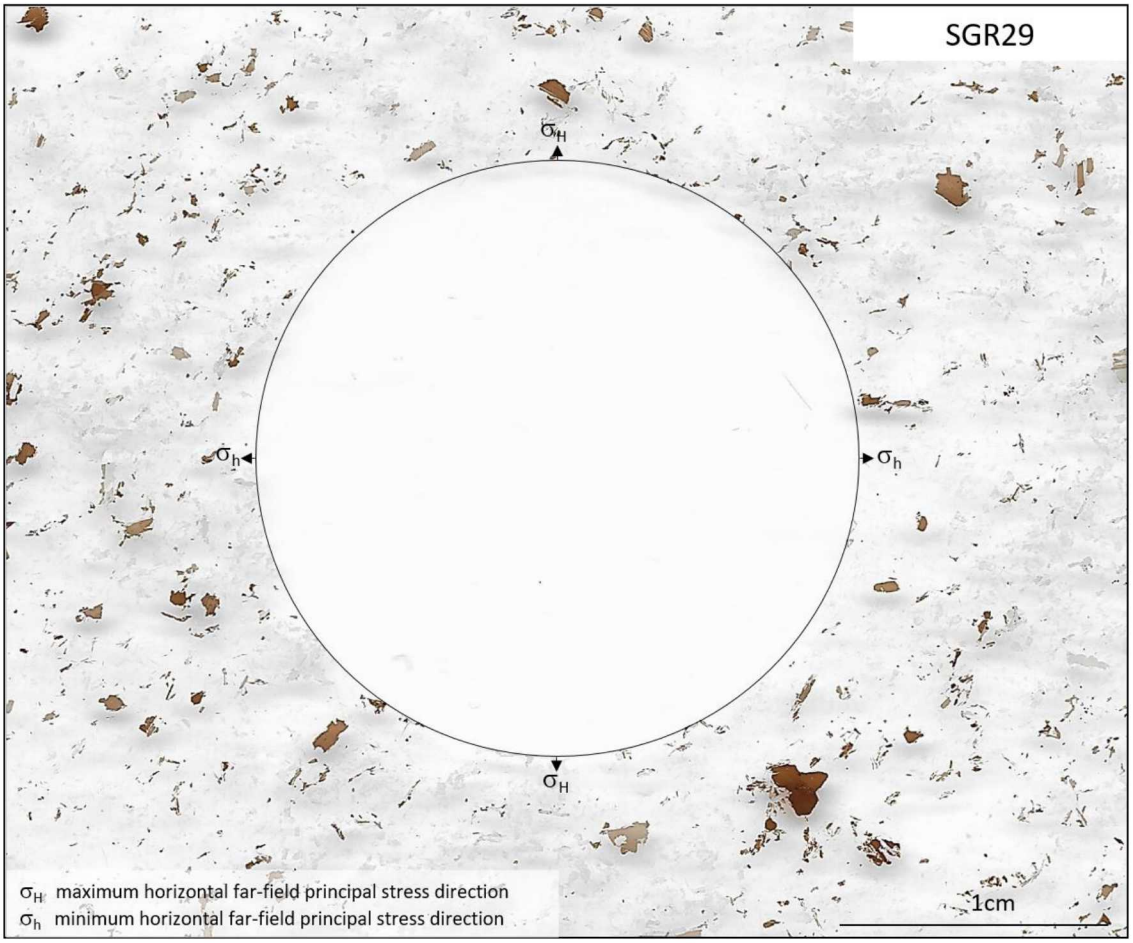
SGR29
σ_H
σ_h
σ_h
σ_H
1cm
σ_H maximum horizontal far-field principal stress direction
σ_h minimum horizontal far-field principal stress direction


SGR25
σ_H
σ_h
σ_h
σ_H
σ_H maximum horizontal far-field principal stress direction
σ_h minimum horizontal far-field principal stress direction
1cm


SGR27
σ_H
σ_h
σ_h
θ_{PB} = 18.60°
1mm
σ_H
θ_{PB} potential or suspected breakout span
σ_H maximum horizontal far-field principal stress direction
σ_h minimum horizontal far-field principal stress direction
1cm

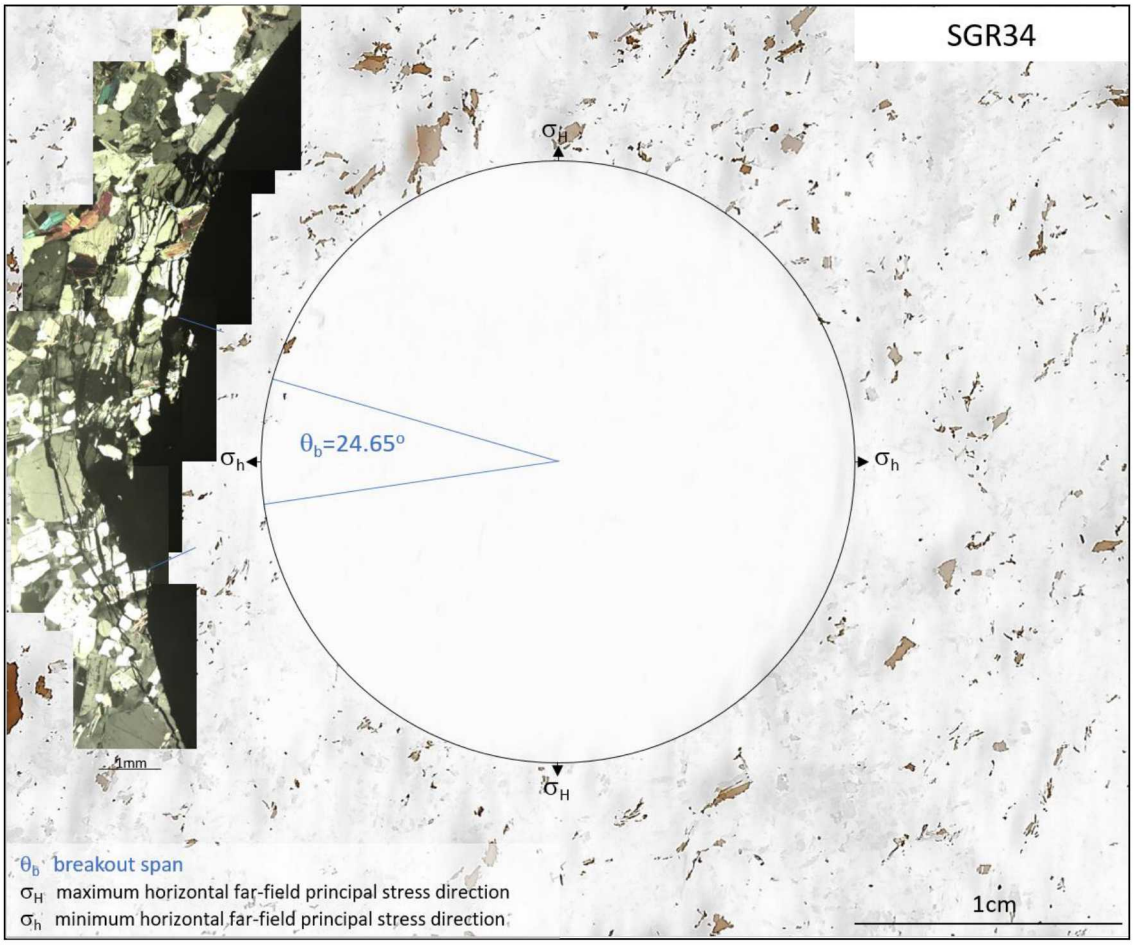
SGR34
σ_H
σ_h
θ_b=24.65°
σ_h
σ_H
1mm
1cm
θ_b breakout span
σ_H maximum horizontal far-field principal stress direction
σ_h minimum horizontal far-field principal stress direction

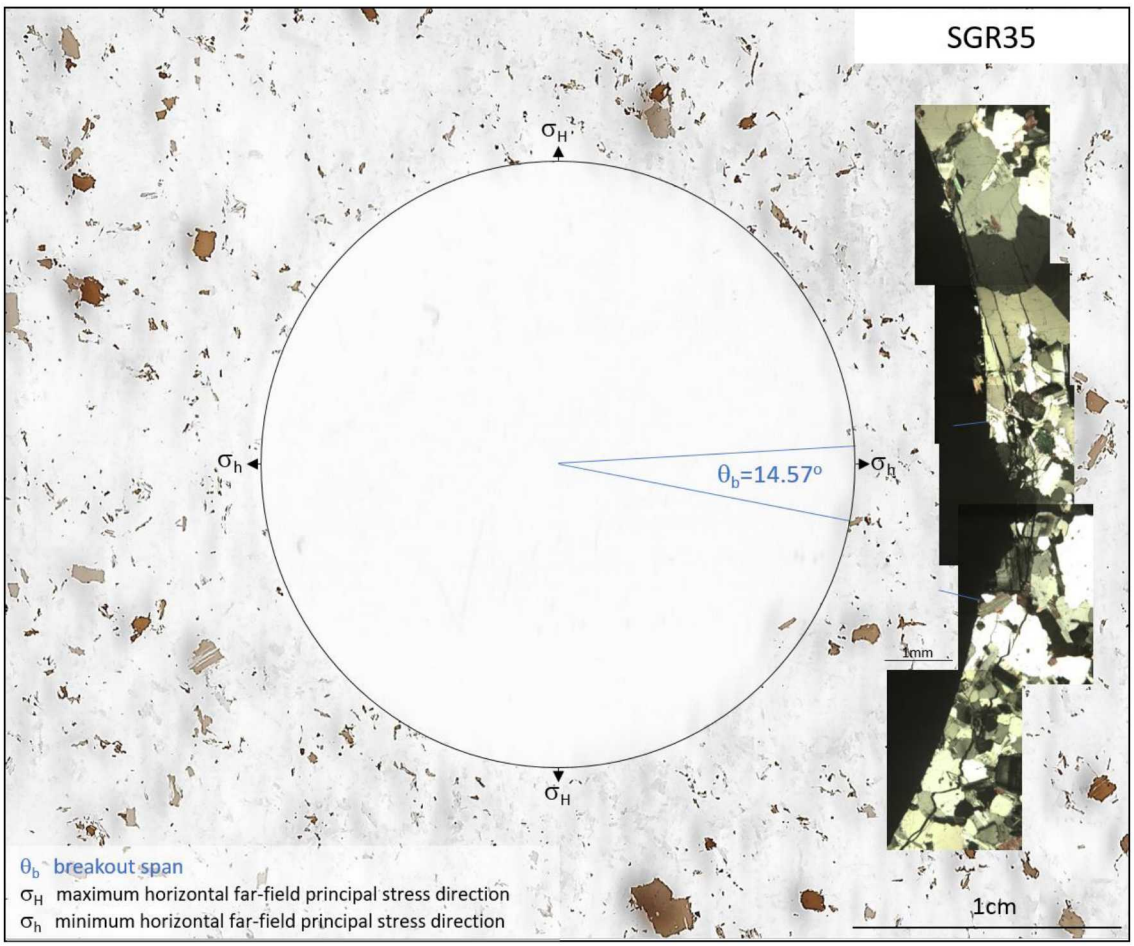
SGR35
σ_H
σ_h
θ_b=14.57°
σ_h
σ_H
1mm
1cm
θ_b breakout span
σ_H maximum horizontal far-field principal stress direction
σ_h minimum horizontal far-field principal stress direction

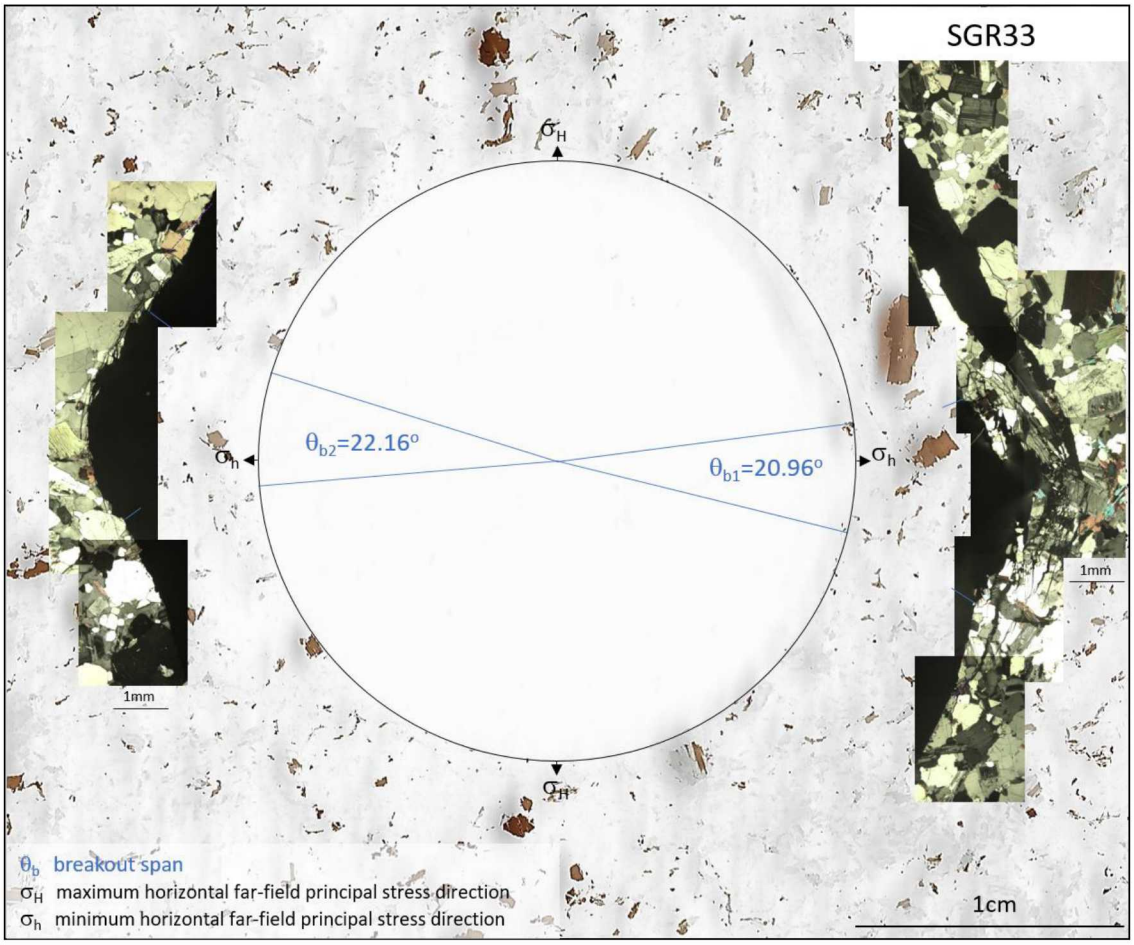
SGR33
σ_H
σ_h
θ_{b2}=22.16°
θ_{b1}=20.96°
σ_h
σ_H
1mm
1mm
1cm
θ_b breakout span
σ_H maximum horizontal far-field principal stress direction
σ_h minimum horizontal far-field principal stress direction

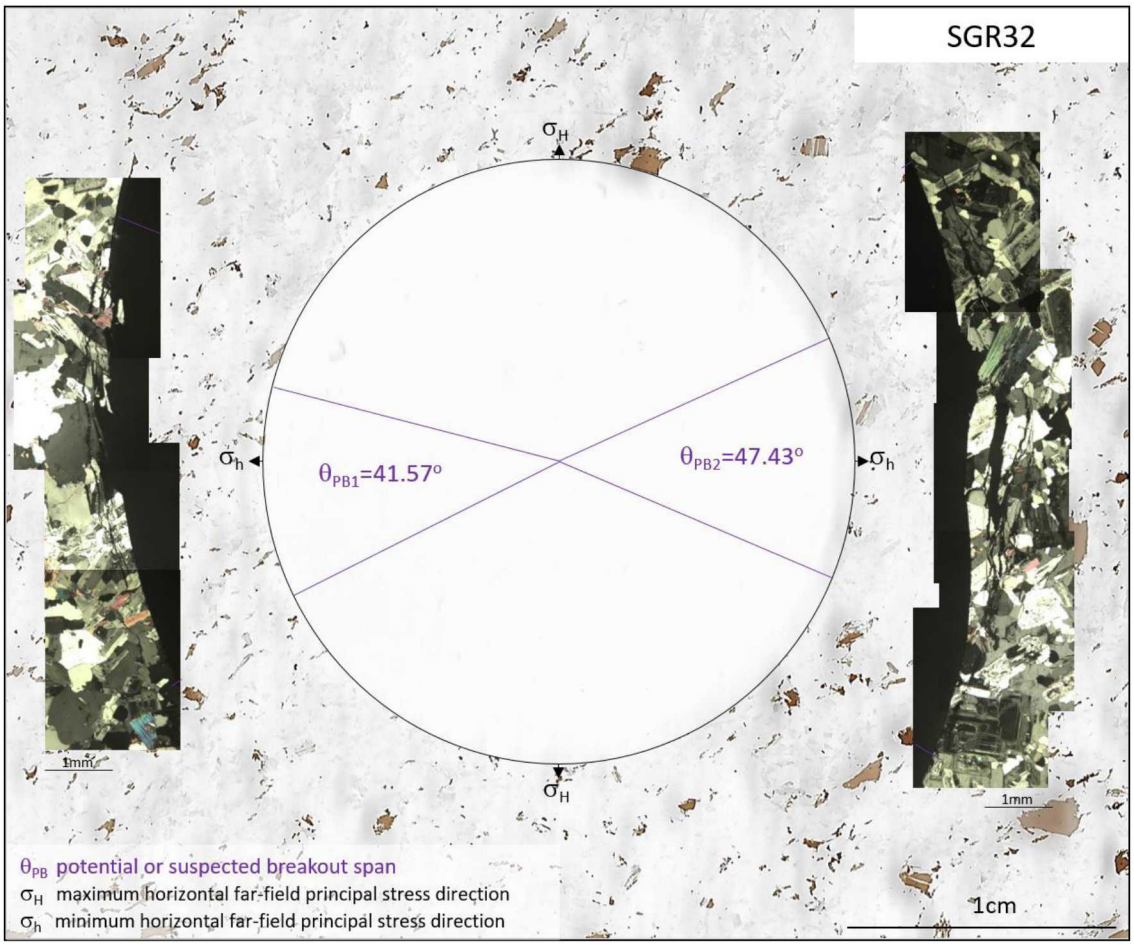
SGR32
σ_H
σ_h
θ_{PB1}=41.57°
θ_{PB2}=47.43°
σ_h
σ_H
1mm
1mm
1cm
θ_{PB} potential or suspected breakout span
σ_H maximum horizontal far-field principal stress direction
σ_h minimum horizontal far-field principal stress direction

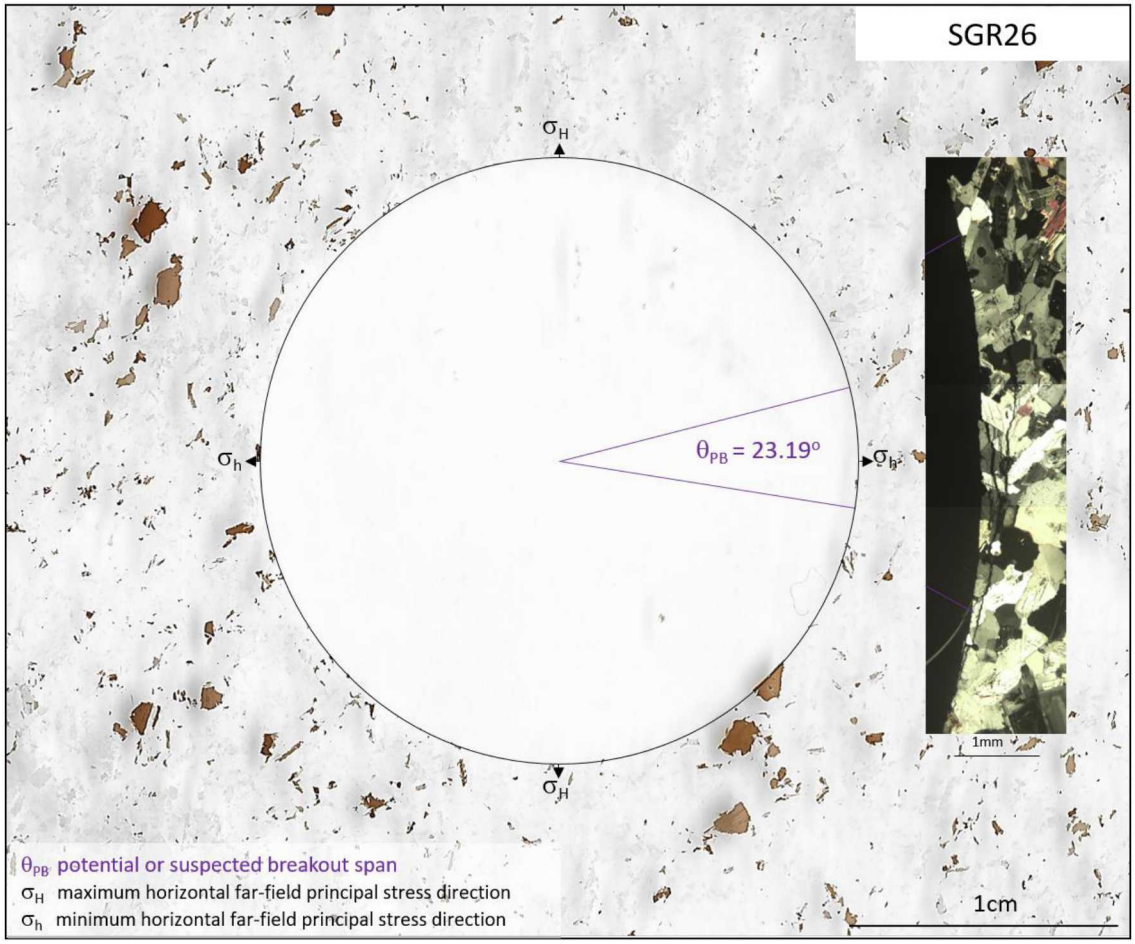
SGR26
σ_H
σ_h
θ_{PB} = 23.19°
1mm
1cm
θ_{PB} potential or suspected breakout span
σ_H maximum horizontal far-field principal stress direction
σ_h minimum horizontal far-field principal stress direction

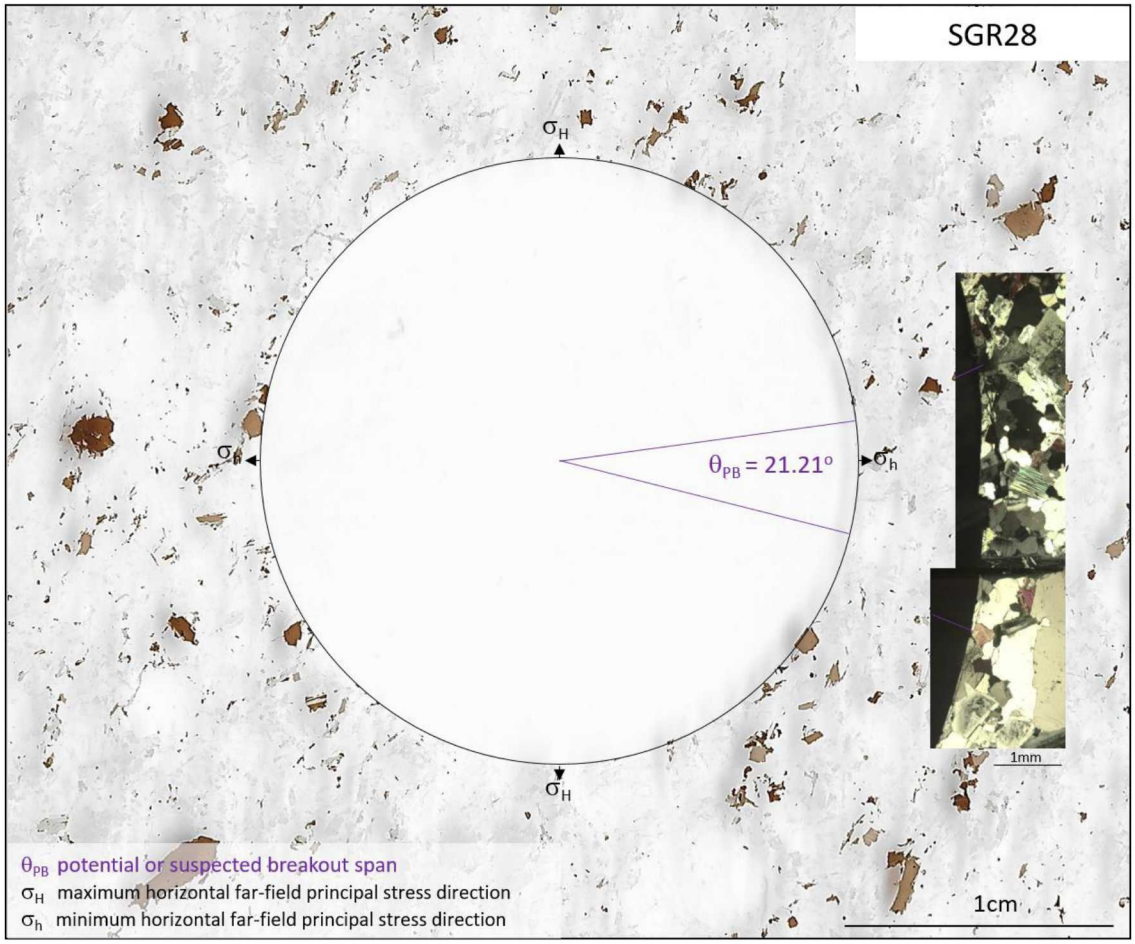
SGR28
σ_H
σ_h
θ_{PB} = 21.21°
1mm
1cm
θ_{PB} potential or suspected breakout span
σ_H maximum horizontal far-field principal stress direction
σ_h minimum horizontal far-field principal stress direction

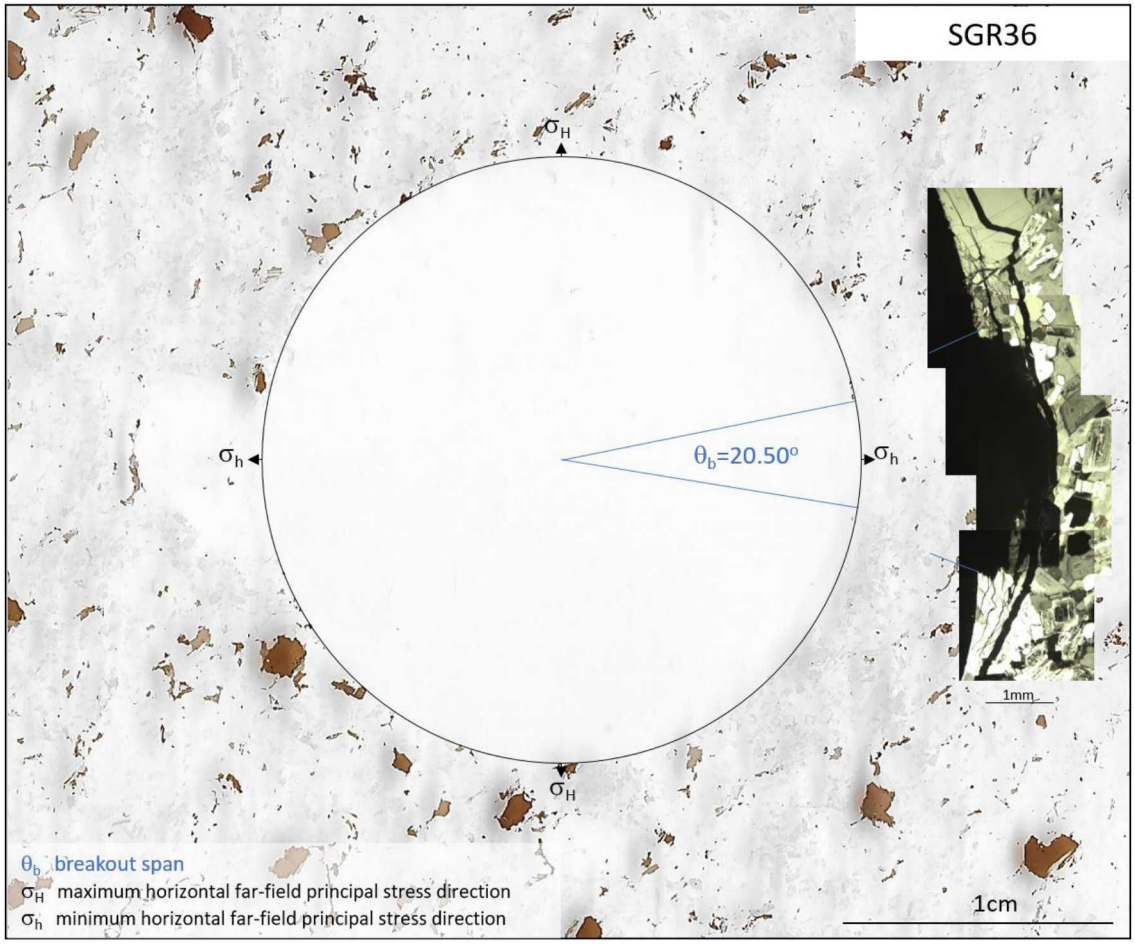
SGR36
σ_H
σ_h
θ_b=20.50°
σ_h
σ_H
1mm
1cm
θ_b breakout span
σ_H maximum horizontal far-field principal stress direction
σ_h minimum horizontal far-field principal stress direction

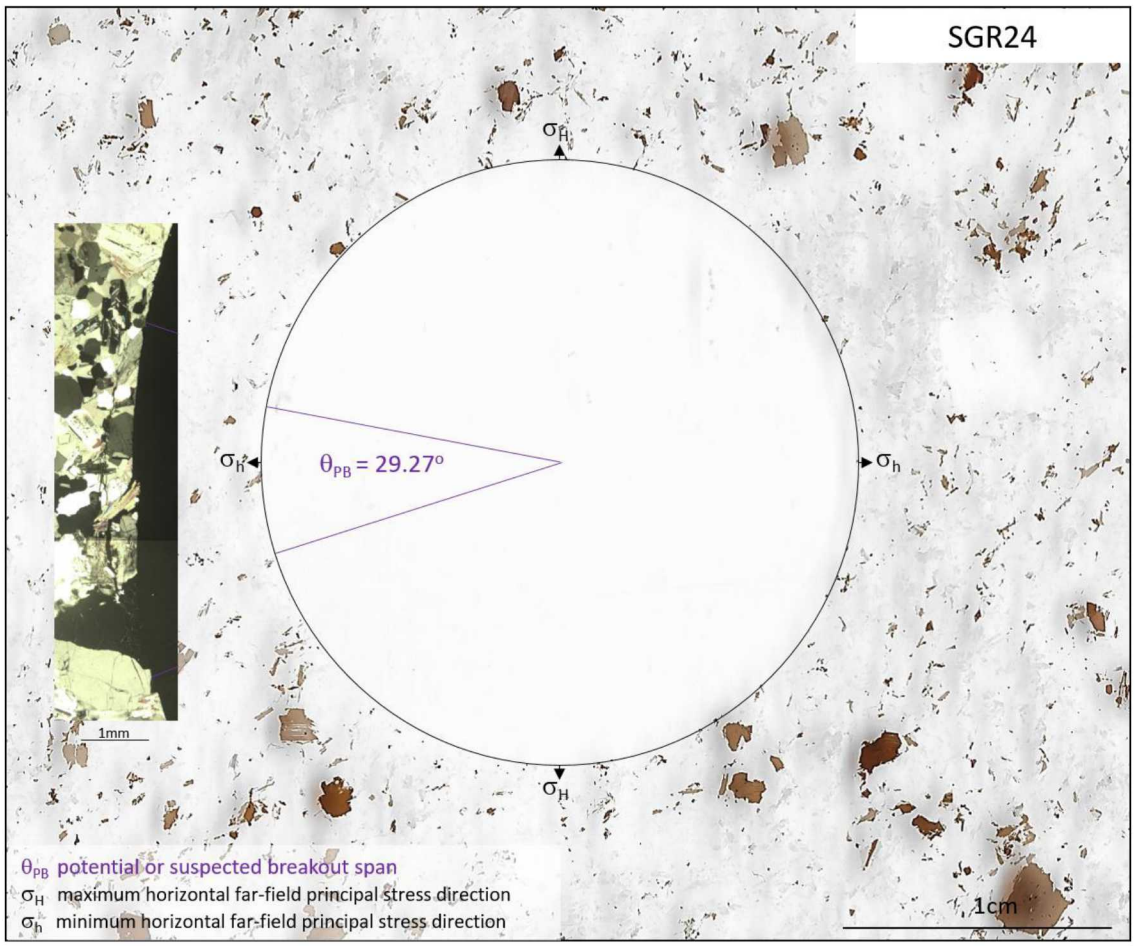
SGR24
σ_H
σ_H
θ_{PB} = 29.27°
σ_h
1mm
σ_H
1cm
θ_{PB} potential or suspected breakout span
σ_H maximum horizontal far-field principal stress direction
σ_h minimum horizontal far-field principal stress direction

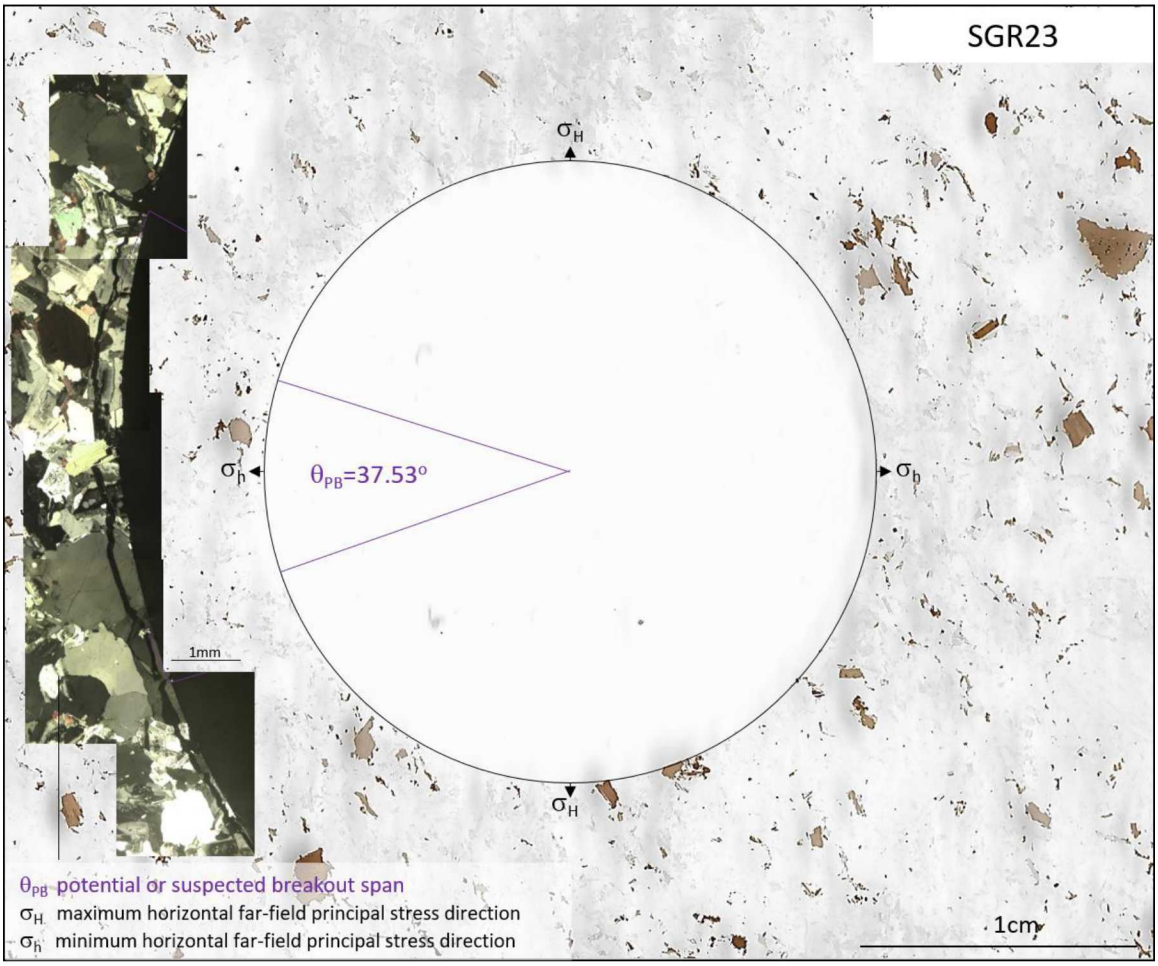
SGR23
σ_H
σ_h
θ_{PB}=37.53°
σ_h
σ_H
1mm
1cm
θ_{PB} potential or suspected breakout span
σ_H maximum horizontal far-field principal stress direction
σ_h minimum horizontal far-field principal stress direction

DISTRIBUTION

1	MS0359	D. Chavez, LDRD Office	1911 (electronic copy)
1	MS0735	R. Charles Choens	8864 (electronic copy)
1	MS0735	Erik Webb	8860 (electronic copy)
1	MS0735	Jennifer Wilson	8864 (electronic copy)
1	MS0735	Moo Lee	8864 (electronic copy)
1	MS0751	Thomas Dewers	8842 (electronic copy)
1	MS0751	Stephen Sobolik	8862 (electronic copy)
1	MS0899	Technical Library	9536 (electronic copy)
1	MS1033	Mathew Ingraham	8864 (electronic copy)
1	MS1033	Courtney Herrick	8864 (electronic copy)


Sandia National Laboratories